

AD

MODELLING AND CONTROL OF A MAGNETO- RHEOLOGICAL VIBRATION DAMPER

Final Technical Report

by

Dr R Stanway (Principal Investigator)
Dr A R Johnson (Co-Investigator)
Dr P H Mellor (Co-Investigator)
Mr A Godbehere (Technician)
Mr N D Sims (Research Student)
Mr J S Yang (Research Student)

United States Army

EUROPEAN RESEARCH OFFICE OF THE U.S. ARMY
London, England

CONTRACT NUMBER N68171-98-M-5388

R&D 8135-AN-015

Contractor : Department of Mechanical Engineering
University of Sheffield
Mappin Street
Sheffield S1 3JD
United Kingdom

Approved for Public Release; distribution unlimited.

DTIC QUALITY INSPECTED 4

20000816 038

REPORT DOCUMENTATION PAGE

Form Approved

OMB No. 0704-0188

Public reporting burden for this collection of information is estimated to average 1 hour per response, including the time for reviewing instructions, searching existing data sources, gathering and maintaining the data needed, and completing and reviewing the collection of information. Send comments regarding this burden estimate or any other aspect of this collection of information, including suggestions for reducing this burden, to Washington Headquarters Services, Directorate for Information Operations and Reports, 1215 Jefferson Highway, Suite 1204 Arlington, VA 22202-4302, and to the Office of Management and Budget, Paperwork Reduction Project (0704-0188), Washington, DC 20503.

1. AGENCY USE ONLY (Leave Blank)	2. REPORT DATE March 31st, 2000	3. REPORT TYPE AND DATES COVERED Final Report June 1999 - February 2000
----------------------------------	------------------------------------	--

4. TITLE AND SUBTITLE Modelling and Control of a Magneto-rheological Vibration Damper	5. FUNDING NUMBERS
--	--------------------

AUTHOR(S) R. Stanway, A. R. Johnson AND P. H. Mellor

6. PERFORMING ORGANIZATION NAME(S) AND ADDRESS(ES) Department of Mechanical Engineering The University of Sheffield Mappin Street SHEFFIELD S1 3JD UK	8. PERFORMING ORGANIZATION REPORT NUMBER MEC - ARO - F
---	---

9. SPONSORING/MONITORING AGENCY NAME(S) AND ADDRESS(ES) Dr Gary Anderson, U.S. Army Research Office Engineering and Environmental Sciences Division 4300 South Miami Boulevard NC 27709 2211 USA Research Triangle Park P O Box 12211	10. SPONSORING/MONITORING AGENCY REPORT NUMBER
--	--

SUPPLEMENTARY NOTES	12b. DISTRIBUTION CODE
DISTRIBUTION/AVAILABILITY STATEMENT	

ABSTRACT (Maximum 200 words) In this report, the authors describe a study to investigate the feasibility of developing a controllable vibration isolator based upon an MR squeeze-flow damper. The experiments demonstrate conclusively that it is feasible to control the transmissibility of a vibration isolator by manipulating the current supplied to an MR damper. The results also show that significant electromagnetic forces are generated by the damping device in the absence of MR fluid. There are two important implications of this latter result. First, in some applications, purely electromagnetic control of transmissibility may be possible. Second, electromagnetic forces do need to be included in an effective mathematical model. The available mathematical model was used in a numerical study to examine feedback control of the vibration isolator. The study shows that, using a simple switching strategy, significant performance gains might be available.

SUBJECT TERMS Magneto-rheological fluids, vibration isolation		15. NUMBER OF PAGES 109
16. PRICE CODE		17. SECURITY CLASSIFICATION OF ABSTRACT
18. SECURITY CLASSIFICATION OF THIS PAGE	19. SECURITY CLASSIFICATION OF ABSTRACT	20. LIMITATION OF ABSTRACT

01-280-5500

Standard Form 298 (Rev. 2-89)
Prescribed by ANSI Std. Z39-18
298-102

ATTACHMENT 1 PAGE 1 ○

ABSTRACT

In this report, the authors describe a study to investigate the feasibility of developing a controllable vibration isolator based upon an MR squeeze-flow damper. The study involves the design and construction of a special isolator test facility into which was incorporated an MR damper loaned to the authors by Dr Mark Jolly of Lord Corporation. Also an existing model of the damper is extended to take account of the isolator dynamics and to predict its transmissibility versus frequency characteristics.

The experimental results demonstrate conclusively that it is feasible to control the transmissibility of a vibration isolator by manipulating the current supplied to the MR squeeze-flow damper. The results also show that significant electromagnetic forces are generated by the damping device in the absence of MR fluid. There are two important implications of this result. First, in some applications purely electromagnetic control of transmissibility may be possible. Second, electromagnetic forces do need to be included in an effective mathematical model. A suitable model needs to account for static shifts in the inter-pole gap when a current is applied together with electromagnetic stiffness and damping effects which are evident under dynamic conditions.

In order to predict the general form of the transmissibility characteristics, the mathematical model had to be modified to account for the increases in resonant frequency which were observed experimentally. The resulting model predicted well the general form of the transmissibility versus frequency characteristics but over-estimated the amplitudes of the resonant peaks. This is understandable since the electromagnetic damping forces were not included. There was sufficient confidence in the model to use it as the basis of a numerical study into feedback control of the vibration isolator. The simulation results clearly show the performance gains which might be available using a well-known switching algorithm. However, the results also show how the closed-loop performance is degraded by the base viscosity of the MR fluid.

LIST OF KEYWORDS

Smart fluids; electro-rheological (ER) fluids; magneto-rheological (MR) fluids;
squeeze-flow operation; vibration control; vibration isolation;
electromagnetic damping; closed-loop control; skyhook damping

TABLE OF CONTENTS

BODY OF REPORT

Statement of Problem	page 1
Background	page 1
Approach	page 2
Experimental Apparatus	page 2
MR Squeeze-Flow Damper	page 3
Experimental Procedure and Results	page 3
Experiments Performed	page 3
Modelling and Control	page 5
Discussion	page 7
Conclusions	page 8
Recommendations for Further Work	page 9

LITERATURE CITED	page 11
------------------	---------

ACKNOWLEDGEMENTS	page 12
------------------	---------

FIGURES

APPENDIX A

APPENDIX B

APPENDIX C

APPENDIX D

BODY OF REPORT

Statement of Problem

The problem addressed in the present investigation is that of investigating the feasibility of developing a controllable vibration isolator based upon a magneto-rheological (MR) damping device. In the project proposal it was suggested that the approach taken would involve the following steps:

- the design and construction of an MR damper;
- the design and construction of a vibration isolator test facility to accommodate the MR damper;
- a detailed study of the performance of the MR damper and isolator and comparison with model predictions;
- recommendations for further work and identification of early opportunities for technology transfer.

Despite a shift in emphasis away from the design and construction of the MR damper itself (see "Background"), these steps have been followed and the results are described in the sections which follow.

Background

In the project proposal it was argued that there is a need to develop controllable mounts for vibration isolation. In principle, controllable (or semi-active mounts) improve upon the performance of purely passive mounts without involving the cost, weight and complexity associated with fully active devices. One of the present investigators (RS) had progressed as far as demonstrating the feasibility of constructing a controllable mount and showing experimentally how its performance was superior to a passive scheme (Stanway et al., 1992). The controllable mount employed an electro-rheological (ER) fluid whose resistance to flow can be varied continuously through the application of an electric field of sufficient intensity. Through electric-field control it was shown that the transmissibility of the vibration isolator mount could be manipulated so as to suppress resonance and also obtain superior high-frequency isolation.

The ER damper used in the experiments by Stanway and his colleagues was unusual in that it operated in the so-called squeeze-flow mode of operation, where the fluid is placed in tension/compression between oscillating electrodes. This type of operation results in an extremely simple and compact mechanical arrangement which can accommodate displacements of several millimeters. Despite the fact that it had been demonstrated that a controllable automotive engine mount could be constructed in this way, commercial exploitation did not follow. The most likely explanation for the lack of industrial interest was the need to provide high voltages (up to 10 kV) in order to create an electrical field of sufficient intensity.

The re-discovery of MR fluids in the 1990s (Sims et al., 1999) opened up new opportunities for squeeze-flow devices. MR fluids require an electromagnetic field to change their resistance to flow and hence the inherent simplicity of an ER squeeze-flow device is lost. However, the coil of the electromagnet can be driven by a low-voltage source (say, from zero to 15 v) and obviously this does not pose the perceived safety problems associated with ER fluids and high-voltage supplies. Jolly and Carlson (1996) soon reported on a prototype MR squeeze-flow device and shortly after such devices went into mass production (Jolly et al., 1998).

When proposing the present project the authors argued that there are a number of issues associated with MR-based vibration isolation which need to be addressed. Both the modelling and control of MR squeeze-flow dampers are at an early stage of development and there are specific aspects such as speed of response which require investigation. To begin addressing these issues a programme of work was suggested. The programme was based around the design and construction of an MR squeeze-flow damper and an associated vibration isolator. During the assessment of the proposal, the authors were offered the loan of the prototype device examined by Jolly and Carlson. This offer was accepted and thus emphasis was shifted away from MR device design and towards construction and testing of an MR-based vibration isolator. In the section which follows, design and construction of the isolator is described before dealing with test procedures, results and their interpretation.

Approach

Experimental Apparatus

Since the behaviour of the ER-based vibration isolator (Stanway et al., 1992) is now relatively well understood and also mimics the operation of a realistic industrial application (an automotive engine mount), it was decided to reproduce the essential features of the earlier apparatus. Consequently the mass to be isolated was chosen to be 60 kg supported on a specially constructed coil spring of stiffness 50 kN/m. These choices provided an isolator with an undamped natural frequency of approximately 5 Hz. The MR damper is placed in parallel with the coil spring. Excitation is provided at the base of the coil spring and MR damper by a servo-hydraulic test machine ("Instron" model 8501). The arrangement described above is shown in Figure 1. Note that a photograph of the completed test facility and a full set of detail drawings was included in Interim Report No. 1.

Referring to Figure 1, the test machine is capable of providing controlled displacement inputs over the frequency range from zero to 200 Hz. The parallel combination of the MR damper and coil spring serves to isolate the mass carriage from this base motion. A mechanism incorporating a micrometer barrel is included to allow accurate setting of the initial inter-pole gap of the MR damper. The mass carriage is constrained to translate in the vertical direction by a pair of linear bearings which are located by a guide shaft. The guide shaft is attached to the fixed cross-beam of the "Instron" test machine. Base motion is monitored by

instrumentation within the test machine. Motion of the mass carriage is monitored by an LVDT (not shown on Figure 1).

MR Squeeze-Flow Damper

The MR damper, on loan from Dr Mark Jolly of Lord Corporation, and included in Figure 1, is shown in greater detail in Figure 2. It comprises a single acting squeeze-flow device with one fixed pole and one moving pole. The electromagnetic coil is toroidal in form and embedded in the iron of the fixed pole. The moving pole is made from steel and is constrained by a rubber bush which allows vertical movement. The shaft attached to the upper pole is threaded, and along with a locknut, allows the inter-pole gap to be adjusted and fixed.

MR fluid (Lord Corporation type MRF-240 BS) is contained in the inter-pole gap. The MR fluid is excited by a magnetic field created by passing current through the electromagnetic coil. The current is provided by a low voltage power supply ("Farnell" type E30/2) which requires no additional amplification.

Experimental Procedure and Results

Experiments Performed

To characterise the behaviour of the MR-based vibration isolator the experiments have been divided into three categories:

- 1) preliminary experiments in the absence of MR fluid and with MR fluid;
- 2) further tests in the absence of MR fluid;
- 3) further tests involving MR fluid.

1) Preliminary Experiments

Preliminary experiments were performed for inclusion in Interim Report No. 2. The mathematical model described by Jolly and Carlson (1996) included only forces developed within the MR fluid and ignored electromagnetic effects. However, the results of a finite-element study (Wong, 1999, included as an Appendix in Interim Report No. 2) indicated that electromagnetic forces were likely to be significant and this was confirmed by tests during the preliminary experimental phase.

The first point to note is that, in the absence of MR fluid, the application of a current to the coil of the electromagnetic causes a significant shift in the inter-pole gap of the damper and thus in the mean level of oscillation of the vibration isolator. The results in Figure 3 were obtained with an initial gap of 2 mm and by increasing the potential applied to the coil from zero to 12 v. Referring to Figure 3, increasing the voltage in this way thus causes the inter-pole gap to reduce by approximately 0.7 mm and thus close to 1.3 mm when the full 12 v. is applied. This effect is almost independent of the mechanical excitation frequency.

In view of this result it was decided to undertake transmissibility tests in the absence of MR fluids. A typical result is shown in Figure 4 where increasing the applied potential from zero to 12 v. reduces the peak transmissibility from around 9.5 to 4.0.

With MR fluid introduced into the inter-pole gap the transmissibility of the vibration isolator can be controlled over an even wider range. The results in Figure 5 show that increasing the applied potential from zero to 6 v. causes the peak transmissibility to reduce from 3.0 to around 0.5. In other words the resonance (at around 7 Hz with MR fluid added) can be completely suppressed through the current supplied to the MR damper. It should be borne in mind that the results in Figures 5 and 6 were not obtained about a common equilibrium position - this shifted continuously as the applied voltage was changed. However, the feasibility of exercising significant control over transmissibility, both with and without MR fluid, was established.

2) Further tests in the absence of MR fluid

To examine the performance of the isolator under open-loop conditions using purely electromagnetic damping, a further set of tests was carried out in the absence of MR fluid. Beginning with an initial inter-pole gap of 1.0 mm and no electrical excitation applied to the coil of the MR damper, the mechanical excitation frequency was increased in steps from 0.1 to 15 Hz. The displacement of the mass carriage was noted at each step. The potential difference applied to the MR damper coil was then increased in steps up to 15 v. and the transmissibility test was repeated at each step. The whole procedure described above was then repeated for initial inter-pole gaps of 1.5, 2.0, 2.5 and 3.0 mm. The input displacement to the isolator was held constant at 0.2 mm peak-to-peak throughout the tests. The results are displayed in Figures 6, 7, 8, 9 and 10.

The control of the resonant amplitude for the various initial gaps is summarised in Table I.

Initial inter-pole gap (mm)	Measured decrease in resonant amplitude ratio
1.0	from 8 to 1
1.5	from 14 to 1
2.0	from 19 to 5
2.5	from 23 to 7
3.0	from 24 to 13

Table I. Control of resonant amplitude using electromagnetic damping.

From Table I it can be seen that at inter-pole gaps of 1.0 and 1.5 the maximum transmissibilities are 8 and 14, respectively, and lock-up can be achieved given sufficient applied potential. With the larger initial gaps the electromagnetic damping force is reduced, maximum resonant amplitudes are higher and it is not possible to lock up the isolator over the whole frequency range.

3) Further tests involving MR fluid

Problems arose when re-filling the device with MR fluid as it was not at all obvious how much fluid should be introduced. The device was filled by removing the rubber bush which supports the upper (moving) pole and pouring MR fluid onto the lower (fixed) pole. The preliminary results with MR fluid (Figure 6) were obtained by leaving some free space between the upper pole and the rubber bush. However, it proved difficult to reproduce this procedure.

The initial intention was to reproduce the tests performed in the absence of MR fluid. Unfortunately the results obtained with initial inter-pole gaps of 1.0 and 1.5 mm were so erratic as to be meaningless. Consistent sets of results were obtained for initial gaps of 2.0, 2.5 and 3.0 mm and these are shown in Figures 11, 12 and 13. Table II summarises control of the resonant amplitudes which was obtained in these experiments.

Initial inter-pole gap (mm)	Measured decrease in resonant amplitude ratio
2.0	from 3 to 1
2.5	from 8 to 1
3.0	from 9 to 1

Table II. Control of resonant amplitude using MR damping.

Table 2 shows that the introduction of MR fluid reduces the transmissibilities at resonance and allows the isolator to be locked over the whole frequency range. However, note from Figures 11, 12 and 13 that the resonance has now shifted up to 8 Hz. In the preliminary tests involving MR fluids and tests in the absence of MR fluid, resonance had occurred at 7 Hz. The most likely causes of this shift is from using additional MR fluid which provides an effective additional stiffness and hence the increased resonant frequency.

Modelling and Control

The tentative model of the MR damper used in the present study is the one described by Jolly and Carlson (1996). This is a quasi-steady model which includes the effect of the developed MR yield stress together with viscous and fluid inertia terms. This model was extended to account for the dynamics of the mass carriage and coil spring in the MR-based vibration isolator. The resulting model takes the form

$$m\ddot{y} + k(y - u) + F_{MR} = 0$$

where y is the displacement of the mass carriage, u is the displacement input at the base of the isolator and F_{MR} is the total force developed by the MR damper. The supported mass is denoted by m and the spring constant by k . Details of the

model are given in the paper by Stanway et al. (2000) which is included as Appendix A in the present report.

This model was used in an attempt to predict the experimental results obtained using MR fluid and shown in Figures 11, 12 and 13. The corresponding numerical results are shown in Figures 14, 15 and 16. Note that the model stiffness has been increased to account for the additional effective stiffness introduced by the MR fluid. Table III summarises control of the resonant amplitudes which was obtained in these numerical experiments.

Initial inter-pole gap (mm)	Predicted decrease in resonant amplitude ratio
2.0	from 7 to 1
2.5	from 9 to 1
3.0	from 12 to 1

Table III. Control of resonant amplitude using MR damping : simulation results.

Comparing this table with the experimental results in Table II, it is apparent that the maximum amplitudes are higher than those measured. This is not unexpected since the experimental results were influenced by the presence of additional electromagnetic damping and the damping introduced by the rubber bush which were not included in the model.

The experimental and simulation results are not directly comparable for another reason: lack of available information on the physical construction of the MR damper meant that it was difficult to relate yield stress, developed within the MR fluid, to the current supplied to the damper's coil. Some relationships were obtained by a combination of numerical and empirical means. (Wong (1999) included as an Appendix to Interim Report No. 2).

Despite the shortcomings of the available mathematical model, comparison of the predictions in Figures 14-16 with the corresponding experimental results in Figures 11-13 reveals that the model captures the essential features of the behaviour of the MR-based vibration isolator. Consequently it was decided to use the model to examine the effect of a feedback control strategy on the transmissibility of the isolator. As a first attempt, the well-known algorithm due to Karnopp et al., (1974) was chosen. Using a switching strategy based upon the directions of the mass velocity and the relative velocity between the mass and base, the algorithm provides an approximation to the optimum single degree-of-freedom isolator which was derived by Bender (1968).

Mathematically, the strategy reduces to the following logic statements.

If $\dot{y}(\dot{y} - \dot{u}) > 0$, then switch on the MR damper.

If $\dot{y}(\dot{y} - \dot{u}) < 0$, then switch off the MR damper,

where \dot{y} and \dot{u} are the velocities of the mass and base, respectively.

To implement this algorithm experimentally will obviously require additional instrumentation, essentially to provide measurements of the velocities \dot{y} and \dot{u} , to perform the logic, and to switch the MR damper's electrical supply. Numerical results obtained at the time of writing indicate that the performance gains available may well justify the cost of the additional components. Figure 17 shows the influence on transmissibility if the MR damper is switched between zero yield stress and finite values ranging up to 500 Pa. By switching in this way it appears possible to suppress the resonance and reduce the transmission of higher frequency vibrations. In practice, if the current to the MR damper's coil was switched off, damping forces would still be present, owing essentially to the viscosity of the base fluid. The effect of this inherent viscosity is shown in Figure 18. Control of resonance is relatively unaffected at the lower values of yield stress but the lower limit is higher than that shown in Figure 18. Perhaps more significantly the transmissibility characteristics exhibit a crossover after resonance, after the fashion of a linear, single degree-of-freedom vibration isolator. Consequently the most effective control of resonance is achieved at the expense of less effective control of high frequency transmission. Nevertheless, the simulation results in Figure 19 show an enormous improvement in transmissibility reduction over open-loop control and represent an obvious target for further investigation.

Discussion

The design and construction of a controllable vibration isolator has been described. Damping is provided by an MR fluid device operating in the squeeze-flow mode. By varying the current supplied to the electromagnetic coil of the MR damper the available damping forces can be controlled, and thus the transmissibility of the isolator. Tests were performed to determine the degree of control which could be exercised over transmissibility. The results obtained are not wholly conclusive but nevertheless point clearly to directions for further work.

Initial tests were aimed at quantifying the electromagnetic forces which are available in the absence of MR fluid in the damper. In a single acting device, such as the one investigated here, the application of current causes a shift in the inter-pole gap of the damper and thus of the equilibrium position around which the vibration isolator operates. A way of dealing with this problem is discussed later.

From the main body of tests conducted in the absence of MR fluid, it was noted that:

- controllable vibration isolation is available on the basis of electromagnetic damping alone;
- with the damper in place, the resonant frequency of the vibration isolator is increased from 5 Hz to 6Hz. This increase is essentially due to the presence of the rubber bush which supports the moving pole of the MR damper;

- electromagnetic forces clearly need to be accounted for in the mathematical model.

After introducing MR fluid into the damper, it was noted that:

- controllable vibration isolation is available over the range of inter-pole gaps from 2.0 to 3.0 mm (and probably above). Smaller inter-pole gaps produced erratic results;
- with the MR damper under investigation the results were not repeatable. It is suggested that this is largely due to the difficulty in deciding how much fluid to introduce;
- the amount of fluid introduced into the inter-pole gap has a significant effect on the overall stiffness of the isolator: resonant frequencies measured ranged from 6 to 8 Hz.

In the modelling study, based upon an existing quasi-steady model of the MR damper, it was found that:

- the model was capable of predicting the general trend of the transmissibility versus frequency characteristics but consistently underestimated the amount of damping available;
- the model needs refining both to account for electromagnetic damping generated on the MR device and to account for increased stiffness effects, which arise from the MR fluid;
- work is required to relate the current supplied to the MR damper's coil to the yield stress developed within the MR fluid. In order to achieve this objective, it is essential to employ an MR damper in which all the physical properties are known.

Based upon the existing model, a numerical study was used to investigate the influence of on-off feedback control for improving the transmissibility of the isolator. Using a well-established switching strategy it was shown that, in principle, both resonance and high frequency transmission can be reduced much more effectively than is possible using an open-loop strategy.

Conclusions

In this report, the authors have described a study to investigate the feasibility of developing a controllable vibration isolator based upon an MR squeeze-flow damper. The study has involved the design and construction of a special isolator test facility into which was incorporated an MR damper loaned to the authors by Dr Mark Jolly of Lord Corporation. Also an existing model of the damper was extended to take account of the isolator dynamics and to predict its transmissibility versus frequency characteristics.

The experimental results demonstrate conclusively that it is feasible to control the transmissibility of a vibration isolator by manipulating the current supplied to an MR squeeze-flow damper. The results also show that significant electromagnetic forces are generated by the damping device in the absence of MR fluid. There are

two important implications of this result. First, in some applications purely electromagnetic control of transmissibility may be possible. Second, electromagnetic forces do need to be included in an effective mathematical model. A suitable model needs to account for static shifts in the inter-pole gap when a current is applied together with electromagnetic stiffness and damping effects which are evident under dynamic conditions.

With MR fluid in place in the damper reasonably consistent results were obtained using initial inter-pole gaps in the range from 2.0 to 3.0 mm. The use of smaller initial gaps produced erratic results. A major problem emerged by emptying and re-filling the damper as it was difficult to assess how much MR fluid to introduce. As a result the experimental traces were not repeatable.

In order to predict the general form of the transmissibility characteristics, the mathematical model had to be modified to account for the increases in resonant frequency which were observed experimentally. The resulting model predicted well the general form of the transmissibility versus frequency characteristics but over-estimated the amplitudes of the resonant peaks. This is understandable since the electromagnetic damping forces were not included. There was sufficient confidence in the model to use it as the basis of a numerical study into feedback control of the vibration isolator. The simulation results clearly show the performance gains which might be available using a well-known switching algorithm. However, the results also show how the closed-loop performance is degraded by the base viscosity of the MR fluid.

Recommendations For Further Work

It has been emphasised throughout this report that the results, although not wholly conclusive, are valuable nevertheless in that they point clearly to directions for further work.

In the authors' opinion, the most pressing need is for a comprehensive mathematical model to account for static and dynamic effects in MR squeeze-flow dampers. Because of the complex interaction of electrical and mechanical variables within such devices, the development of modelling techniques will probably involve a combination of theoretical and experimental techniques. An MR squeeze-flow damper which has recently been designed and is currently under construction is shown in Figure 19. A full set of detail drawings is included as Appendix B.

It is recommended that the new MR damper be used in two parallel exercises:

- implementation of closed-loop control of the vibration isolator using the technique described by Yang (2000);
- development of an effective mathematical model of the MR damper itself which accounts for both electromagnetic forces and those developed with the MR fluid.

The first exercise would provide validation of the simulation results which were described earlier in the present report. These results (see Figures 17 and 18) indicate that significantly superior performance is available using a simple, well-established switching strategy. The control hardware is already in place to implement this control strategy, having been successfully applied to the modelling and control of an ER long-stroke vibration damper (Sims et al., 1999, 2000; Sims, 2000) and also to active constrained layer damping applied to a damped-clamped plate (Chantalakhana and Stanway, 2000(a); 2000(b); Chantalakhana, 2000). Copies of the papers describing the key control studies (Sims et al, 1999; Chantalakhana and Stanway, 2000) are included as Appendices C and D).

The second exercise is required for two reasons. First, to extend our understanding of the operation of the MR squeeze-flow damper and lead to the development of systematic guidelines for designing such devices. Fundamental studies in collaboration with the University of Liverpool, and involving ER fluids in dynamic squeeze flow, continue to demonstrate how little we know about many of the basic operating mechanisms (El Wahed et al., 1998(a), 1998(b), 1999). Second, to investigate the use of pure electromagnetic damping for vibration suppression. The feasibility of pursuing this latter option has been demonstrated conclusively in the present study.

LITERATURE CITED

Bender, E. K., 1968. "Optimum linear preview control with application to vehicle suspension". ASME Journal of Basic Engineering, **90**, pp. 213-221.

Chantalakhana, C., 2000(a). "Model-based Control of Plate Vibrations using Active Constrained Layer Damping". PhD Thesis, University of Sheffield.

Chantalakhana, C. and Stanway, R., 2000(b). "Active constrained layer damping of damped-clamped plate vibrations". Journal of Sound and Vibration, submitted.

Chantalakhana, C. and Stanway, R., 2000(c). "Active constrained layer damping of plate vibrations: a numerical and experimental study of modal controllers". Smart Materials and Structures, submitted.

El Wahed, A. K., Sproston, J. L. and Stanway, R., 1998(a). "The performance of an ER fluid in dynamic squeeze-flow: the influence of particle size". Journal of Colloid and Interface Science, **211**, pp. 264-280.

El Wahed, A. K., Sproston, J. L. and Stanway, R., 1998(b). "The performance of an ER fluid in dynamic squeeze-flow under constant voltage and constant field". Journal of Physics D: Applied Physics, **31**, pp. 2964-2974.

El Wahed, A. K., Sproston, J. L. and Stanway, R., 1999. "Dynamic performance of an ER fluid vibration damper under AC excitation". Journal of Intelligent Materials and Structures, **9**, pp. 772-779.

Jolly, M. R. and Carlson, J. D., 1996. "Controllable squeeze film damping using magneto-rheological fluid". Proceedings "Actuator '96", Bremen, Germany, pp. 333-336.

Jolly, M. R. and Bender, J. W. and Carlson, J. D., 1998. "Properties and applications of commercial magneto-rheological fluids". Proceedings SPIE 5th Annual Symposium on "Smart Structures and Materials", San Diego, CA.

Karnopp, D. C., Crosby, M. J. and Harwood, R. A., 1974. "Vibration control using semi-active force generators". ASME Journal of Engineering for Industry, **96**, pp. 619-626.

Sims, N. D., Stanway, R. and Johnson, A. R., 1999. "Vibration control using smart fluids: a state-of-the-art review". The Shock and Vibration Digest, **31**, pp. 195-203.

Sims, N. D., Peel, D. J., Stanway, R., Johnson, A. R. and Bullough, W. A., 2000. "The ER long-stroke damper: a new modelling technique with experimental validation". Journal of Sound and Vibration, **229**, pp. 207-227.

Sims, N. D., Stanway, R., Peel, D. J., Bullough, W. A. and Johnson, A. R., 1999. "Controllable viscous damping: an experimental study of an ER damper under proportional feedback control". Smart Materials and Structures, **8**, pp. 601-605.

Sims, N. D., 2000. "Modelling and control of an electro-rheological long-stroke vibration damper". PhD Thesis, University of Sheffield.

Stanway, R., Sproston, J. L., Prendergast, M. J., Case, J. R., and Wilne, C. E., 1992. "ER fluids in the squeeze-flow mode, an application to vibration isolation", Journal of Electrostatics, **38**, pp. 89-94.

Stanway, R., Sims, N. D., Johnson, A. R. and Mellor, P. H., 2000. "Modelling and control of an MR vibration isolator", to be presented at the 7th SPIE International Symposium on "Smart Structures and Materials", Newport Beach, 5-9th March.

Yang, J. S., 2000. "Vibration isolation using an MR squeeze-flow damper: a modelling and control study". MPhil Thesis, University of Sheffield.

Wong, A. S., 1999. "Application of a magneto-rheological short-stroke damper". B.Eng Final-Year Project Dissertation, University of Sheffield.

ACKNOWLEDGEMENTS

The authors of this final report are grateful to Dr Mark Jolly of Lord Corporation for the loan of the MR squeeze-flow damper.

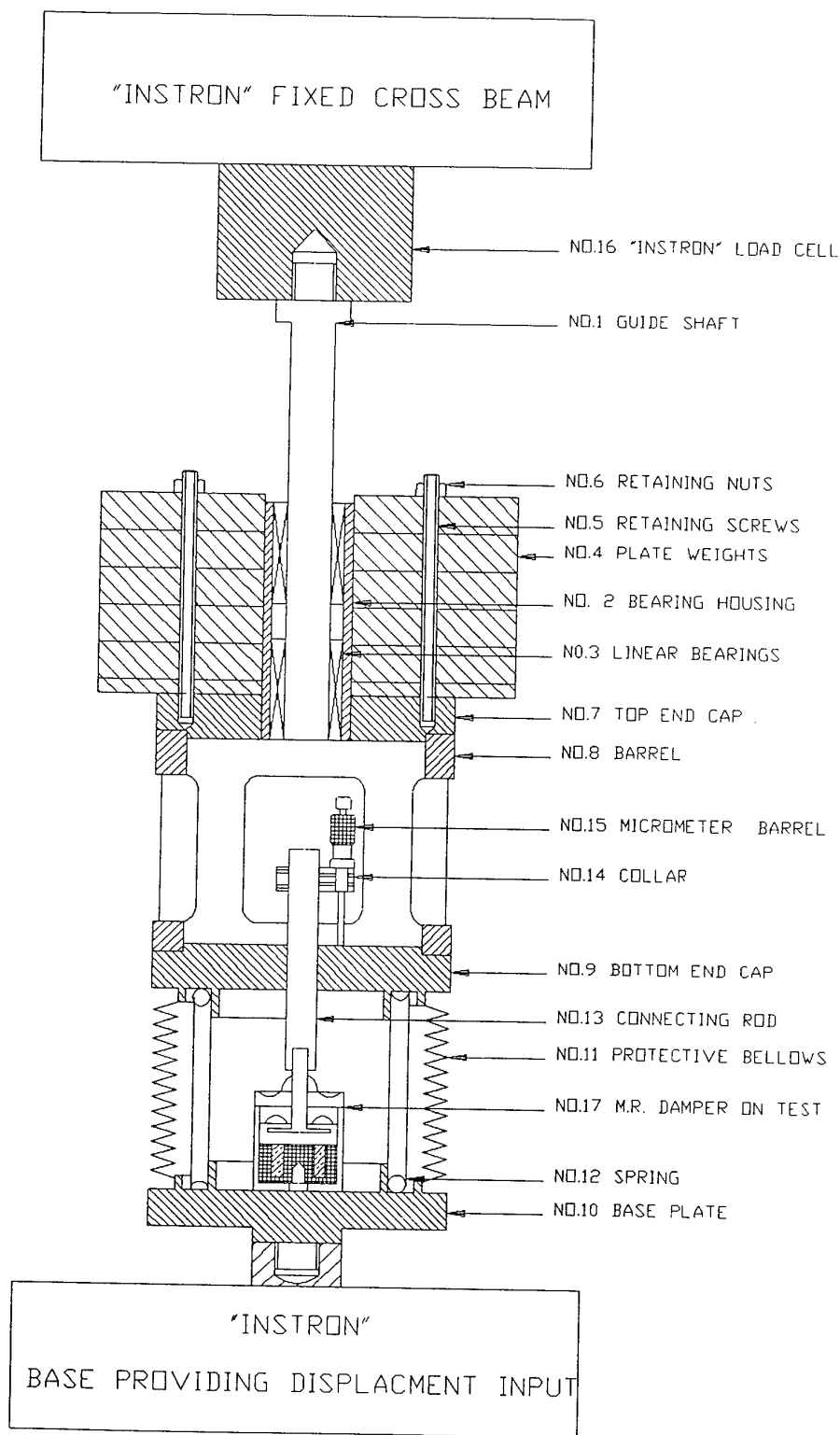


Figure 1 Arrangement drawing of test facility

TITLE: General Assembly	PART NO: G.A.	MATERIAL: Various	PROJECTION: First Angle	SCALE: 1:5
ALL DIMENSIONS IN MM	TOLERANCE: ± 0.2 MM UNLESS OTHERWISE STATED	DRAWN BY: A. Godbehare	DATE: 9/7/98	DRAWING NUMBER: AI-GA
NOTES:	REVISIONS:			

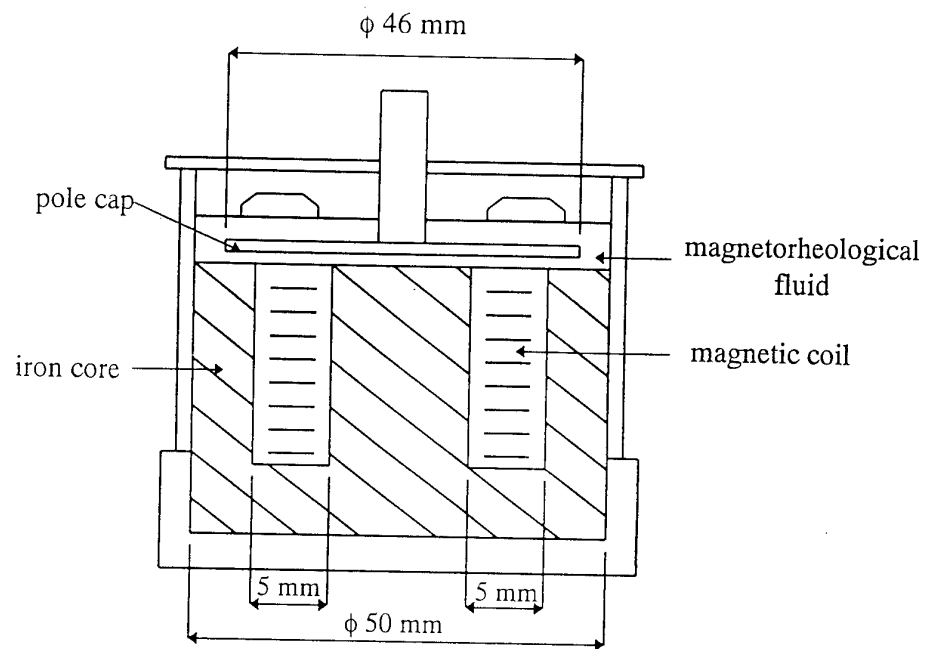


Figure 2. MR squeeze-flow damper.

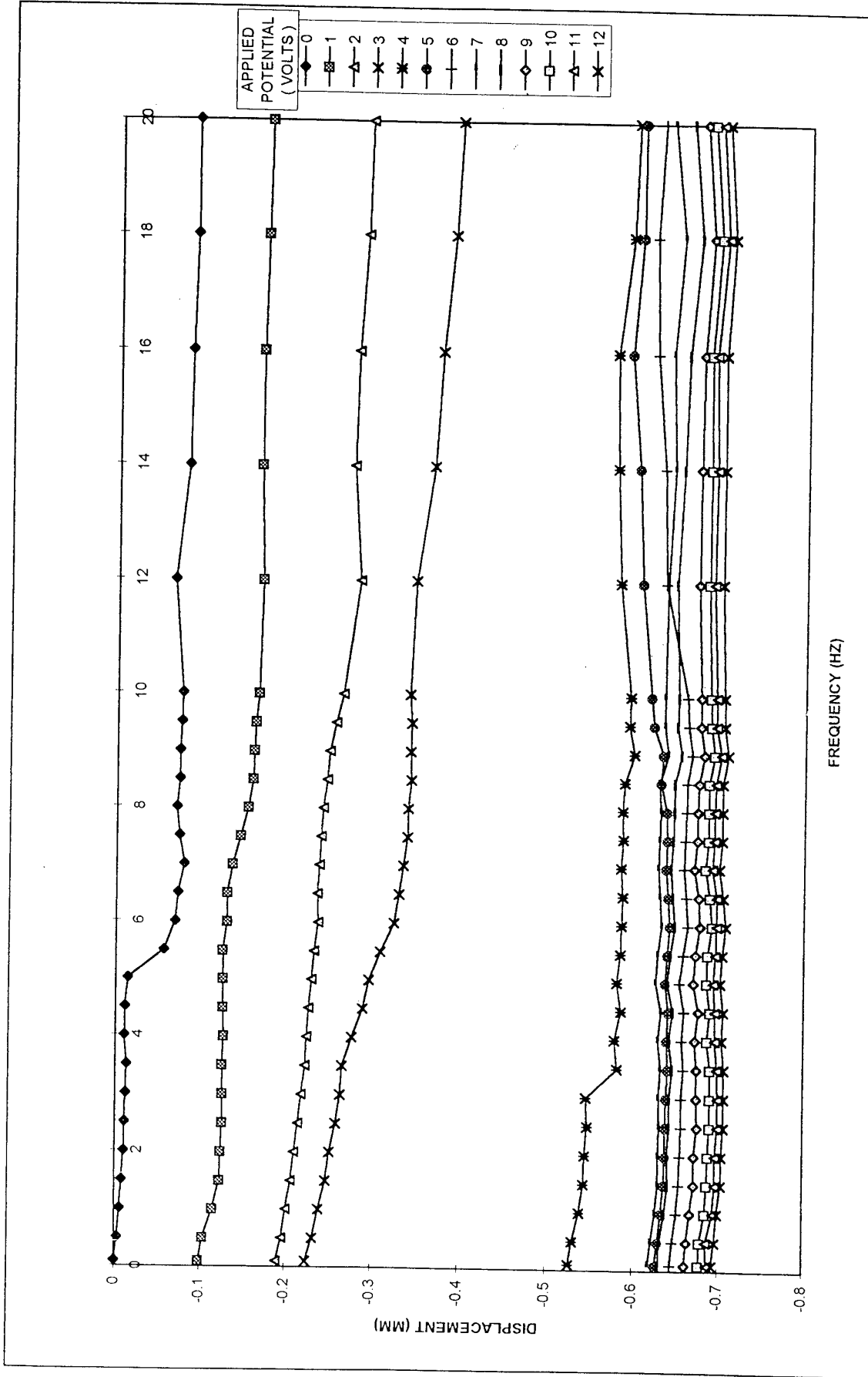


Figure 3. Effect of applied voltage on mean level of oscillation.

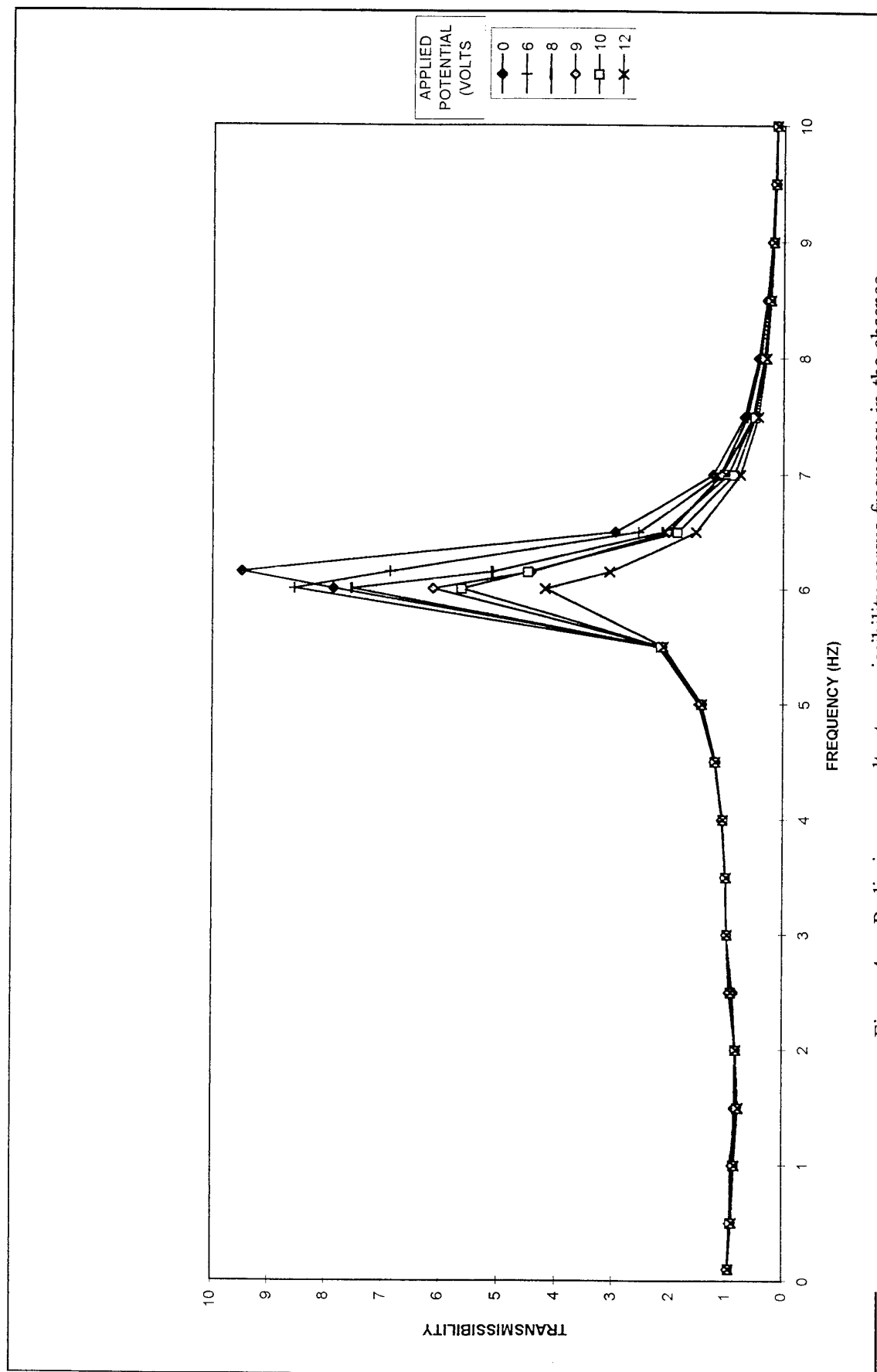


Figure 4. Preliminary results: transmissibility versus frequency in the absence of MR fluid. Initial interpole gap 2mm.

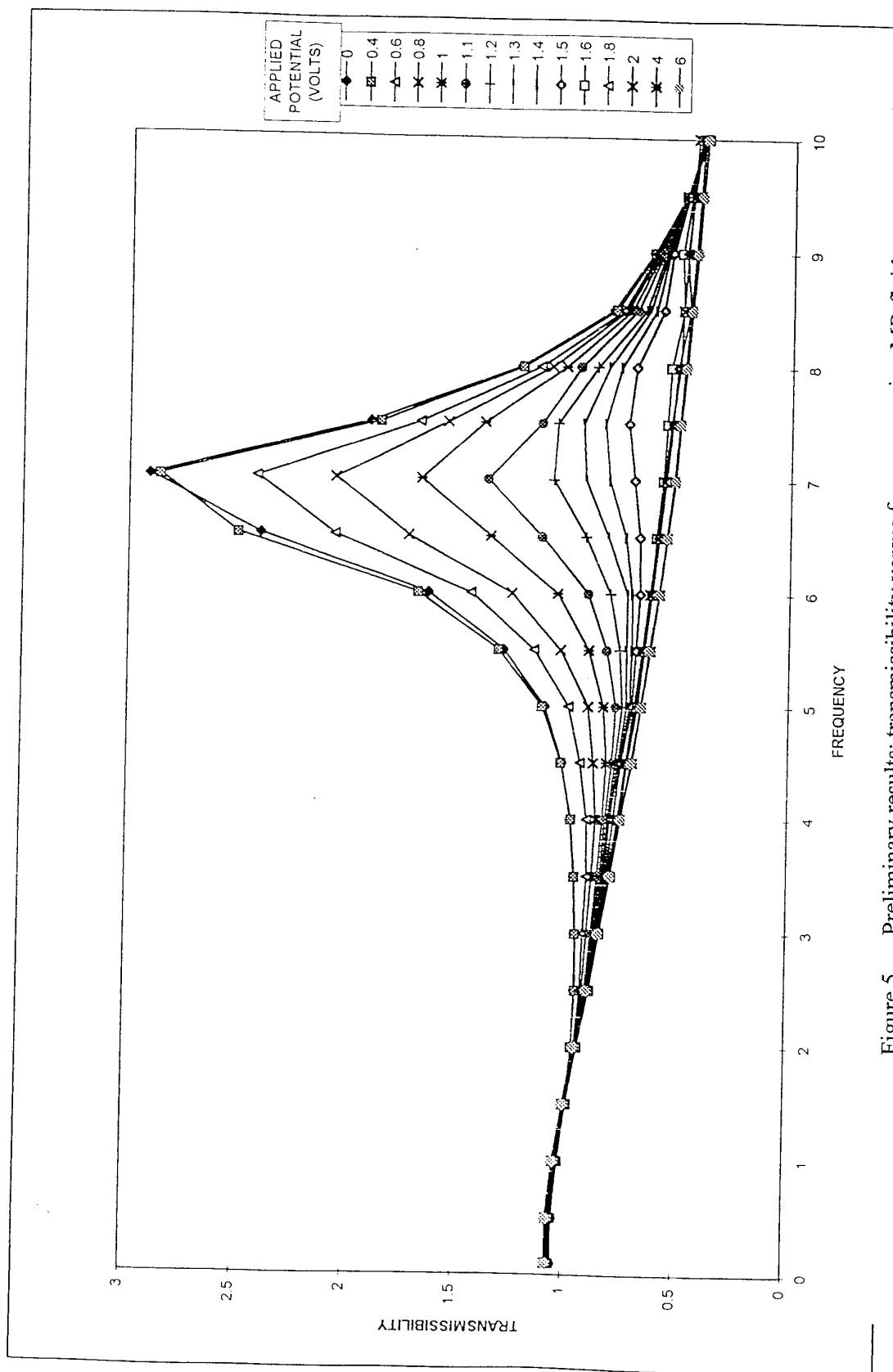


Figure 5. Preliminary results: transmissibility versus frequency using MR fluid.
Initial interpole gap 2 mm.

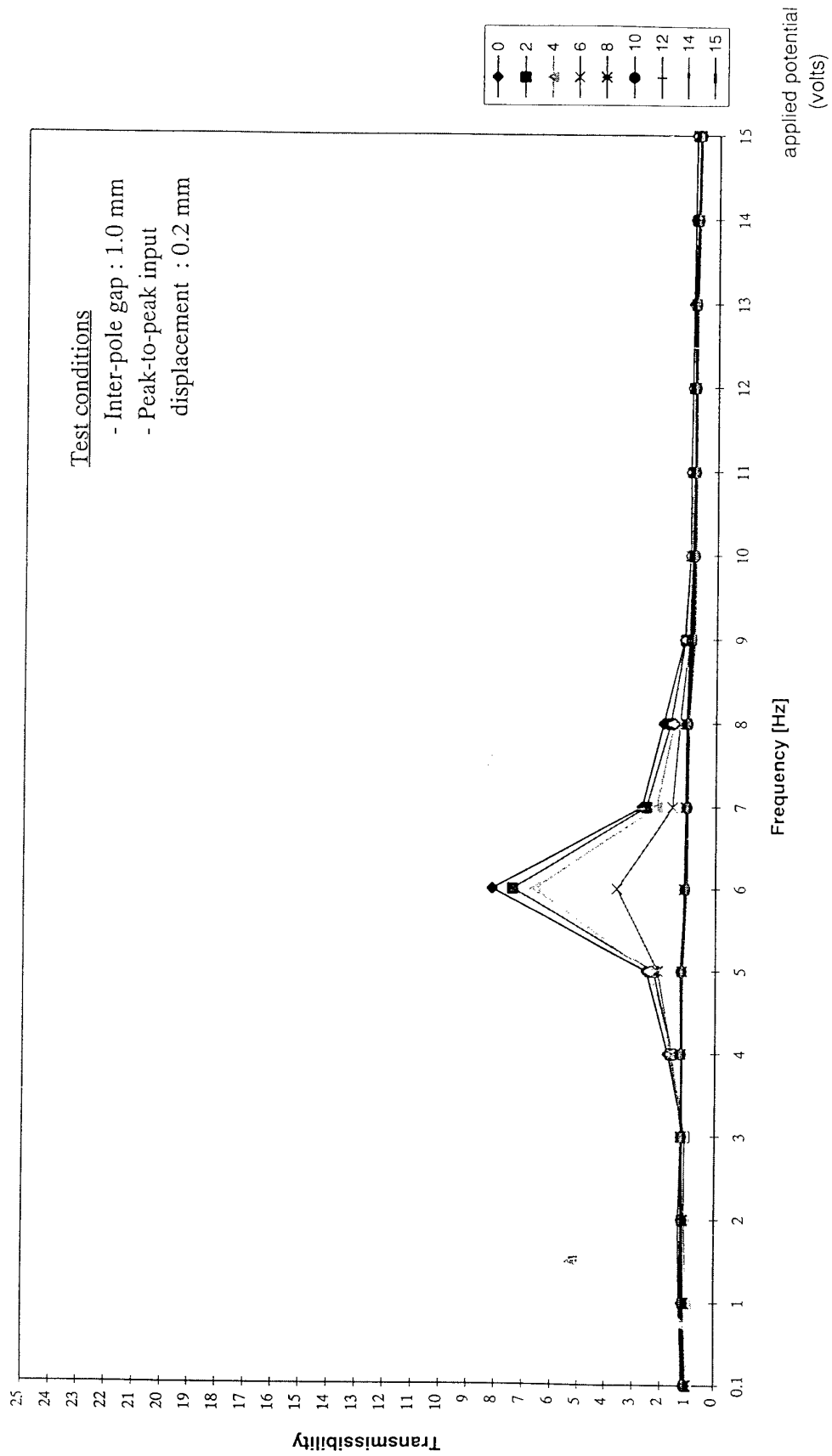


Figure 6. Transmissibility versus frequency in the absence of MR fluid. Initial interpole gap 1 mm.

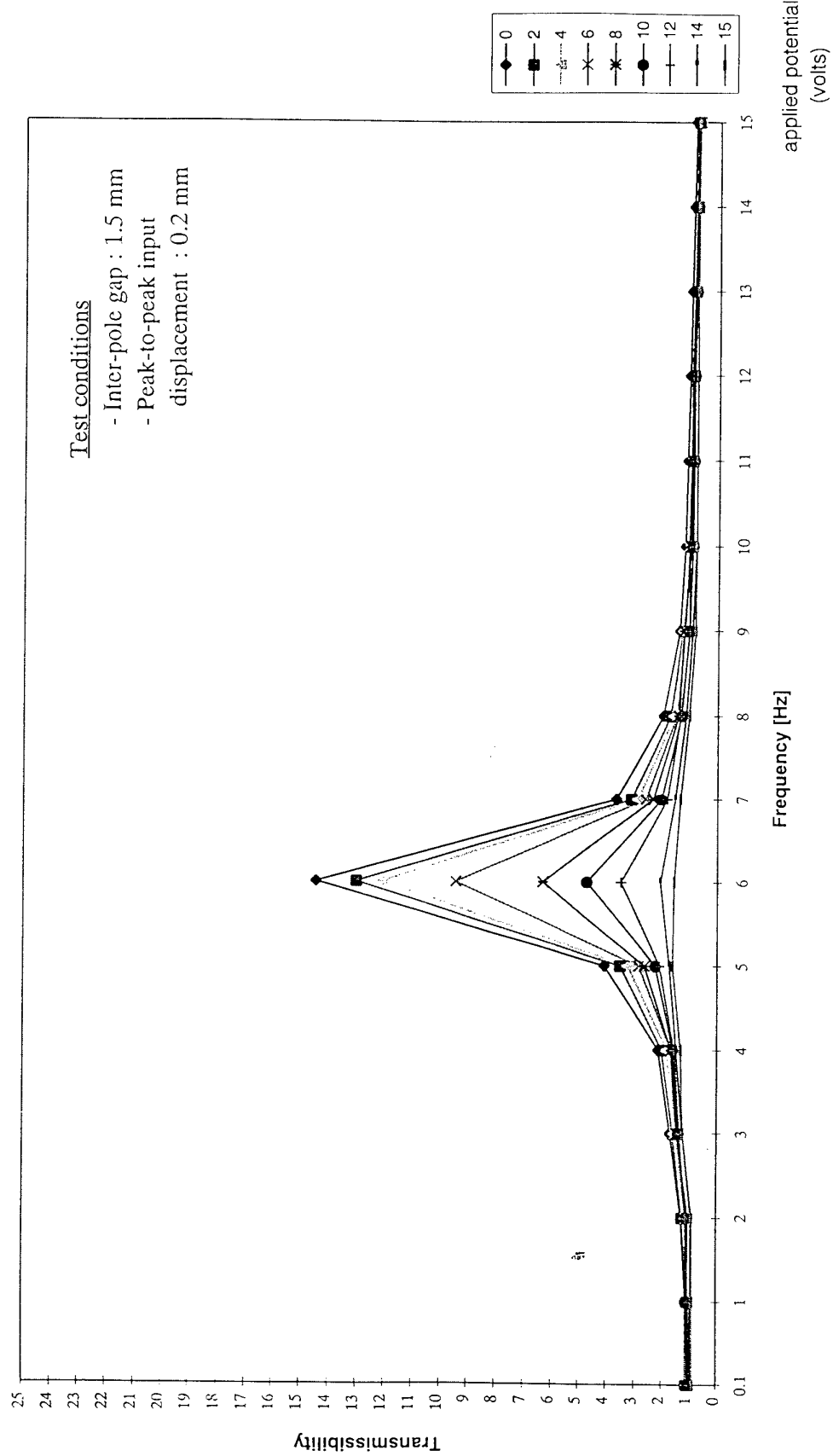


Figure 7. Transmissibility versus frequency in the absence of MR fluid. Initial interpole gap 1.5 mm.

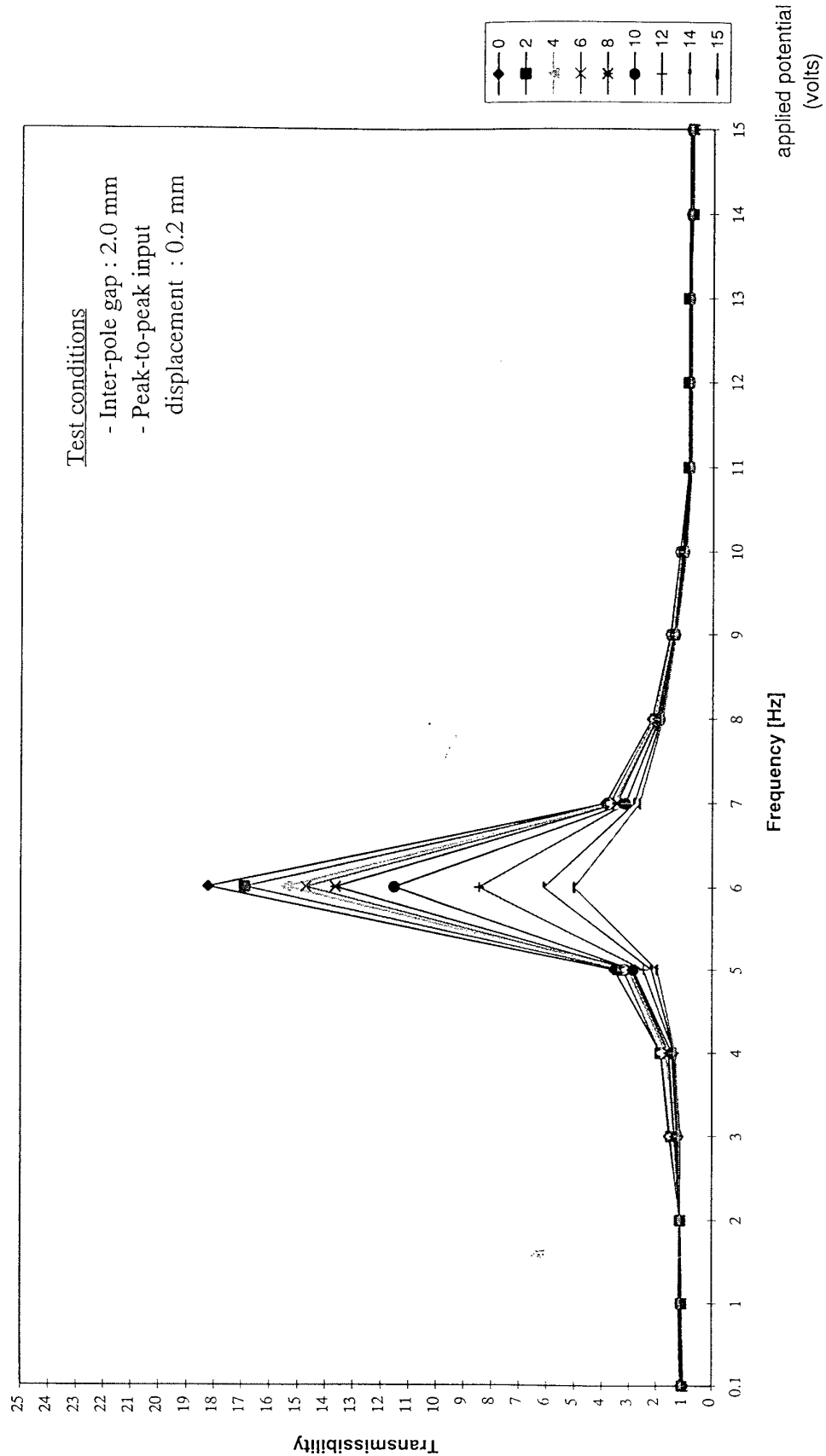


Figure 8. Transmissibility versus frequency in the absence of MR fluid. Initial interpole gap 2 mm.

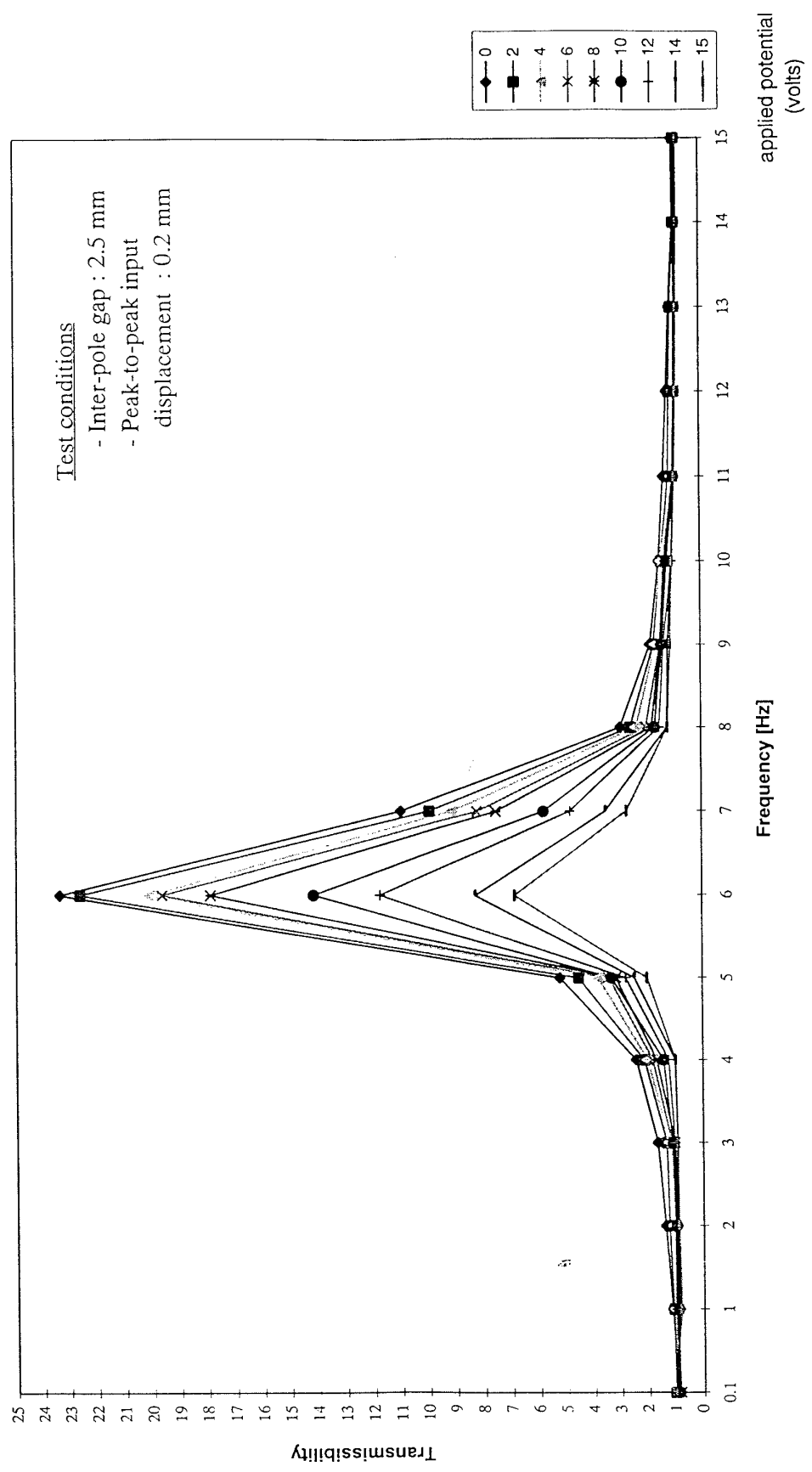


Figure 9. Transmissibility versus frequency in the absence of MR fluid. Initial interpole gap 2.5 mm.

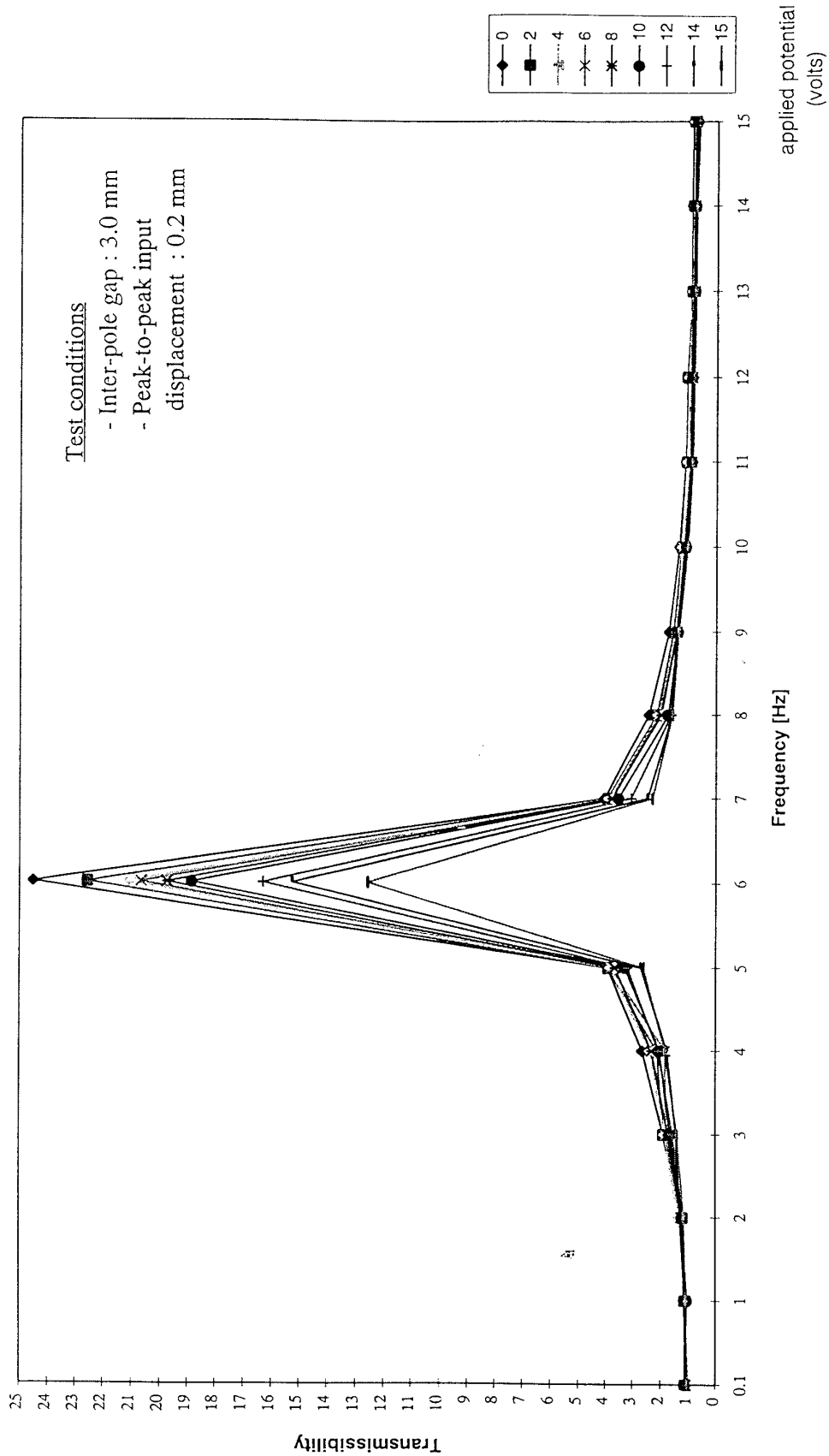


Figure 10. Transmissibility versus frequency in the absence of MR fluid. Initial interpole gap 3 mm.

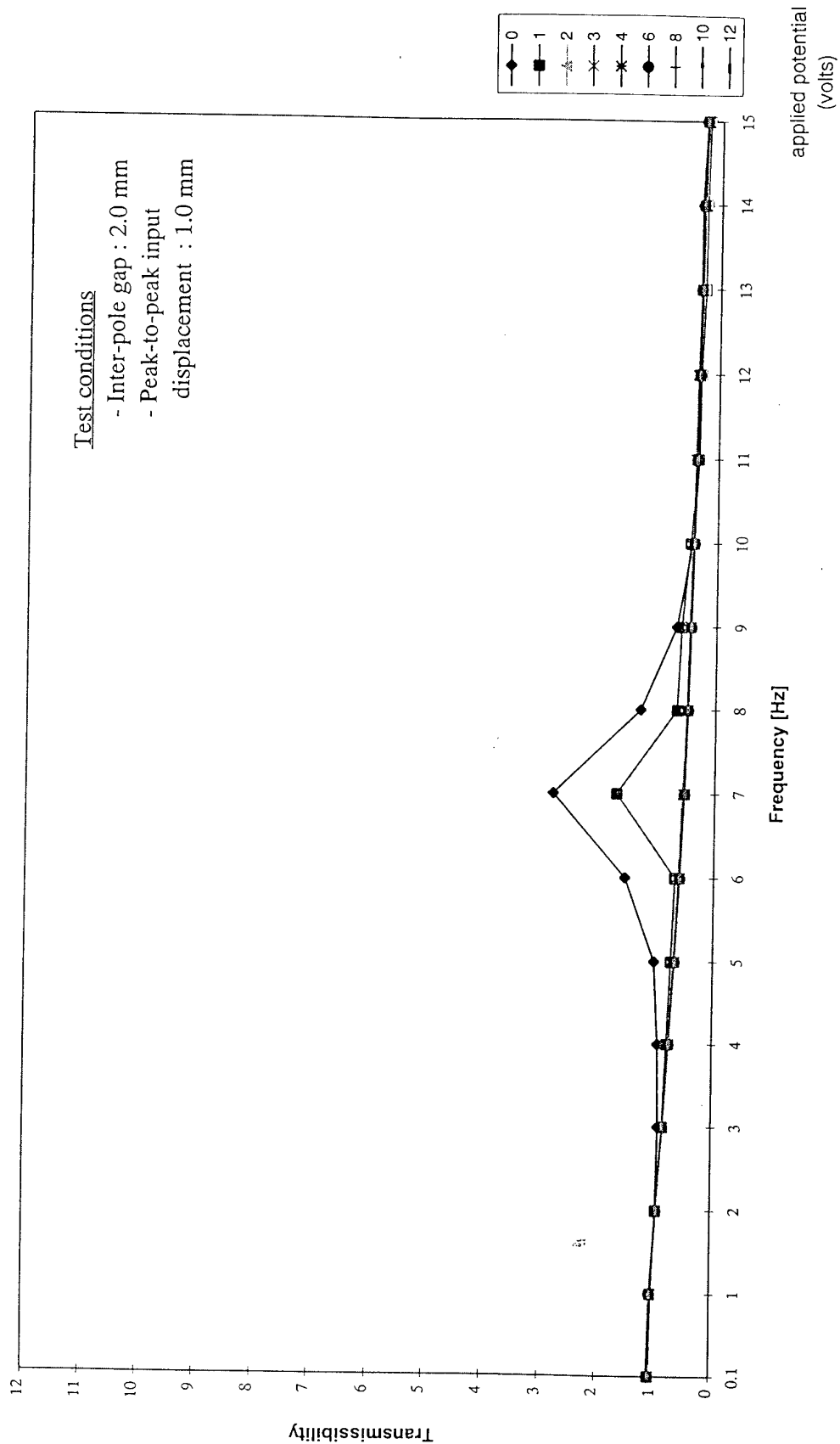


Figure 11. Transmissibility versus frequency using MR fluid. Initial interpole gap 2 mm.

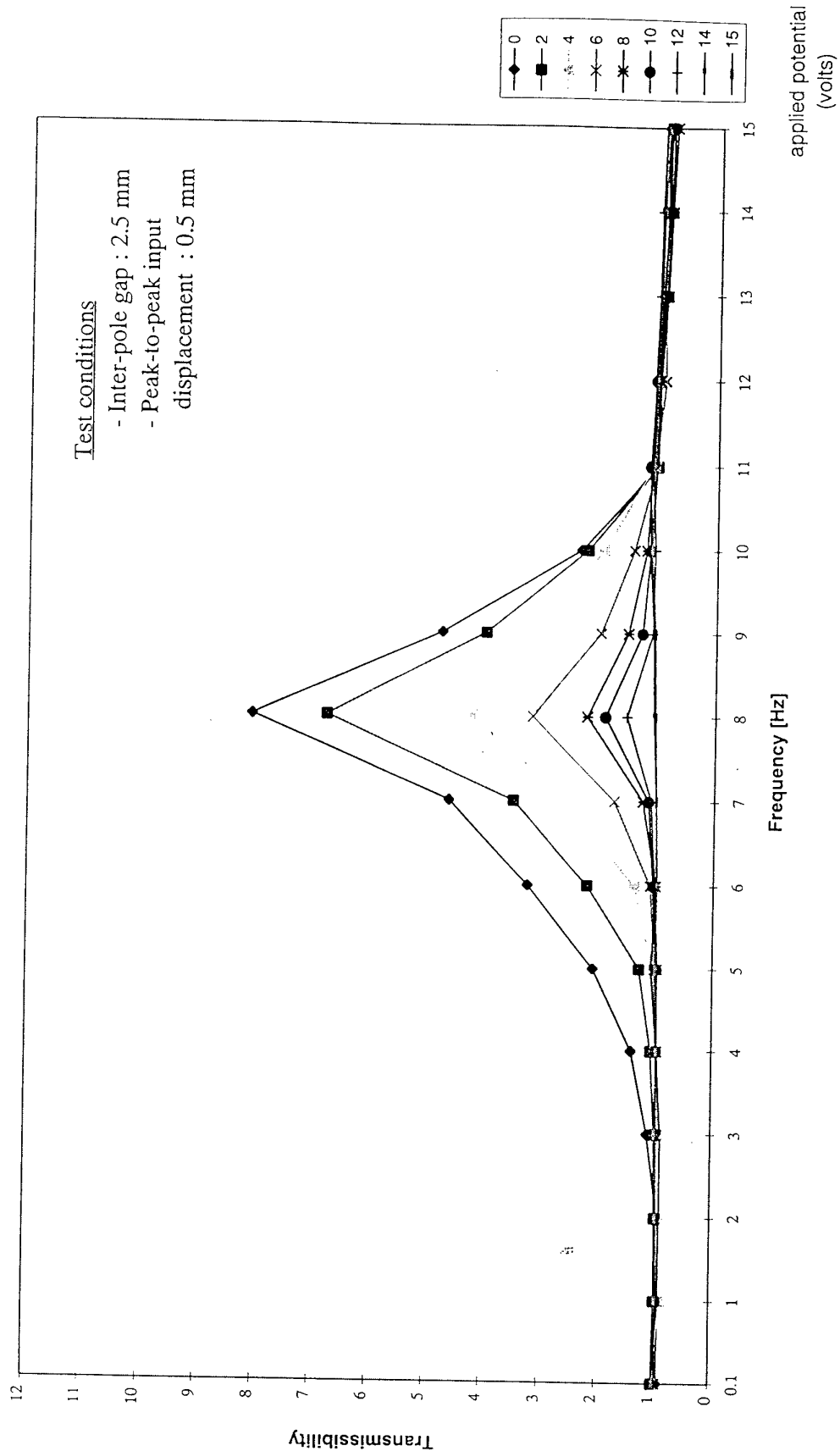


Figure 12. Transmissibility versus frequency using MR fluid. Initial interpole gap 2.5 mm.

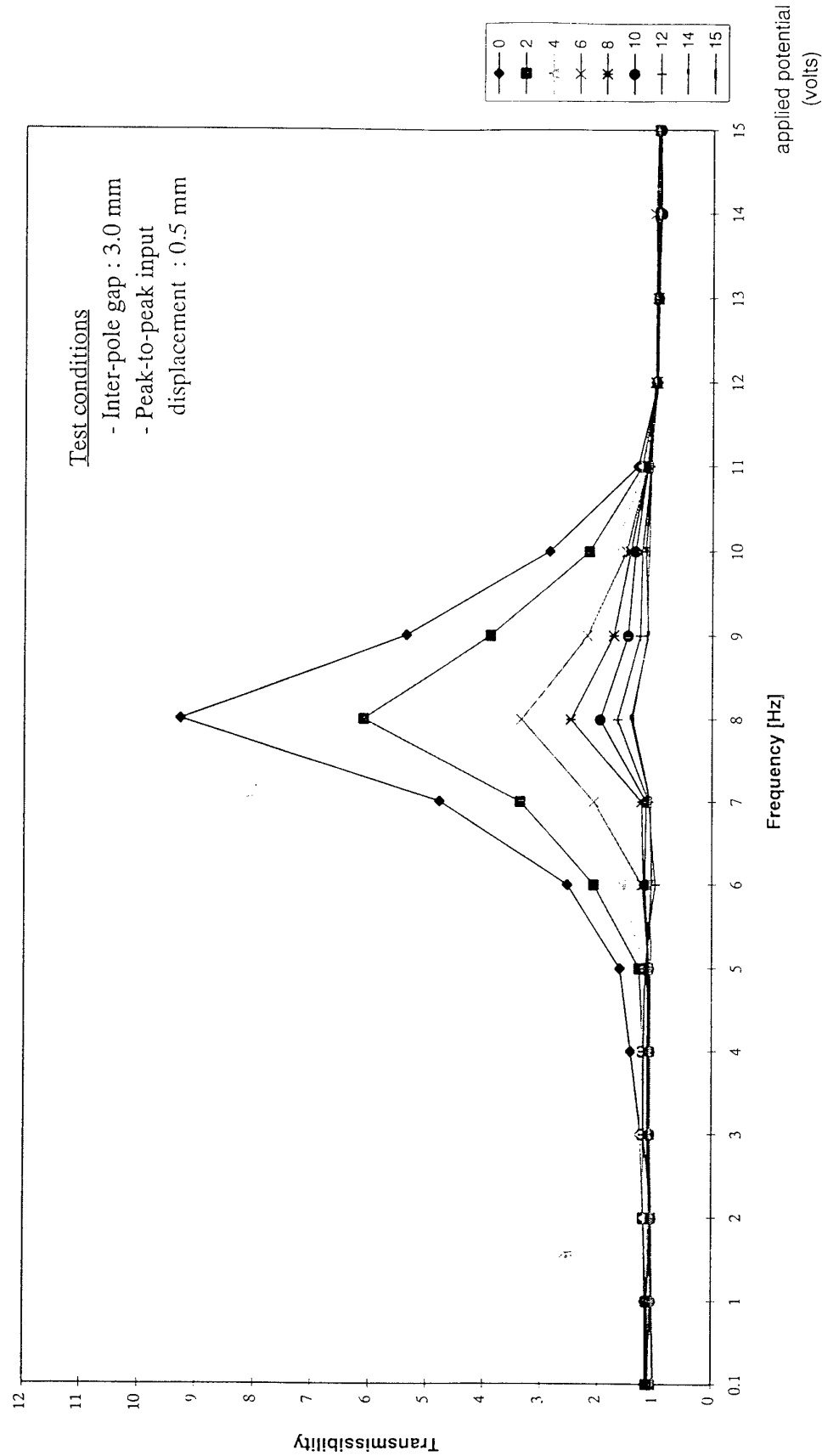


Figure 13. Transmissibility versus frequency using MR fluid. Initial interpole gap 3 mm.

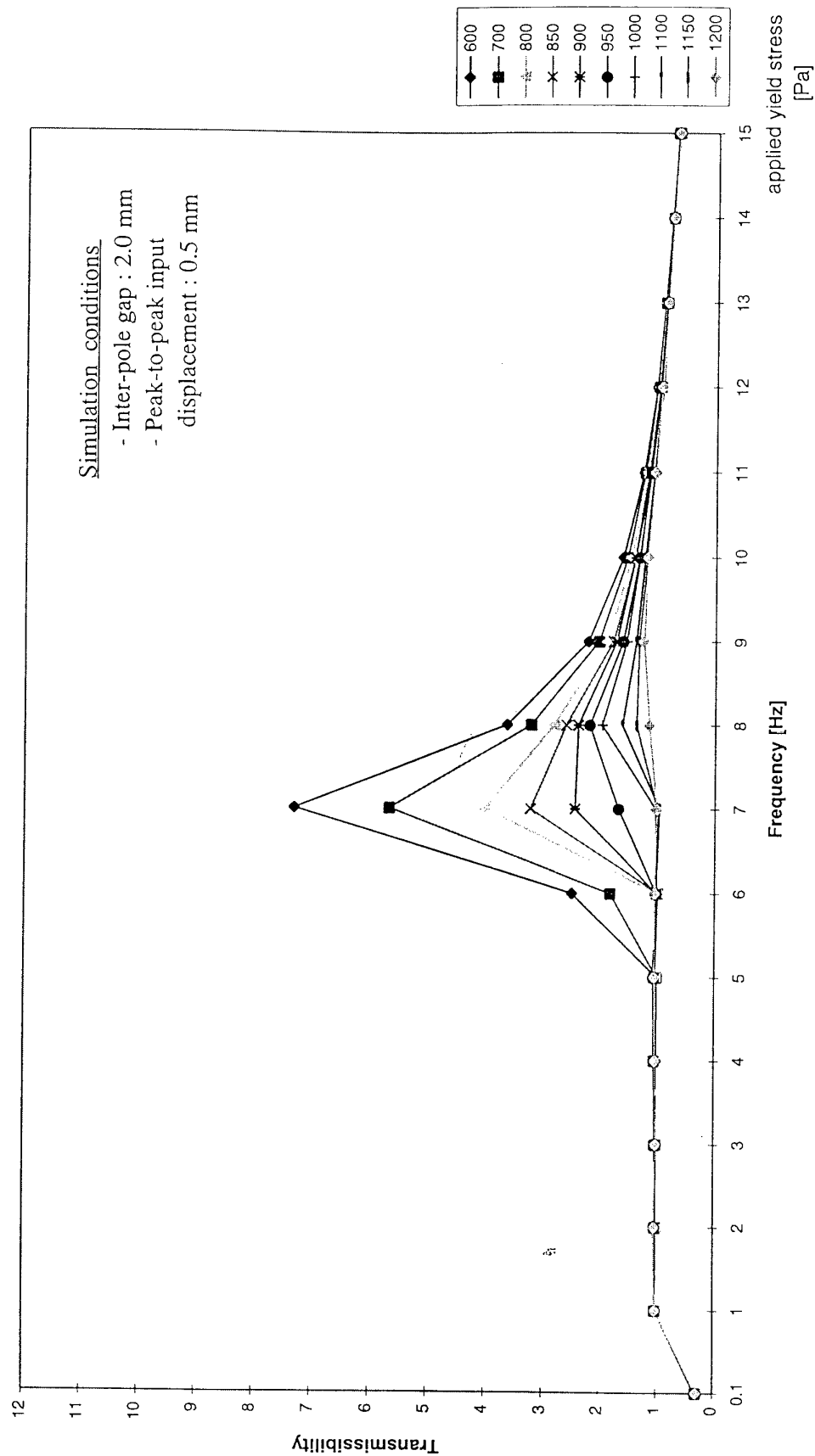


Figure 14. Simulation results. Transmissibility: open-loop control using MR fluid. Initial interpole gap 2 mm.

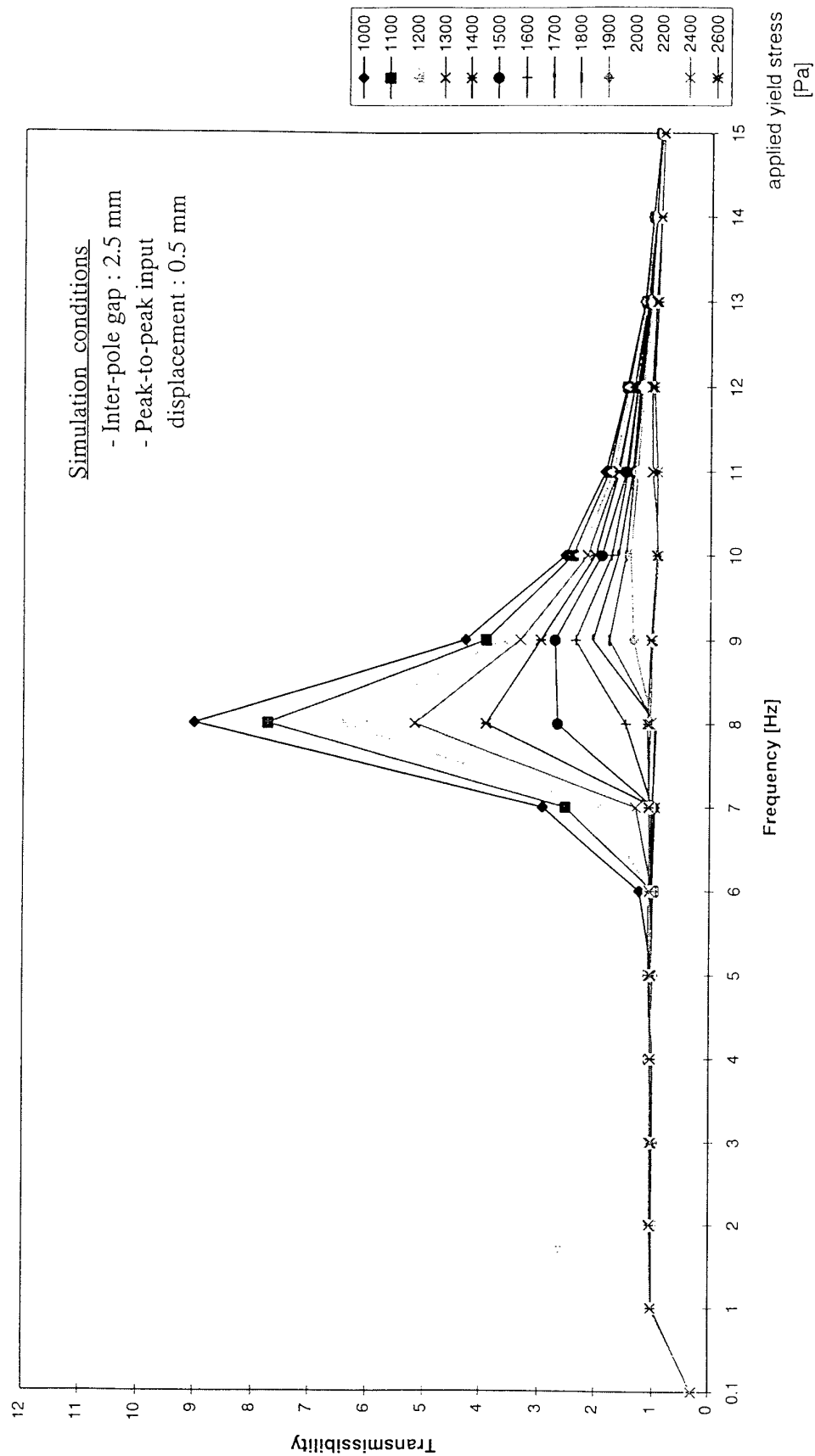


Figure 15. Simulation results. Transmissibility: open-loop control using MR fluid. Initial interpole gap 2.5 mm.

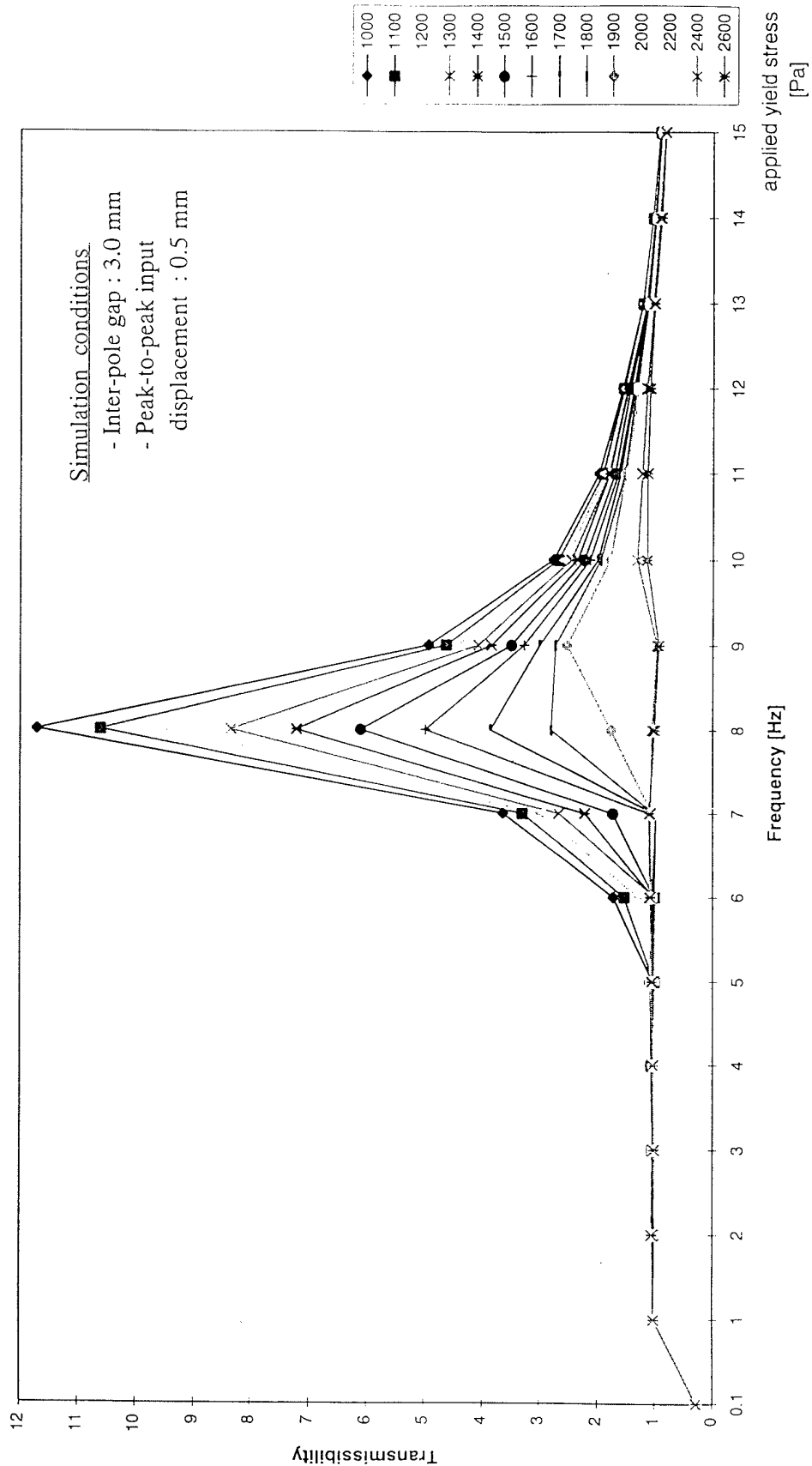


Figure 16. Simulation results. Transmissibility: open-loop control using MR fluid. Initial interpole gap 3 mm.

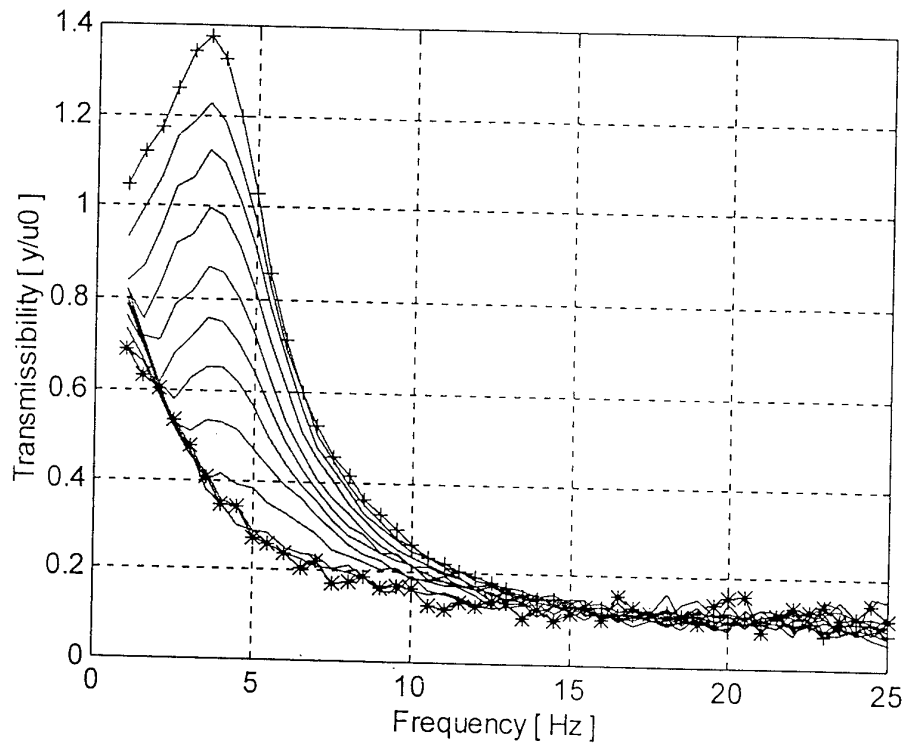


Figure 17. Simulation results. Closed-loop control of transmissibility with ideal switching strategy.

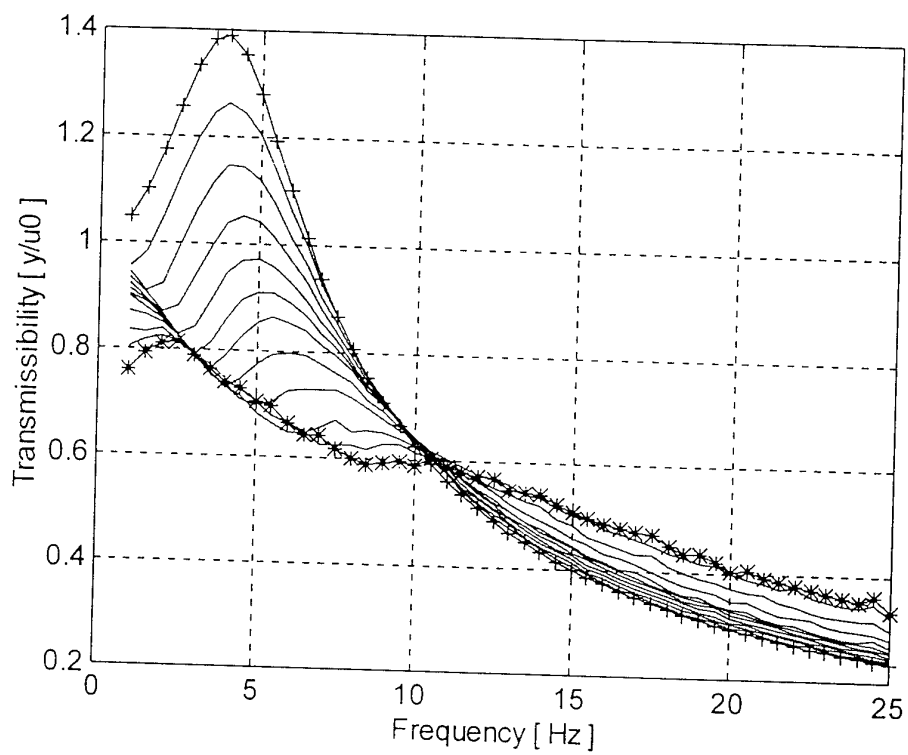


Figure 18. Simulation results. Closed-loop control of transmissibility taking account of base viscosity of MR fluid.

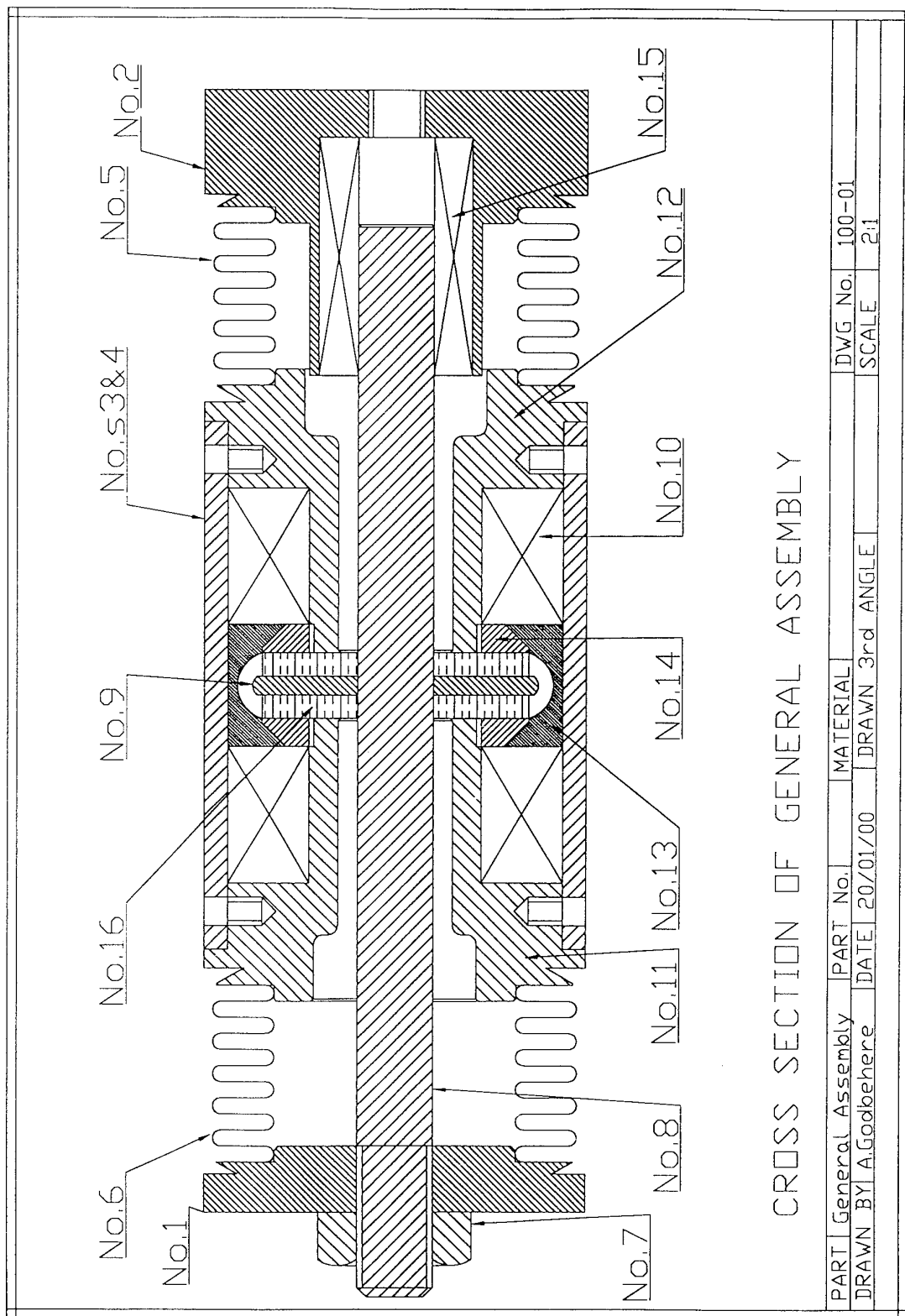


Figure 19. Proposed design for MR squeeze-flow damper, Mark II.

APPENDIX A

Copy of Stanway, R., Sims, N. D., Johnson, A. R. and Mellor, P. H., 2000.
"Modelling and control of an MR vibration isolator", to be presented at the 7th
SPIE International Symposium on "Smart Structures and Materials", Newport
Beach, 5th-9th March.

Modelling and control of a magnetorheological vibration isolator

Roger Stanway*, Neil D Sims and Andrew R Johnson

University of Sheffield
Department of Mechanical Engineering
Mappin Street
Sheffield, S1 3JD, United Kingdom

ABSTRACT

It is now well established that magnetorheological (MR) fluids can provide the basis for constructing controllable vibration damping devices. Moreover, the characteristics of MR fluids are generally compatible with industrial requirements and there is enormous scope for commercial exploitation. In this paper the authors describe the design and construction of a vibration isolator which incorporates an MR damper. The damper is unusual in that it operates in the squeeze-flow mode. A quasi-steady model of the MR damper is summarized and then extended to include the vibration isolator dynamics. Model predictions are compared with experimental results. It is shown that by employing the MR damper a wide range of control can be exercised over the transmissibility of the vibration isolator. Numerical experiments are used to show that a feedback control strategy can provide even more control over transmissibility.

1. NOMENCLATURE

F	total force developed by MR fluid
k	spring stiffness
m	supported mass
P_0	nominal pressure
r_0	radius of pole face, MR damper
x_0	inter-pole gap
x, \dot{x}, \ddot{x}	displacement, velocity acceleration of upper pole
y	displacement of supplied mass
z, \dot{z}, \ddot{z}	relative displacement, velocity and acceleration
μ	fluid viscosity
ρ	fluid density

2. INTRODUCTION

The feasibility of constructing a controllable vibration isolator based upon an electrorheological (ER) squeeze-flow damper was established some years ago (Stanway et al. 1992). Subsequent investigations focussed on modeling the ER fluid in squeeze-flow, both to account for observed behavior and to gain a better understanding of physical mechanisms (Williams et al. 1994). Our understanding of ER squeeze-flow behavior continues to improve through detailed studies into the influence of factors such as particle size (El Wahed et al. 1999) and the form of the applied electric field (El Wahed et al. 1998).

Given the successful operation of the ER-based vibration isolator and the simplicity and compactness of its construction, it may seem surprising that commercial exploitation did not follow. The main reason for the reluctance of industry to develop this form of device is the operating characteristics of the ER fluids themselves, notably the need to provide electric field strengths of up to 8kV/mm, the perceived sensitivity of ER fluids to temperature effects and the limited temperature range. What has emerged as a direct result of the development of prototype ER squeeze-flow dampers and associated modelling techniques is a range of controllable dampers which employ magneto-rheological (MR) fluids in squeeze-flow (Jolly et al. 1998).

* Correspondence: Telephone: (0114) 22 27728 Fax: (0114) 22 27890 Email: r.stanway@sheffield.ac.uk

Over the past few years MR fluids have enjoyed a rapid rise to prominence as the smart fluid which is ideally suited for commercial exploitation. MR fluids are capable of generating substantially greater force levels than comparable ER devices, are less sensitive to environmental changes and operate over a wider temperature range. However, the overriding advantage of MR over ER fluids arises from the way in which control is exercised. MR fluids are excited by a magnetic field rather than the electric field used to excite ER fluids. This magnetic field can be generated by an electromagnetic circuit which requires only a low voltage electrical source. As a result there appears to be tremendous potential for the application of MR squeeze-flow dampers in vibration isolation applications.

To examine the use of an MR squeeze-flow damper in a vibration isolation context, a new experimental facility has been built. The construction follows the general outline of the apparatus described by Stanway et al (1992) but with an MR damper in place of the ER device. In what follows here the authors describe the experimental facility and then develop a quasi-steady mathematical model to account for its observed behavior. Experimental results are presented to show that full control over transmissibility is available through the MR damper. However, further work is required to extend the quasi-steady model so that it is able to account for the observed behavior of the MR-based vibration isolator. Numerical experiments are used to examine the effect of feedback control on vibration isolation.

3. EXPERIMENTAL FACILITY

In the experimental work described by Stanway and his colleagues (1992) the stated aim was to develop a vibration isolator capable of performing as a controllable automotive engine mount. To this end the supported mass was chosen to be 60kg with a supporting spring of stiffness 50kN/m. This arrangement which provides a structure with a (undamped) natural frequency of approximately 5Hz, was adopted for the present test facility. The only modification made was to build the supported mass in sections, each of mass 10kg, so that higher natural frequencies can be obtained using the same spring. The general arrangement of the vibration isolator is shown in Figure 1.

Referring to Figure 1, the MR squeeze-flow device is placed in parallel with the supporting spring, i.e. between the base and the supported mass. The present damper is a device on loan from Lord Corporation and is described in a previous paper (Jolly and Carlson, 1996). A fine adjustment mechanism incorporating a micrometer barrel allows accurate setting of the inter-pole gap. For the tests described here an inter-pole gap of 2mm was used.

The base of the isolator is connected to a servo-hydraulic test machine ('Instron' model 8501) which provides the displacement input to the isolator. The machine is capable of providing controlled displacements of up to ± 50 mm over the frequency range from zero to 200Hz. The mass carriage translates vertically in response to this displacement input. The carriage movement is constrained by a linear bearing and guide shaft. The upper end of the guide shaft is firmly fixed to the upper cross beam of the test machine.

The excitation provided to the base of the isolator is measured directly from the control panel of the test machine. The response of the mass carriage is measured using an LVDT connected to an oscilloscope. The MR fluid is excited using a combination of a signal generator and power amplifier.

4. MATHEMATIC MODELLING

1. Model of the MR Damper

The basis of our mathematical model is the analysis of a simple squeeze-film device presented by Jolly and Carlson. This analysis derives from the physical representation shown in Figure 2. With reference to Figure 2, MR fluid is contained between two poles of radius r_0 . The nominal thickness of the fluid film (i.e. the initial inter-pole gap) is x_0 . A downward displacement of the upper pole, denoted x , compresses the fluid and imposes a radial flow. It is assumed that the fluid pressure (and the resulting force) is the sum of pressure contributions due to viscosity of the carrier liquid, fluid inertia and magnetic field effects. There is also a force arising from the nominal pressure measured at $r=0$. These force expressions are as follows:

1. Force due to viscosity

$$f_1 = \frac{3}{2} \mu r_0^4 \frac{\dot{x}}{(x_0 - x)^3} \quad (1)$$

where μ is the fluid viscosity and \dot{x} denotes the velocity of the upper pole.

2. Force due to fluid inertia

$$f_2 = \frac{\rho r_0}{8} \ddot{x} + \frac{\dot{x}^2}{(x_0 - x)^3} \quad (2)$$

where ρ is the fluid density and \ddot{x} denotes the acceleration of the upper pole.

3. Force due to MR effect

$$f_3 = \frac{4}{3} \pi r_0^3 \tau_y \frac{\text{sgn}(\dot{x})}{(x_0 - x)} \quad (3)$$

where τ_y is the yield stress induced by the applied magnetic field. And finally

4. Force due to nominal pressure P_0

$$f_4 = \pi r_0^2 P_0 \quad (4)$$

The total force developed within the fluid is then given by

$$F = f_1 + f_2 + f_3 + f_4 \quad (5)$$

2. Model of MR-based Vibration Isolator

A lumped model of the MR-based vibration isolator is shown in Figure 3. Referring to Figure 3, the supported mass is denoted by m and its displacement by x . The spring stiffness is denoted by k and the motion at the base of the spring is denoted by y . The MR damper develops a force which (from equations (1), (2) and (3)) is a function of z , \dot{z} , \ddot{z} , respectively the relative displacement, velocity and acceleration across the damper's poles. The corresponding equation of motion for the vibration isolator is therefore

$$kz + f(z, \dot{z}, \ddot{z}) = m\ddot{x} \quad (6)$$

where $z = y - x$ is the relative displacement across the spring and MR damper and f is the non-linear damping function developed in equations (1) to (5). The equation of motion can be expressed in block diagram form, Figure 4, and then solved using modern simulation software (The Mathworks, 1998).

5. EXPERIMENTAL PROCEDURE AND RESULTS

Two sets of experiments have been completed. These both involve measuring the transmissibility of the vibration isolator as a function of applied excitation to the MR damper, one in the absence of MR fluid, one with a commercial MR fluid (Lord Corporation type MRF-240BS) in the damper.

A typical set of results obtained in the absence of MR fluid are shown in Figure 5. The initial gap was set at 2mm and an input displacement of 0.2mm peak-to-peak was applied to the base of the isolator. Referring to Figure 5, the peak transmissibility is approximately 9.5 at just above 6Hz. Increasing the voltage applied to the MR damper up to 12 volts causes a reduction in peak transmissibility to approximately 4.2 at 6Hz. Given that the initial gap was set at a relatively large value and that electromagnetic forces will rise dramatically as the gap is reduced, the results indicate that it is worthwhile investigating purely electromagnetic damping as means of providing controllable isolation. Also the results indicate that electromagnetic forces need to be incorporated into the mathematical model of the MR damper.

The results obtained with MR fluid are shown in Figure 6. Referring to Figure 6, it is clear that the MR damper provides a vibration damper whose transmissibility can be controlled over a wide range. With zero applied volts the peak

transmissibility is slightly below 3 at 7Hz. The reduction of this value in relation to Figure 5 is due to the damping provided by the base fluid in the absence of an applied magnetic field. Increasing the applied voltage to 6 volts results in the transmissibility reducing to approximately 0.5 at 7Hz. Current experiments are aimed at examining the influence of the inter-pole gap on the transmissibility of the isolator

6. VALIDATION OF THE MATHEMATICAL MODEL

The equation of motion of the complete vibration isolator (i.e. Equation (6)) was solved using Simulink software. The results of the simulation exercise are shown in Figure 7.

Figure 7 displays the transmissibility of the isolator versus mechanical excitation frequency for a range of values of assumed yield stress. Increasing the MR fluid yield stress from 600 to 1200Pa has the effect of reducing the transmissibility from approximately 7 to around unity. By increasing the spring stiffness in the model to correspond to observed behavior, the model predicted resonant frequencies of approximately 7 Hz, which agrees with the experimental results shown in Figure 6.

Further development of the mathematical model is currently in progress. First and foremost there is a need to relate the yield stress developed within the ER fluid to the current supplied to the electromagnetic coil. The influence of electromagnetic forces needs to be examined in more detail. Finally the effective stiffness of the isolator needs to be identified so that the model is able to predict the observed resonant frequency.

7. NUMERICAL EXPERIMENTS TO EXAMINE FEEDBACK CONTROL

From the discussion in the previous section and comparison of Figure 6 and 7, it is apparent that the mathematical model of the MR damper requires further development. However, since the existing model captures the essential features of the observed responses, it was decided to use numerical experiments to examine the behavior of the model under the influence of feedback control on the transmissibility of the vibration isolator. As a first attempt, it was decided to use the model to examine the effect of applying the well-known algorithm due to Karnopp et al (1974). Using a switching strategy based upon the directions of the mass velocity and relative velocity between the mass and the base, the algorithm provides a semi-active approximation to the optimum single-degree-of-freedom isolator which was derived by Bender (1968). Mathematically, the strategy reduces to the following two logic statements:

- if $\dot{x}\dot{z} > 0$, then switch on the MR damper.
- if $\dot{x}\dot{z} < 0$, then switch off the MR damper.

where \dot{x} is the absolute velocity of the isolated mass and \dot{z} is the relative velocity between the mass and the base.

To implement this algorithm experimentally will obviously require additional instrumentation, essentially to provide measurements of the velocities \dot{x} and \dot{z} . However, the numerical results obtained indicate that the performance gains available may well justify the cost of the additional components. Figure 8 shows the influence on transmissibility if the MR damper is switched between zero yield stress and 500 Pa. By switching in this way it appears possible to suppress the resonance and reduce the transmission of higher frequency vibrations. In practice, the results would not be so favorable since with the current to the MR damper's coil switched off, damping forces would still be present, owing essentially to the viscosity of the base liquid. The effect of this inherent viscosity is shown in Figure 9. Perhaps most significantly, the transmissibility characteristics exhibit a crossover above resonance, after the fashion of a linear, single degree-of-freedom vibration isolator. Consequently the most effective control of resonance comes at the expense of less effective suppression of high frequency vibrations. Nevertheless, the simulation results in Figure 9 show a significant improvement over open-loop control and represent an obvious target for further investigation. Experiments into the closed-loop control of ER fluid dampers have shown some of the advantages available (Sims et al, 1999).

8. CONCLUSIONS

In this paper the authors have described the design and construction of a novel vibration isolator which uses MR fluid as the working medium. Preliminary test results show that the transmissibility of the device can be controlled over a wide range through varying the voltage applied to the coil of the MR damper.

A simple quasi-steady mathematical model has been introduced to account for the observed behavior of the vibration isolator. Model predictions are encouraging but it has been emphasized that further development is required.

Based upon the model of the MR damper, numerical experiments were performed to examine the influence of applying a feedback control strategy. By switching the damper between two force levels, it was shown how significant improvements

could be achieved in the transmissibility characteristics. Current work is directed towards implementing this control strategy.

ACKNOWLEDGEMENTS

The authors would like to thank the US Army, European Research Office for support of this work under contract number N68171-98-M-5388. Thanks are also due to Dr Mark Jolly of Lord Corporation for the loan of the MR damper. One of the authors (NDS) was in receipt of an EPSRC studentship while the work was in progress.

REFERENCES

- Bender, E.K., 1968. "Optimum linear preview control with application to vehicle suspension" ASME Transactions, Journal of Basic Engineering, Vol. 90, pp213-221.
- El Wahed, A. K., Sproston, J. L., and Stanway, R., 1998. "The Performance of an ER Fluid in Dynamic Squeeze Flow under Constant Voltage and Constant Field," Journal of Physics D: Applied Physics, Vol. 31, pp2964-2974.
- El Wahed, A. K., Sproston, J. L., and Stanway, R., 1999. "The Performance of an ER Fluid in Dynamic Squeeze-flow: The Influence of Solid Phase Size," Journal of Colloid and Interface Science, Vol. 211, pp264-280.
- Jolly, M. R., and Carlson, J. D., 1996. "Controllable Squeeze-film Damping using MR Fluid," Proceedings of Actuator '96, Bremen, Germany, June 26-28, pp333-336.
- Jolly, M. R., Bender, J. W., and Carlson, J. D., 1998. "Properties and Applications of Commercial MR Fluids," Proceedings SPIE 5th Annual Symposium on Smart Structures and Materials, San Diego, CA.
- Karnopp, D.C., Crosby, M.J. and Harwood, R.A., 1974 "Vibration control using semi-active force generators" ASME Transactions, Journal of Engineering for Industry, Vol. 96, pp619-626.
- Sims N D, Stanway R, Peel D J, Bullough W A and Johnson A R 1999, "Controllable viscous damping: An experimental study of an electrorheological long-stroke damper under proportional feedback control" Smart Materials and Structures, Vol. 8, p. 601-615.
- Stanway, R., Sproston, J. L., Prendergast, M. J., Case, J. R., and Wilne, C. E., 1992. "ER Fluids in the Squeeze-flow Mode: An Application to Vibration Isolation," Journal of Electrostatics, Vol. 28, pp89-94.
- The Mathworks, 1997. "Using Simulink".
- Williams, E. W., Rigby, S. G., Sproston, J. L., and Stanway, R., 1993. "ER Fluids Applied to an Automotive Engine Mount," Journal of Non-Newtonian Fluid Mechanics, Vol. 47, pp221-238.

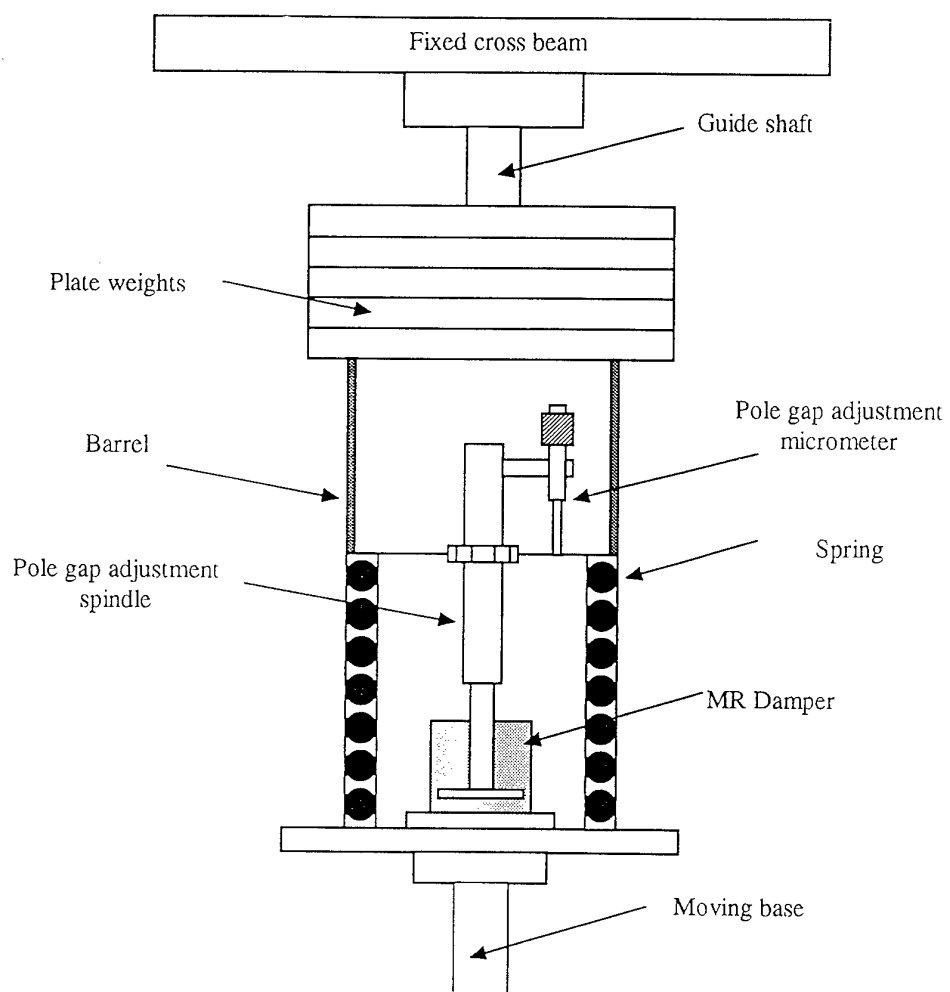


Figure 1 Schematic diagram of test facility.

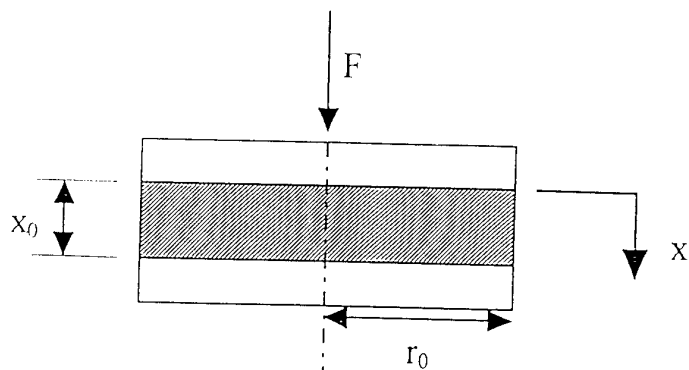


Figure 2 MR squeeze-flow cell.

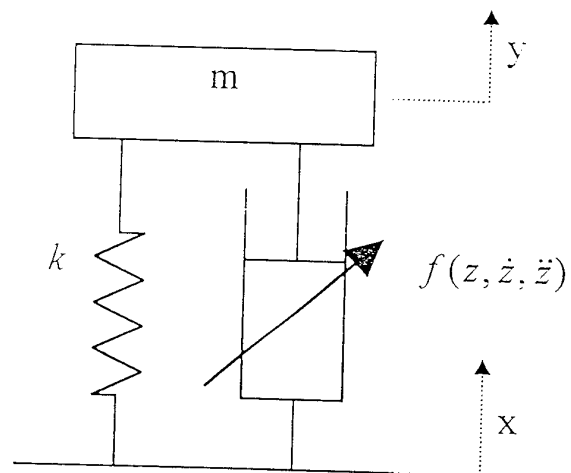


Figure 3 Vibration isolator: lumped parameter model.

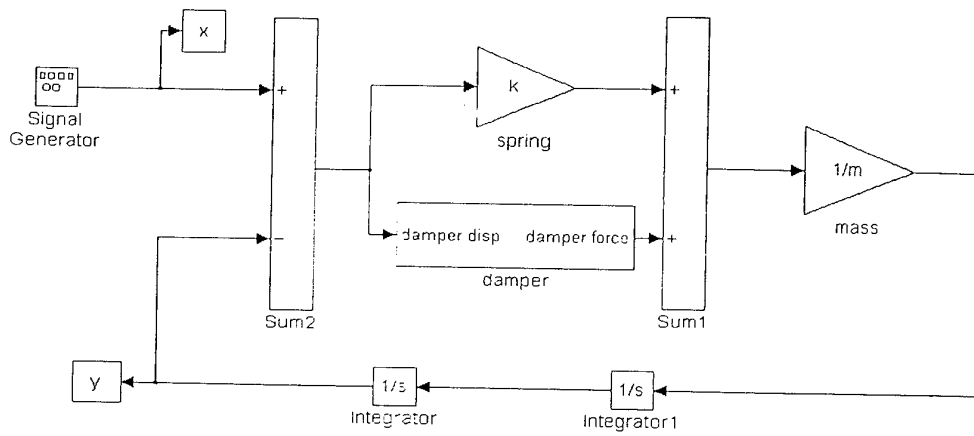


Figure 4 Block diagram model of vibration isolator.

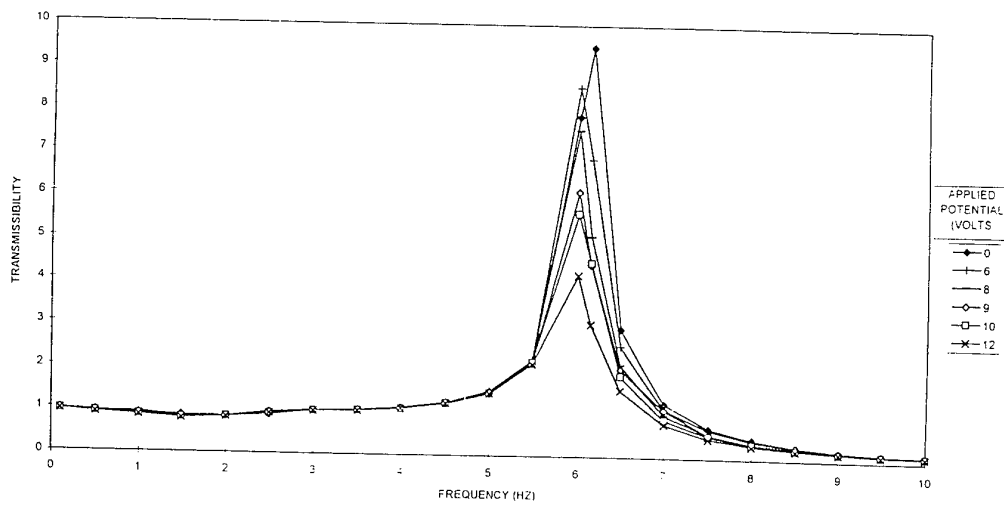


Figure 5 Transmissibility versus frequency: experimental results in the absence of MR fluid.

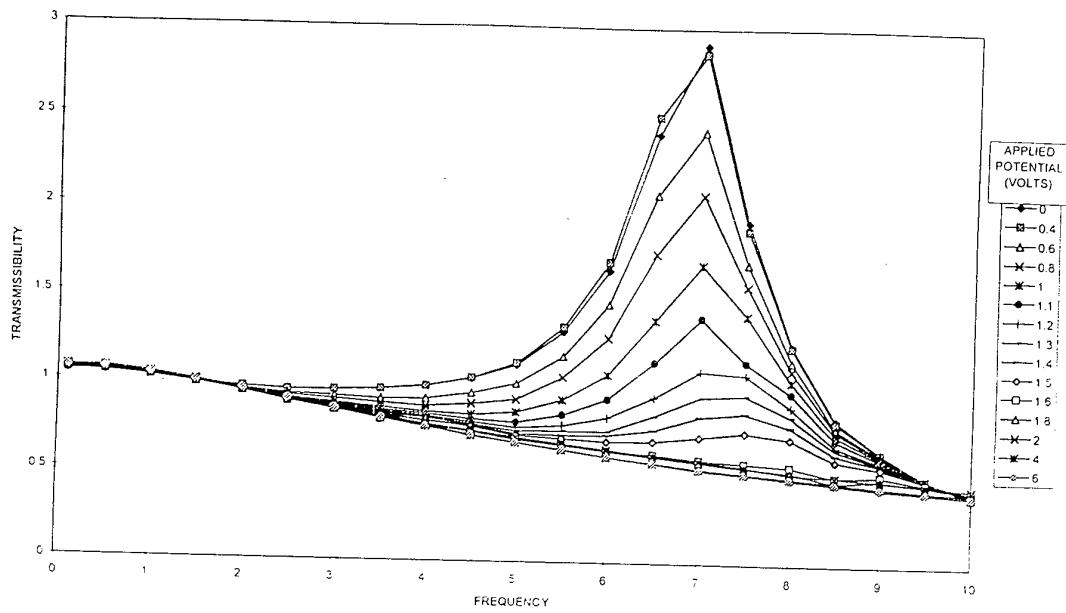


Figure 6 Transmissibility versus frequency: the influence of MR fluid.

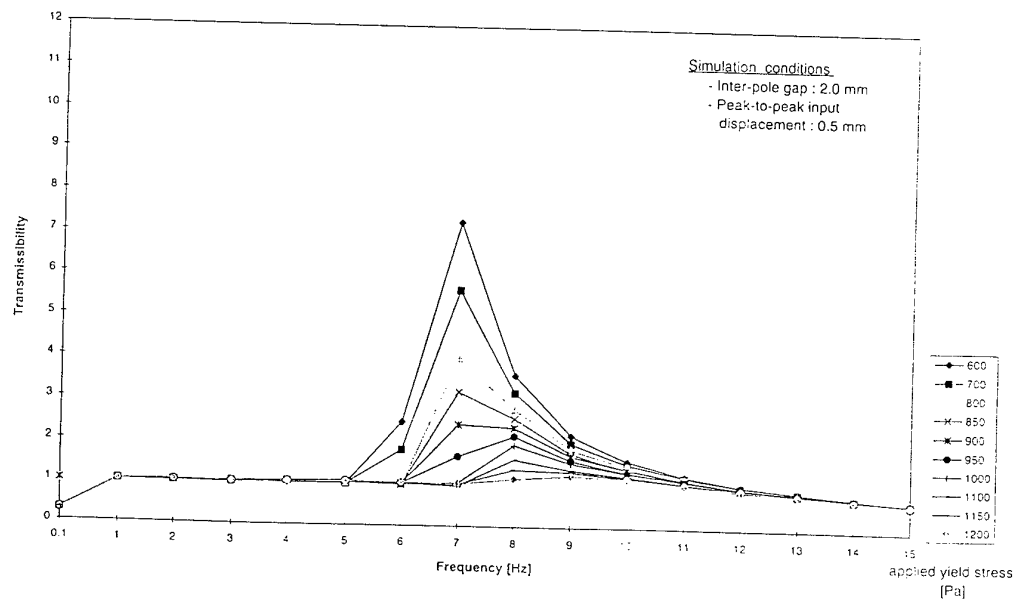


Figure 7 Model predictions of transmissibility versus frequency at various values of MR yield stress.

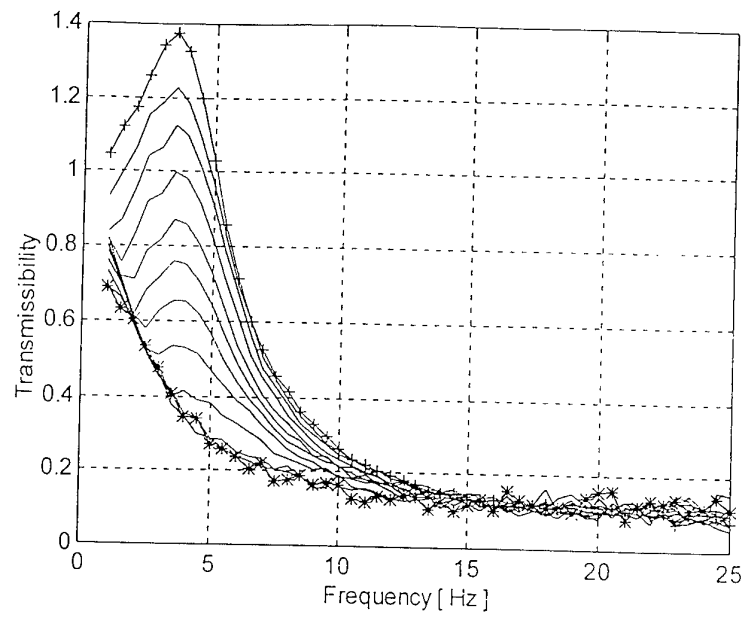


Figure 8 Feedback control: transmissibility versus frequency. Applied yield stress ranging from zero to 500 Pa.

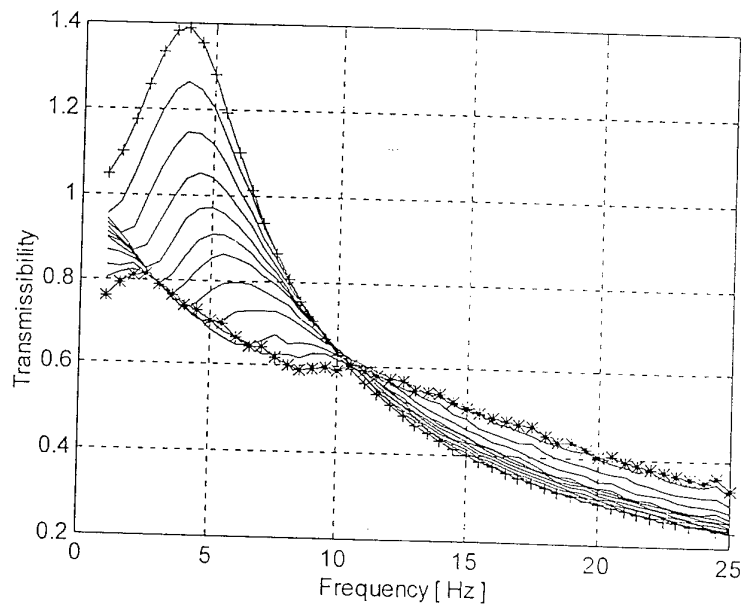
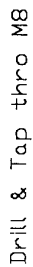


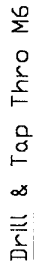
Figure 9 Feedback control: transmissibility versus frequency. Base viscosity of MR fluid included.

APPENDIX B

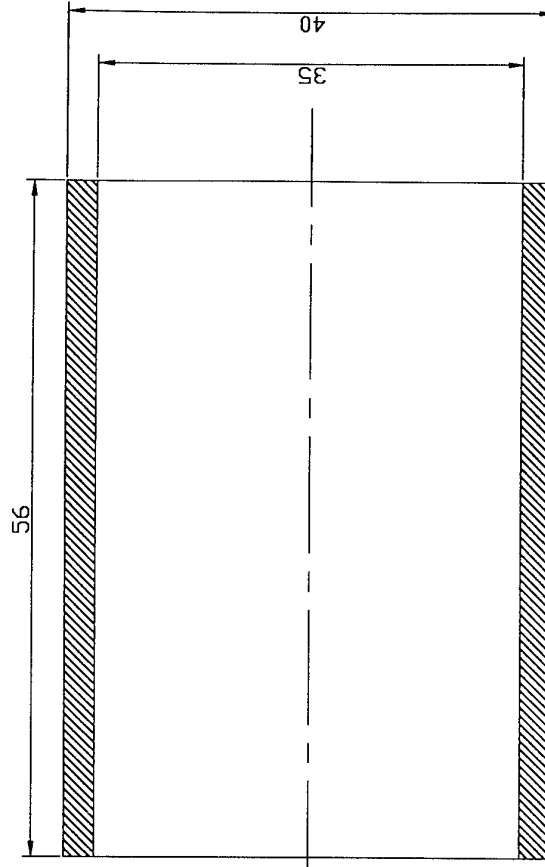
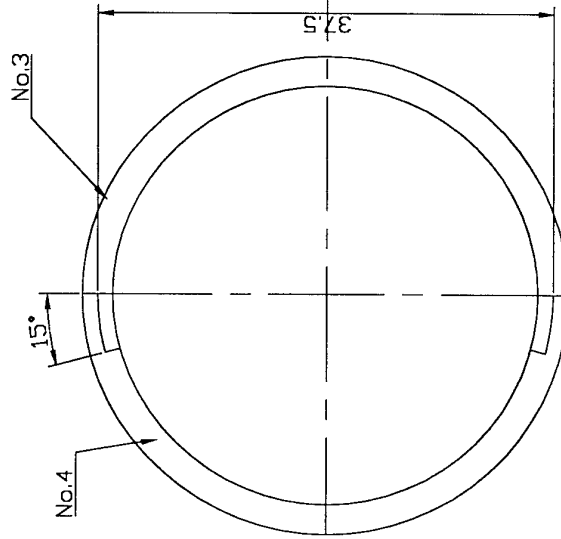
Double-acting MR squeeze-flow damper, set of detail drawings.



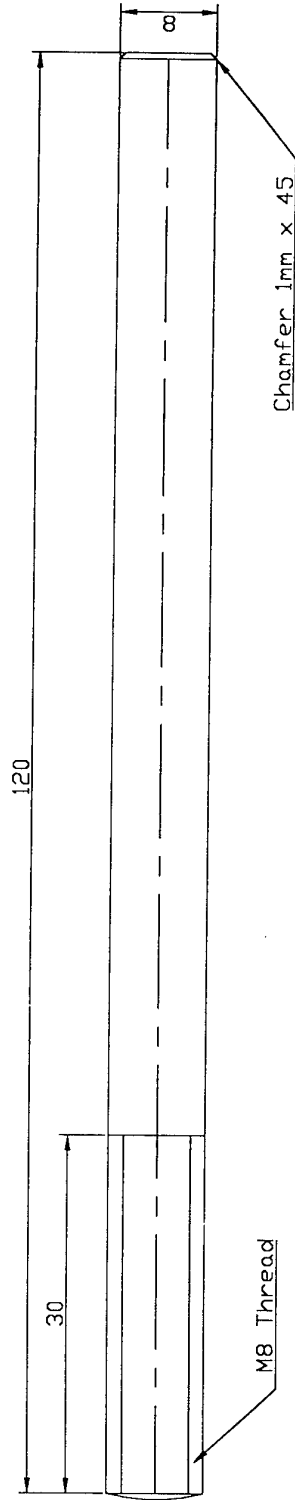
PART	Upper End Cap	PART No. 1	MATERIAL	Stainless 316L	DWG No.	101-01
DRAWN BY	Agodbehere	DATE	20/01/00	DRAWN 3rd ANGLE	SCALE	2:1
Tolerances to be +/- 0.1mm unless stated otherwise						



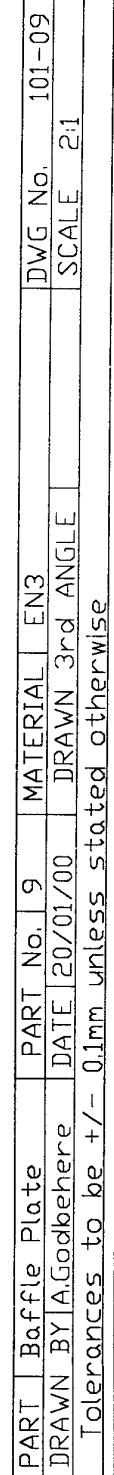
Tolerances to be +/- 0.1mm unless stated otherwise



PART Outer Casing Cover	PART No. 3&4	MATERIAL EN3	DWG No. 1J1-03/4
DRAWN BY A.Godbehere	DATE 20/01/00	DRAWN 3rd ANGLE	SCALE 2:1
Tolerances to be +/- 0.1mm unless stated otherwise			

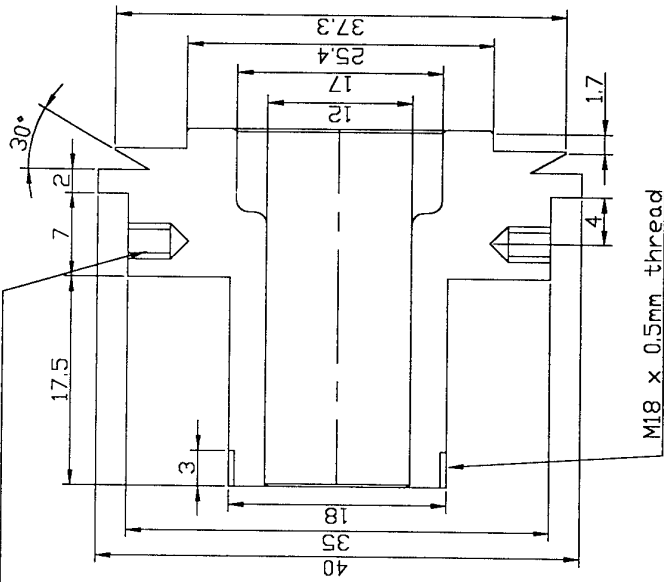


PART	Center Shaft	PART No.	8	MATERIAL	Stainless 316L	DWG No.	101-08
DRAWN BY	A.Godbehere	DATE	20/01/00	DRAWN 3rd	ANGLE	SCALE	2:1
Tolerances to be +/- 0.1mm unless stated otherwise							



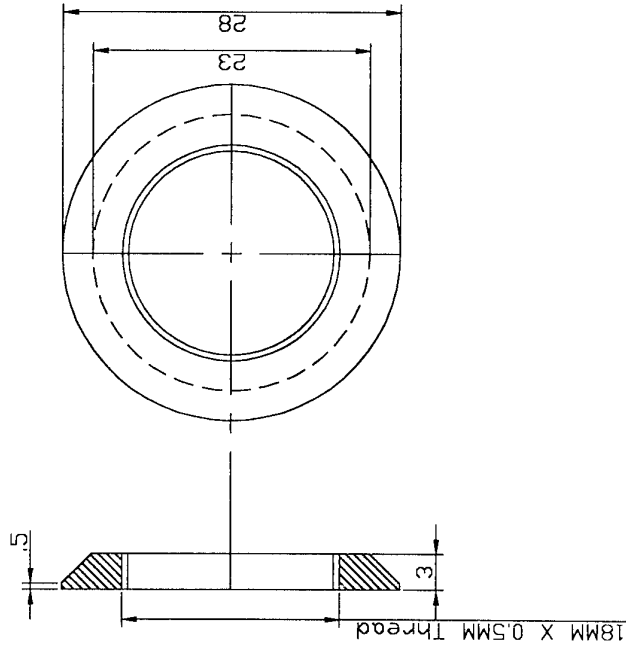
PART	Baffle Plate	PART No.	9	MATERIAL	EN3	DWG No.	101-09
DRAWN BY	A.Godbehere	DATE	20/01/00	DRAWN 3rd	ANGLE	SCALE	2:1
Tolerances to be +/- 0.1mm unless stated otherwise							

Drill & tap M3 x 5mm deep



M18 x 0.5mm thread

PART Upper&Lower Core	PART N61&12	MATERIAL EN3	DWG No. 101-11/12
DRAWN BY A.Godbehere	DATE 20/01/00	DRAWN 3rd ANGLE	SCALE 2:1
Tolerances to be +/- 0.1mm unless stated otherwise			



PART Locking Ring	PART No. 14	MATERIAL EN3	DWG No. 101-14
DRAWN BY A.Godbehere	DATE 20/01/00	DRAWN 3rd ANGLE	SCALE 2:1
Tolerances are to be +/- 0.1mm unless stated otherwise			

APPENDIX C

Copy of Sims, N. D., Stanway, R., Peel, D. J., Bullough, W. A. and Johnson, A. R., 1999. "Controllable viscous damping: an experimental study of an ER damper under proportional feedback control", Smart Materials and Structures, **8**, pp. 601-615.

Controllable viscous damping: an experimental study of an electrorheological long-stroke damper under proportional feedback control

N D Sims, R Stanway†, D J Peel, W A Bullough and A R Johnson

Department of Mechanical Engineering, The University of Sheffield, Mappin Street, Sheffield, S1 3JD, UK

Received 26 July 1999

Abstract. It is now well known that smart fluids (electrorheological (ER) and magnetorheological) can form the basis of controllable vibration damping devices. With both types of fluid, however, the force/velocity characteristic of the resulting damper is significantly nonlinear, possessing the general form associated with a Bingham plastic. In a previous paper the authors suggested that by using a linear feedback control strategy it should be possible to produce the equivalent of a viscous damper with a continuously variable damping coefficient. In the present paper the authors describe a comprehensive investigation into the implementation of this linearization strategy on an industrial scale ER long-stroke vibration damper. Using mechanical excitation frequencies up to 5 Hz it is shown that linear behaviour can be obtained between well defined limits and that the slope of the linearized force/velocity characteristic can be specified through the choice of a controller gain term.

1. Introduction

It is now well established that smart fluids, both electrorheological (ER) and magnetorheological (MR), provide the basis for the construction of controllable vibration damping devices (Sims *et al* 1999b). The construction and testing of controllable dampers using ER fluid as the working medium is described in various recent publications (Makris *et al* 1996, Gavin *et al* 1996a, b, Kamath *et al* 1996). Controllable dampers employing MR fluids are described by a number of authors (Dyke *et al* 1996, Kamath *et al* 1997, Jolly *et al* 1998). Potential areas of application that have been investigated include robotics (Choi *et al* 1995), the aerospace industries (Kamath *et al* 1997), and the seismic protection of tall buildings (Makris *et al* 1996).

There are key differences between ER and MR fluids which serve to explain why MR-based devices are now mass-produced for commercial applications whereas ER-based devices remain at the prototype stage. ER fluids are excited by an applied electric field of up to 8 kV mm^{-1} of inter-electrode gap. To produce such levels of field strength requires high voltage, a fact that deters many potential users who perceive safety problems. MR fluids on the other hand

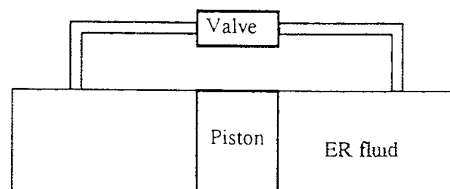


Figure 1. Schematic diagram of the piston and cylinder.

are excited by a magnetic field, which requires only a low-voltage source. In addition MR fluids generate significantly greater dynamic force levels than ER fluids and operate over much greater temperature ranges.

There is, however, one major feature shared by both ER and MR fluids—the general form of the force/velocity characteristic, which is significantly nonlinear. The application of an electric or magnetic field, as appropriate, causes the development of a yield stress within the smart fluid. The simplest model that can be used to account for the behaviour of a smart fluid is the well known Bingham plastic model, essentially a combination of Coulomb and viscous damping effects. In a previous paper (Sims *et al* 1997), it was suggested that the application of a relatively simple feedback control system to an ER damper should produce

† Author to whom correspondence should be addressed.

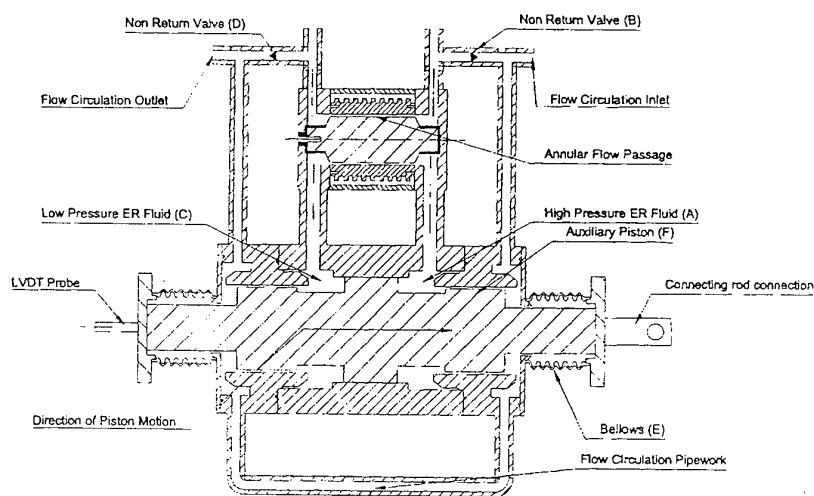


Figure 2. ER long-stroke vibration damper.

a device with a controllable viscous damping characteristic. Using a quasi-steady model of the ER vibration damper the development of the control scheme was described and it was shown how, in principle, linear behaviour was available between well defined limits. Also, it was shown how the slope of the linearized force/velocity characteristic could be varied through the choice of a controller gain term. If linearization can be demonstrated in practice then the prospect of controllable viscous dampers opens up for both ER- and MR-based devices.

In the following, the authors describe a comprehensive study into the implementation of feedback control of an ER vibration damper. The paper begins with a description of an industrial-scale, ER long-stroke damper which forms the basis of the study. Modelling of the damper is then summarized with emphasis on the extension of the basic quasi-steady model to account for dynamic effects within the ER fluid. A numerical simulation is used to choose the feedback control parameters and to design the various signal processing algorithms. Finally the results of implementing feedback control are presented and discussed.

2. Experimental arrangement

Before describing the modelling and control strategies, it is necessary to have an understanding of the ER long-stroke damper test facility that forms the basis of the present investigation. In this section, the test facility is described in detail, along with the associated measurement and control equipment.

The ER damper itself essentially consists of a piston being driven sinusoidally through a cylinder. An ER valve forms a flow bypass, as shown schematically in figure 1. The full experimental facility comprises the ER damper together with a piston drive mechanism, an ER fluid circulation system, a cooling water system and instrumentation and control equipment. These features are described in turn.

2.1. ER damper

The ER long-stroke damper consists of a piston and cylinder arrangement that is bypassed by an ER valve. The piston has an effective area of 0.0014 m^2 , and the maximum piston stroke is 16 mm. The fluid used in the device is commercially available (Bayer 'Rheobay' 3565), and consists of a silicone oil carrier liquid and polymer particle suspension. The manufacturer's maximum recommended electric field is 8 kV mm^{-1} , but during these tests the electric field was limited to 4 kV mm^{-1} . During operation, the fluid's behaviour can be explained with reference to figure 2. As the piston is displaced by the drive mechanism from the left to the right, the volume (A) decreases, forcing fluid at high pressure through the ER valve. Note that the non-return valve (B) remains closed during this operation. Meanwhile, the volume (C) increases, and the non-return valve (D) opens as fluid flows in to the expansion side of the cylinder. The expansion side of the cylinder is therefore pressurized to the reservoir pressure, which helps to avoid cavitation of the fluid. The ends of the device are sealed with a bellows arrangement. One end of each of the bellows is clamped and sealed to the cylinder end and the other end is clamped and sealed to the piston. The fluid volume within the bellows (E) is sealed from the high-pressure fluid (A) by the auxiliary piston (F). This ensures that the fluid pressure on the bellows is maintained at the reservoir pressure, thus extending the life of the bellows. Any nitrogen gas, or air, that has become trapped in the system can be removed by way of valves at the bleed points indicated on figure 2.

The ER valve, figure 3, is 70 mm long and consists of two concentric electrodes, one capable of being raised to a high voltage and the other earthed. Fluid flows through the 0.5 mm annular gap between the electrodes and the resistance to flow is altered by the electric field. This resistance to flow results in a pressure drop across the valve. Since the expansion side of the valve is maintained at the reservoir pressure, the pressure drop across the valve is manifested as a pressure increase in the compression side of the device. This results in a force

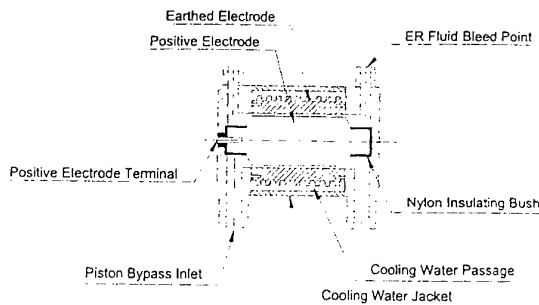


Figure 3. ER valve cross section.

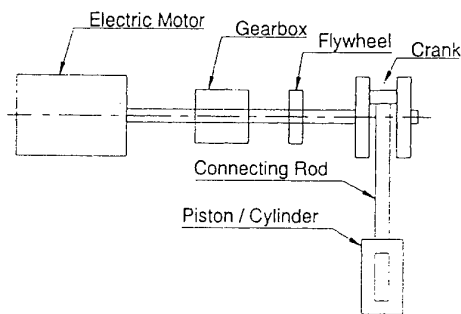


Figure 4. Crank arrangement for the driving piston.

acting on the piston, equal to the pressure difference between volumes A and C, multiplied by the effective piston area.

2.2. Piston drive mechanism

The piston is driven by a variable speed electric motor, via a variable ratio reduction gearbox, coupled to a flywheel and crank mechanism. This is shown schematically in figure 4. The gearbox has a maximum input speed of 1500 rpm, which is reduced to 150, 340, 700, or 1500 rpm depending on the selected gear. This enables the piston frequency to be set manually to any value up to 25 Hz. The crank arrangement is such that the connecting rod can be moved radially on the crank arm to adjust the displacement amplitude. The maximum displacement amplitude of 8 mm is governed by the piston and cylinder design, the displacement amplitude can only be adjusted off-line. The connecting rod is attached to one end of the piston, which translates inside the rigidly supported cylinder.

2.3. ER fluid circulation system

The ER fluid circulation system consists of a fluid reservoir, circulation pump, filter, isolation valves and the ER damper described in section 2.1. The system is shown schematically in figure 5. The ER fluid reservoir is pressurized by nitrogen to 0.7 bar g, referred to as the reservoir pressure. From the reservoir, the fluid can be circulated by a pump through the filter and piston/cylinder arrangement. The filter catches foreign particles that are either magnetic or larger than those in the polymer suspension. Constant circulation ensures that the fluid remains homogeneous in terms of the volume

Controllable viscous damping: ER long-stroke damper

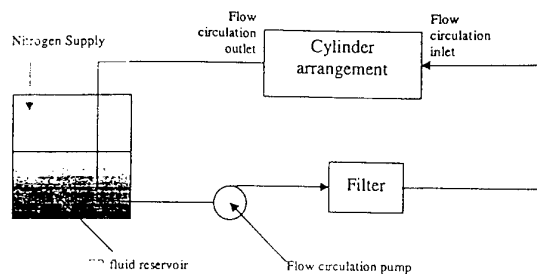


Figure 5. The ER fluid circulation system.

fraction of the particle suspension. This is important in the laboratory because changes in the volume fraction are likely to affect the yield stress of the fluid.

2.4. Water circulation system

Like any oil, ER fluid has characteristics that are highly dependent upon temperature, particularly its viscosity. During laboratory tests, it is therefore important to maintain accurate control of the fluid's temperature and here this is achieved by a water circulation system. The water circulation system consists of a water bath and circulation pump, as shown schematically in figure 6. The heating coil and thermostat in the heated tank ensure that the water temperature can be maintained at any specified value in the range 25–70 °C. From the heated tank the water is drawn by a pump to a cooling jacket on the ER valve. During operation the energy dissipated from the device increases the temperature of the fluid in the valve. The cooling jacket acts as a heat exchanger to ensure that the fluid temperature in the valve is maintained. From the cooling jacket, the cooling water flows to the ER reservoir water bath. This maintains the reservoir of ER fluid at the operating temperature. The water then returns to the heated tank. In summary, the water circulation system serves two purposes: heating the fluid to the desired operating temperature and removal of the dissipated heat energy from the system, thus maintaining the desired operating temperature of the ER fluid.

2.5. Instrumentation and control equipment

The test facility is equipped with comprehensive instrumentation which is illustrated schematically in figure 7.

The resistance to flow of the fluid is measured as a pressure drop across the main piston, using pressure sensors fitted to the cylinder on either side of the piston. With reference to figure 2, these sensors measure the pressures in regions (A) and (C). The pressure sensors have a linear range of 0–50 bar and are in turn connected to piezoresistive amplifiers, which give outputs within the range of 0–1 V. Amplification ('Fylde' UNI-AMP 351UA) is then applied to the signals in order to ensure good resolution after quantization by the data acquisition system.

The displacement of the piston is measured by a linear variable differential transformer (LVDT) transducer, attached to the left-hand end of the piston which protrudes from the bellows, as shown in figure 2. This transducer had an

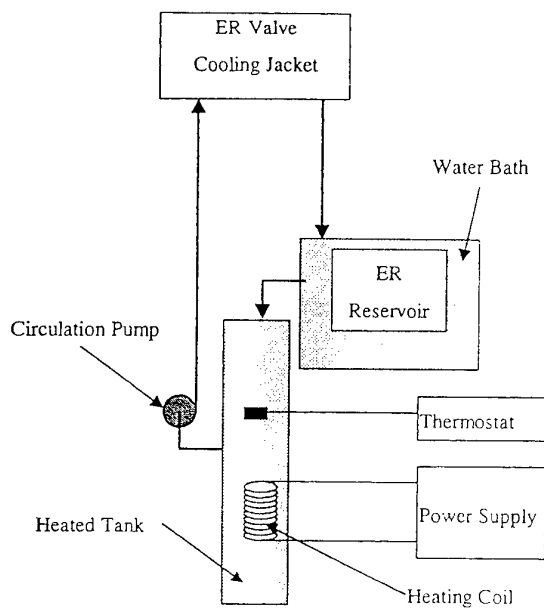


Figure 6. Damper test rig—water circulation system.

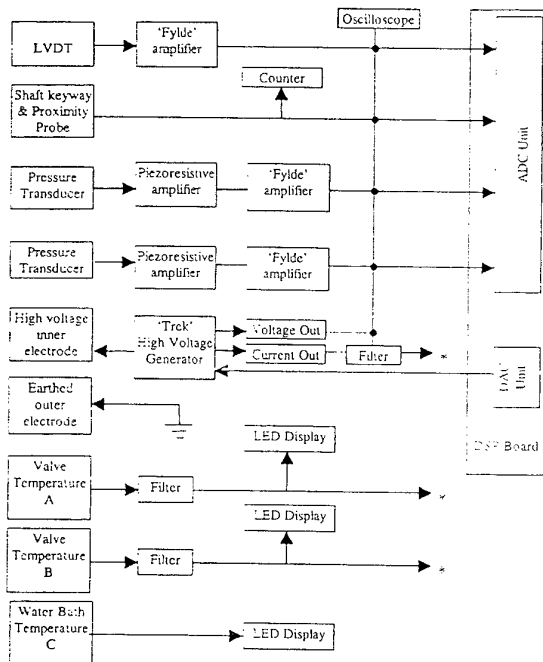


Figure 7. Measurement systems. The dSPACE controller board is interchangeable with an eight-channel data acquisition system, allowing data-logging for the signals marked*.

effective linear range of 100 mm with a gain of 0.01 V mm^{-1} . Again, an amplifier ('Fylde' UNI-AMP 351UA) ensures good quantized resolution. In addition to the LVDT, a key-way and proximity probe are fitted to the end of the crankshaft. This key-way is accurately matched to the

piston's bottom dead centre (BDC) position. The signal can therefore be used to evaluate the LVDT time constant (which may be important at higher displacement frequencies) to trigger the data acquisition and to measure the input displacement frequency.

Temperature sensors are fitted to the piston bypass on either side of the ER valve. These measure the temperature of the ER fluid both before and after it has passed through the valve. A third sensor measures the water temperature of the ER reservoir water bath. The signals are filtered using analogue low-pass elliptic filters ('Kemo' Type VBF/23) before being channelled to the data acquisition system.

The electric field across the electrodes of the ER valve is produced by a commercial high-voltage generator ('Trek' model P0575A). The remote input, 0–10 V, produces an output of 0–5 kV, corresponding to a field strength across the 0.5 mm electrode gap of 0–10 kV mm^{-1} . The unit has two additional outputs that provide measurement of voltage across and current through the ER fluid. The current signal is filtered using an analogue low-pass elliptic filter ('Kemo' Type VBF/24) prior to data acquisition.

The signals, once filtered or amplified as described above, can be logged by one of two methods. In addition to these two methods, a six-channel oscilloscope is connected so that the main signals (pressures, displacement, voltage, current, and crank BDC) can be viewed on-line. Meanwhile, the temperature readings are shown on LED display units.

In the first method, for data logging purposes, an eight-channel, 128 kWord analogue-digital converter (ADC) unit ('MicroLink' 4000 Series) is linked to a personal computer (PC). This is typically set to sample at 1 kHz, giving 16 s of data. In this case, the high-voltage generator remote input is supplied by a signal generator.

In the second method, for closed-loop control, digital signal processing (DSP) hardware can be used to control the electric field strength and acquire data. This system comprises a Pentium II 266 PC with a floating point DSP board ('dSPACE' DS1102), together with corresponding software. The DSP offers four ADC channels of 12 and 16 bit resolution, and four digital-analogue converter (DAC) channels (of which only one is used). The versatile software enables the user to generate and download DSP programs, either from hand-written C code or, more conveniently, directly from a block diagram model (Simulink 1999). Once the DSP program is running the program variables can be changed or viewed on-line, using either the DSP software or via Matlab using the DSP 'toolbox'.

3. Quasi-steady damper model

The ER valve used in the test facility was the subject of previous research, mainly using assumptions of quasi-steady flow (Peel *et al* 1996). Peel described the development of semi-empirical constitutive equations to account for the flow rate/pressure drop characteristics of the valve. For completeness, the derivation of these equations is briefly summarized below.

The modelling procedure is based upon the assumption that the flow through the ER valve, whose flow passage is annular, can be approximated by a model describing

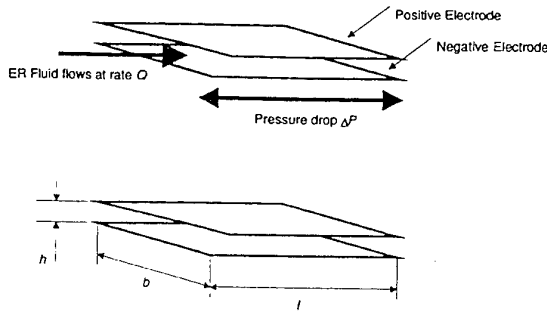


Figure 8. Bingham flow between flat plates.

Bingham plastic flow between two flat plates, where the yield stress is due to the electric field across the plates. This is shown schematically in figure 8. Given this assumption, the constitutive equation for a Bingham plastic flowing in steady state through parallel plates of separation h , breadth b , and length l is (Wilkinson 1960)

$$4 \left(\frac{l}{h \Delta P} \right)^3 \tau_b^3 - 3 \left(\frac{l}{h \Delta P} \right) \tau_b + \left(1 - \frac{12 \mu l Q}{b h^3 \Delta P} \right) = 0 \quad (1)$$

where τ_b is the Bingham plastic yield stress, ΔP is the pressure drop across the plates, Q is the fluid flow rate, and μ is the fluid viscosity. Of the three roots of this cubic equation, two are inadmissible, leaving the largest positive root as the only physically meaningful solution (Wilkinson 1960).

The post-yield behaviour of an ER fluid differs somewhat from that of an ideal Bingham plastic. This is due to a depletion in the resistance to flow in the fluid as flow rate increases. As the first step towards a robust modelling technique, the Bingham plastic equation is first expressed in non-dimensional form:

$$\pi_1^3 - \left(\frac{3}{2} + 6 \frac{\pi_2}{\pi_{3,0}} \right) \left(\frac{\pi_{3,0}}{\pi_2^2} \right) \pi_1^2 + \frac{1}{2} \left(\frac{\pi_{3,0}}{\pi_2^2} \right)^3 = 0 \quad (2)$$

where the non-dimensional groups are defined as

$$\pi_1 = \frac{\Delta P h}{2 l \rho \bar{u}^2} \quad (\text{Friction coefficient})$$

$$\pi_2 = \frac{\rho \bar{u} h}{\mu} \quad (\text{Reynolds number})$$

$$\pi_{3,0} = \frac{\tau_b \rho h^2}{\mu^2} \quad (\text{Bingham plastic Hedström number})$$

where ρ is the fluid density and the mean fluid flow velocity in the valve is $\bar{u} = Q/bh$.

The deviation of the ER fluid's behaviour from the Bingham plastic response can now be modelled by adjusting the Hedström number as the Reynolds number increases:

$$\pi_3 = P \times \pi_2 + \pi_{3,0} \quad (3)$$

Here π_3 is the ER Hedström number, P is an experimentally determined parameter and $\pi_{3,0}$ is the Bingham plastic Hedström number. This semi-empirical relationship, being non-dimensional, serves to characterize the ER fluid itself

rather than being dependent upon the valve geometry or prevailing flow conditions. Replacing $\pi_{3,0}$ with π_3 in (2) yields

$$\pi_1^3 - \left(\frac{3}{2} + 6 \frac{\pi_2}{\pi_3} \right) \left(\frac{\pi_3}{\pi_2^2} \right) \pi_1^2 + \frac{1}{2} \left(\frac{\pi_3}{\pi_2^2} \right)^3 = 0. \quad (4)$$

The next step is to develop a relationship between the yield stress τ_y and the electric field E across the electrodes. This empirical relationship has been developed from data obtained using a static clutch device (Peel *et al* 1996) as

$$\tau_y = A_{e2} E^2 + A_{e1} E + A_{e0} \quad (5)$$

where A_{e0} , A_{e1} and A_{e2} are experimentally determined constants.

The theory summarized above enables the pressure drop across the valve to be determined given the 'primary' variables—flow rate and field strength—the 'secondary' variables, consisting of the fluid properties ρ , μ , A_{e0} , A_{e1} and A_{e2} ; and valve geometry l , b and h . If the damper's response is simplified to that of the simple 'bypass' damper shown in figure 1, then the same pressure drop will occur across the piston, giving rise to a force F_d on the piston:

$$F_d = \Delta P a \quad (6)$$

where a is the effective piston area. The mean fluid velocity through the valve will be

$$\bar{u} = \frac{\dot{x} a}{b h} \quad (7)$$

where \dot{x} is the piston velocity. Finally the piston force can be expressed as

$$F_d = \chi(\dot{x}, E, \rho, \mu, A_{e2}, A_{e1}, A_{e0}, l, b, h, a). \quad (8)$$

The variables l , b , h and a are properties of the valve and piston geometry, and thus fixed. The variables ρ , μ , A_{e0} , A_{e1} and A_{e2} , however, are properties of the fluid that are likely to change under the influence of environmental conditions, especially temperature variations. In order to simplify the modelling procedure, these variables are assumed to be constant during a particular experiment, allowing us to rewrite (8) as

$$F_d = \chi(\dot{x}, E). \quad (9)$$

Note that numerical values of ρ , μ , A_{e0} , A_{e1} , A_{e2} , l , b , h and a are given in the appendix. The function χ is defined as the quasi-steady damper function and is shown graphically in figure 9.

This model of the damper's response has been used to illustrate the proposed control strategy (Sims *et al* 1997). As stated earlier, the main aim of the present investigation is to implement a control strategy on the ER test facility in order to linearize the damper's response. This control strategy consists of a proportional feedback control system, where the damper force is the controlled output and electric field strength in the ER valve is the manipulated variable. The control strategy is shown in block diagram form in figure 10(a). It has been demonstrated (West 1960) that for such a system, by appropriate choices of the forward-loop

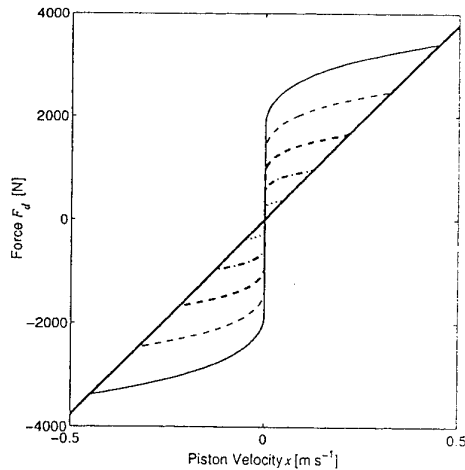


Figure 9. Quasi-steady damper function. —, $E = 0 \text{ kV mm}^{-1}$; \cdots , $E = 1 \text{ kV mm}^{-1}$; $-\cdot-$, $E = 2 \text{ kV mm}^{-1}$; $---$, $E = 3 \text{ kV mm}^{-1}$; $----$, $E = 4 \text{ kV mm}^{-1}$; $=====$, $E = 5 \text{ kV mm}^{-1}$.

gain G and feedback-loop gain B it is possible to generate a damper force that is independent of piston velocity. This is shown for the quasi-steady damper model in figure 10(b). Furthermore, by modifying the block diagram, as shown in figure 11(a), so that the set point is proportional to the velocity across the damper, a close approximation to linear damping can be achieved. The corresponding response is illustrated in figure 11(b). It can be seen that linear, variable damping has been achieved, within the control limits. The damping coefficient is proportional to the controller gain D and the control limits are the maximum and zero electric field strength conditions.

The earlier feasibility study (Sims *et al* 1997) demonstrated the feasibility of the proposed control strategy, but was subject to the following limitations:

- the damper model was quasi-steady,
- the influence of negative piston velocity on the controller was neglected,
- the various signal processing operations required for control were not modelled and
- the investigation was purely theoretical and numerical.

In the following these problems are overcome in turn. Firstly, an improved model of the damper is presented, along with experimental validation. Next, this model is incorporated into a comprehensive simulation of the closed-loop system. This simulation is used to determine the most appropriate values for the controller parameters and to design suitable signal processing algorithms.

4. Accounting for dynamic effects

The quasi-steady model summarized above is able to account for observed behaviour at low frequencies, say less than 1 Hz. At higher frequencies the influence of the ER fluid dynamics becomes significant and needs to be accounted for in the model. The main dynamic effects that occur in the device have been identified as arising from the fluid's

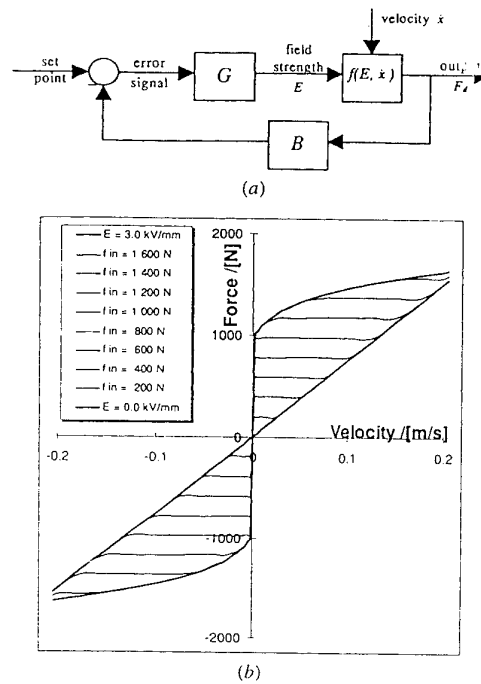


Figure 10. Initial control strategy. (a) Block diagram and (b) simulated force/velocity response.

compressibility and inertia, so in this section the damper model is extended so as to include these effects. A detailed description of the extension of the quasi-steady model, together with experimental validation, appears in an earlier paper (Sims *et al* 1999a). This work is summarized below.

We begin by considering the simplified physical arrangement of the ER long-stroke damper, as shown in figure 1. Whilst the resistance to flow that occurs in the valve is well described by the quasi-steady damper function χ , described earlier, it is the fluid's compressibility and inertia that are the main contributors toward dynamic effects. The fluid's compressibility can be expressed as a spring of stiffness k , running from the piston head to the valve, and the fluid's inertia can be represented as a mass m lumped at the piston head. To develop a lumped parameter model, the continuous nature of the fluid's flow can be overcome by 'unravelling' the device at the valve. This results in the system shown in figure 12. Tentative values for the stiffness k and mass m can be estimated from the fluid's bulk modulus and density, respectively, and are included in the appendix. Note, however, that these tentative values need to be updated using experimental data if the model is to account for observed behaviour.

This model does not correspond to the physical arrangement described in section 2.3. To recap, pressure in the expansion side of the piston and valve is relieved by a non-return valve, to the reservoir pressure, and hence does not resist flow. This aspect of the mechanical design can be incorporated into the model by using dampers that do not resist expansion. This is shown in figure 13, where the layout has been rearranged. With reference to figure 13 it is possible to identify three distinct operating regions.

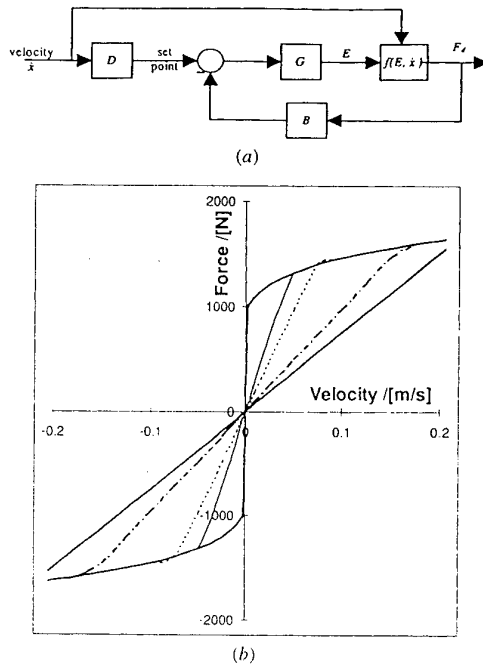


Figure 11. Initial control strategy, using a set point proportional to velocity. (a) Block diagram and (b) simulated force/velocity response. —, $E = 4.0 \text{ kV mm}^{-1}$; —, $D = 30\,000 \text{ N s m}^{-1}$; ·····, $D = 20\,000 \text{ N s m}^{-1}$; — — —, $D = 10\,000 \text{ N s m}^{-1}$; —, $E = 0.0 \text{ kV mm}^{-1}$.

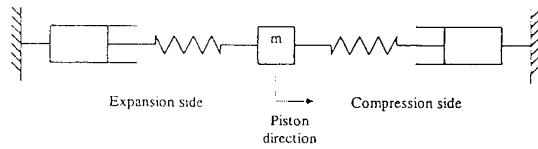


Figure 12. Lumped parameter representation.

Region 1. Here the damper velocity is positive, damper B is resisting motion while damper A and spring A are both transmitting zero force.

Region 2. Here the dampers come to a stop, both dampers become rigid and both springs resist motion.

Region 3. Once flow has reversed, damper A resists motion, while damper B and spring B both transmit zero force.

From these observations, it is logical to combine the two springs to form one bilinear spring, and to combine the dampers in a similar fashion. This is shown in figure 14. The stiffness of the spring during flow reversal is double that during flow, and so the resulting bilinear spring function is

$$F_s = \kappa(y, E) = \begin{cases} 2ky & \text{if } |y| \leq F_y/2k \\ ky - F_y/2 & \text{if } y < -F_y/2k \\ ky + F_y/2 & \text{if } y > F_y/2k \end{cases} \quad (10)$$

where y is the applied displacement across the spring, $x_2 - x_1$, and F_y is the resulting spring force. F_y is determined from the shear stress at yield τ_y , which can be obtained from (5):

$$F_y = \tau_y \times 2al/h = (A_{e2}E^2 + A_{e1}E + A_{e0}) \times 2al/h.$$

Controllable viscous damping: ER long-stroke damper

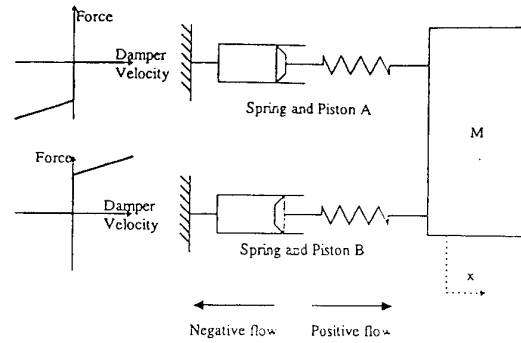


Figure 13. Lumped parameter system, rearranged with dampers that do not resist expansion.

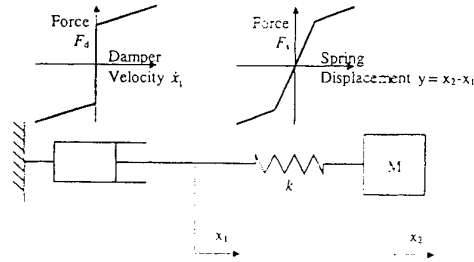


Figure 14. Simplified lumped parameter model.

The damper's response is given by the quasi-steady damper function defined in (9). The equations of motion for the system shown in figure 14 are therefore

$$\begin{aligned} -\chi(\dot{x}_1, E) + \kappa(x_2 - x_1, E) &= 0 \\ F - \kappa(x_2 - x_1, E) &= m\ddot{x}_2 \end{aligned} \quad (11)$$

where \ddot{x}_2 is the piston acceleration.

4.1. Solving the equations of motion

The system shown in figure 14 appears to be relatively simple since it possesses only two degrees of freedom. However, there are problems associated with its solution. First, the lack of an inertia term between the mass and spring makes the equations of motion statically degenerate, so they cannot be mapped onto the state-space in the traditional way. Second, the discontinuous nature of the quasi-steady damper function, shown graphically in figure 9, makes the equations difficult to solve. This is particularly the case if they are written in such a way that they involve an algebraic loop (The Mathworks 1997), that is $x = f(x)$, since then an iterative method must be employed, and this must be robust in the face of a step discontinuity.

An elegant solution to these problems has been developed (Sims *et al* 1999a) which involves rewriting the equations of motion (11) in the form

$$\dot{x}_1 = \chi^{-1}(\kappa(x_2 - x_1, E), E) \quad (12a)$$

$$F = \kappa(x_2 - x_1, E) + m\ddot{x}_2 \quad (12b)$$

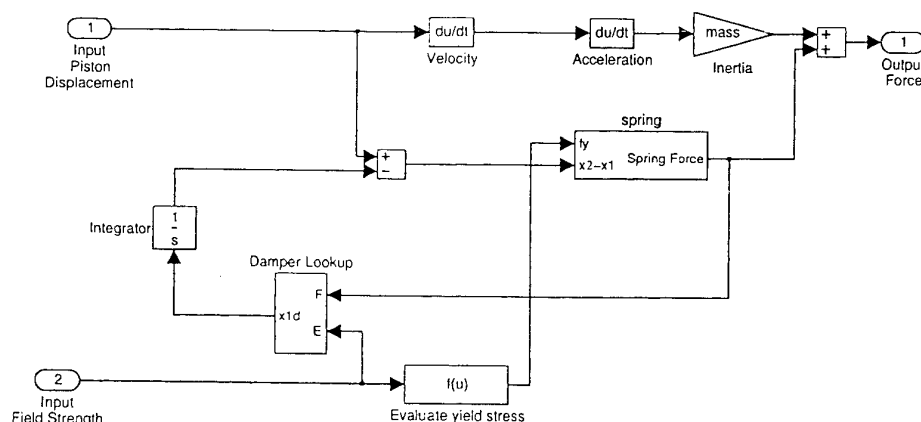


Figure 15. Block diagram for the equations of motion.

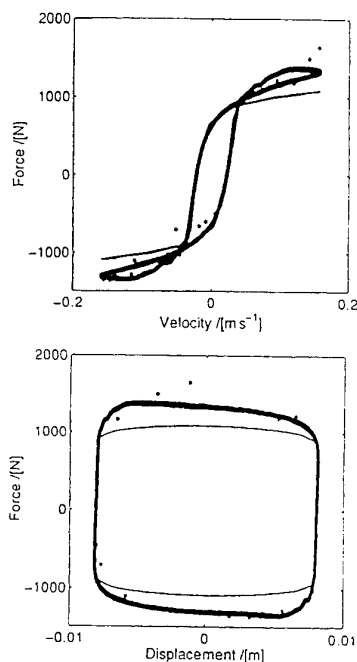


Figure 16. Validated model and experimental results (open-loop). (a) Force against velocity and (b) force against displacement., experimental: —, predicted.

It can be seen that (12a) is an ordinary differential equation (ODE), involving the inverse quasi-steady damper function, rather than an algebraic equation with an algebraic loop. This avoids the use of iterative methods in solving and thus traditional ODE solvers can be used instead. Equation (12b) is readily solved, once x_1 is determined from (12a). However, we still require the inverse of the quasi-steady damper function

$$\dot{x}_1 = \chi^{-1}(F_d, E). \quad (13)$$

This can be determined by any one of a number of iterative methods, but it was found that the most convenient technique

was the use of look-up tables. The process is started by generating force data at certain velocities for a given electric field strength. Provided these forces are monotonic and increasing, the data can be used to find the velocity at equally spaced force increments, using one-dimensional linear interpolation. This process is then repeated for different field strengths, resulting in a table of velocity data for given forces and field strengths. The advantage of this technique is that during simulation the inverse quasi-steady damper function does not have to be evaluated at each time step—the velocity is simply read from the look-up table. This allows the simulations to run significantly faster, since the computations required are much simpler. The errors associated with the technique will be negligible provided that the initial force data points are sufficiently close together.

Equation (12) can now be expressed in block diagram form as shown in figure 15. This block diagram can then be solved using modern simulation software (Simulink 1999). It was found that fixed step ODE solvers, such as fourth-order Runge-Kutta, performed best, using approximately 1000 steps per displacement cycle.

4.2. Experimental validation

Before the new model can be used to investigate the control strategy in greater depth, its predictions must be validated against experimental results. An extensive validation procedure has already been documented (Sims *et al* 1999a), to which the interested reader is referred. To summarize this work, it was found that the model accurately predicted the response of the test rig once certain parameters were updated in line with observed behaviour. Initially, the model's stiffness term was based upon the manufacturer's value for the bulk modulus of the fluid, but it was found that the observed stiffness was less than half of this value. Similar discrepancies were found with the fluid viscosity value and the yield stress/electrical field relationship. Once these parameters were updated in line with observed behaviour, there was good agreement between the model and experimental results, as shown in figure 16.

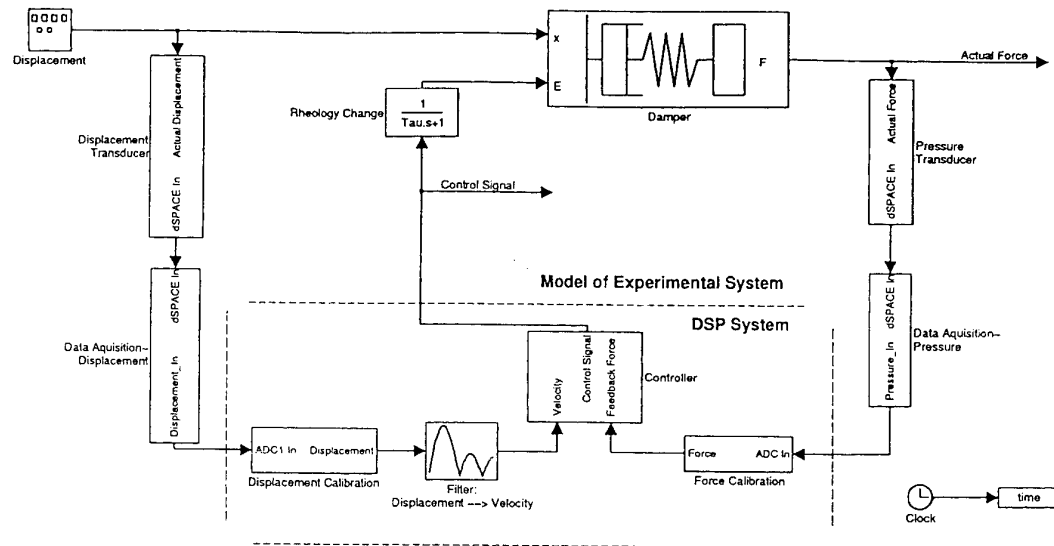


Figure 17. Advanced closed-loop model—main system.

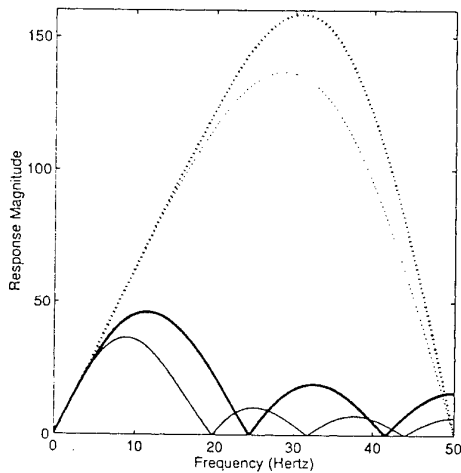


Figure 18. Frequency response magnitude for differentiating filters at a sampling frequency of 100 Hz. —, FIRs order 7; ---, FIRs order 5; ·····, Stirling order 6; - · - · -, Stirling order 4.

5. Modelling the closed-loop response

Now that a more accurate model of the ER long-stroke damper has been developed, we are in a position to investigate the simulated closed-loop response in greater depth. The aim of this section is to develop a controller that can be physically implemented on the test rig. This will require:

- the design of a controller that will operate during negative piston velocity,
- the development of a technique to perform numerical differentiation of the measured displacement signal, to provide a record of the piston velocity and
- a numerical investigation of the simulated closed-loop response to indicate suitable values for the controller gains.

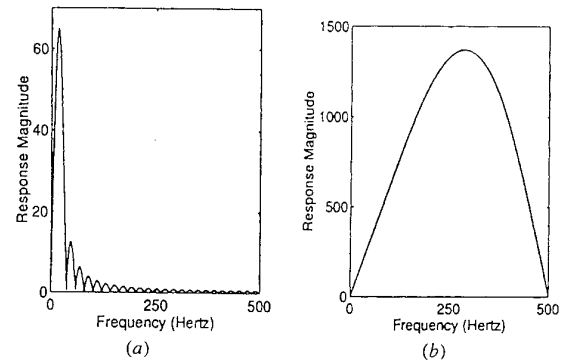


Figure 19. Frequency response magnitude for differentiating filters at a sampling frequency of 1000 Hz. (a) FIRs order 50 and (b) Stirling order eight.

5.1. Development of a closed-loop model

The closed-loop model described here uses the same control strategy as the feasibility study (Sims *et al* 1997), but incorporates a number of improvements so as to produce a more accurate representation of the experimental facility. The model was designed using block diagram notation (Simulink 1999), whereby a system is built up from a number of sub-systems. The main system is shown in figure 17. The input to the system is the sinusoidal piston displacement. This constitutes one of the damper's inputs, the other being the electric field strength that is generated by the controller and high-voltage amplifier. The 'damper' sub-system is identical to that described in section 4.1 and illustrated in figure 15. The model accounts for the effects of the measurement and data acquisition processes by modelling signal noise, quantization, sampling, scaling, and saturation of the signal, before the signals are passed to the DSP system blocks. The first task of the DSP system is to convert the signals into piston force (Newtons) and

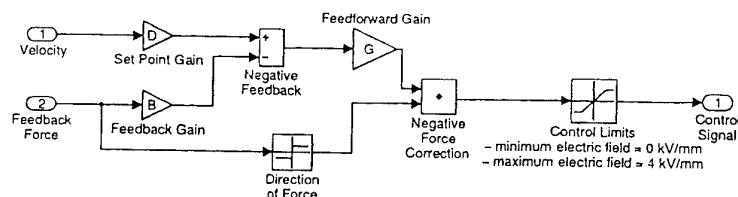
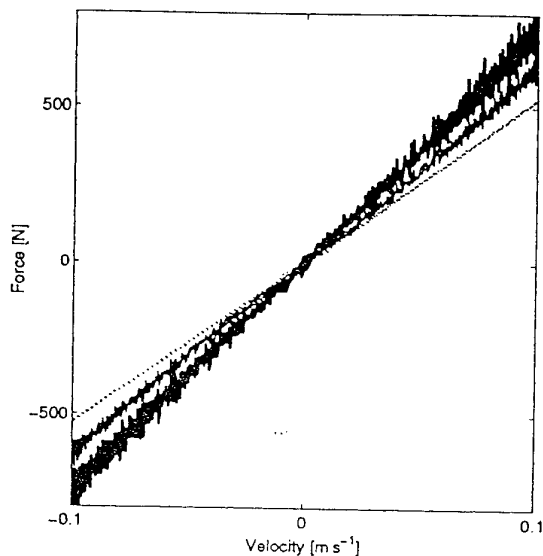
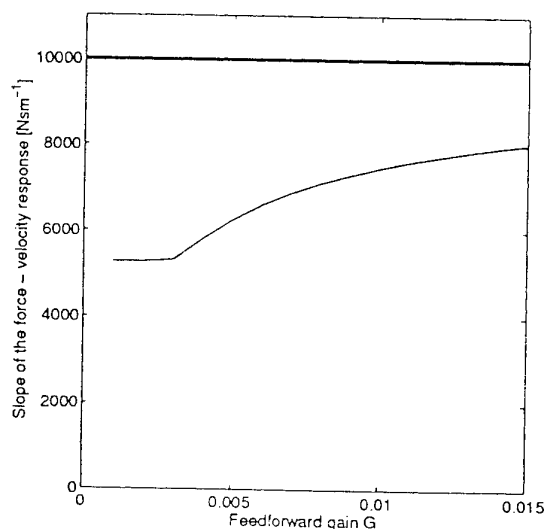


Figure 20. Controller sub-system.

Figure 21. Influence of G on the force against velocity response., $G = 0.001$; —, $G = 0.005$; — —, $G = 0.01$.Figure 22. Influence of G on the slope of the force against velocity response. —, simulated response; — —, set point gain D .

displacement (metres). The piston velocity must then be calculated from the displacement signal—in the feasibility study the displacement signal was simply differentiated, but realistically this signal must be assumed to be contaminated

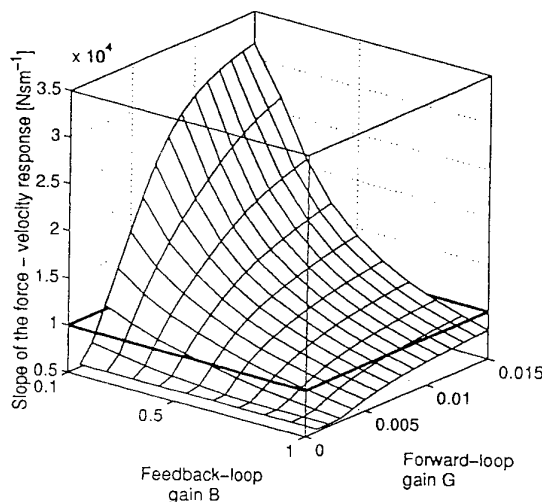


Figure 23. Influence of the forward-loop and feedback-loop gains on the slope of the force against velocity response.

by noise and so an alternative technique is now required. One suitable method is to design a discrete-time filter that operates as an approximate differentiator of the displacement signal. Two alternative filter designs are investigated, one based on the Stirling method (Scarborough 1958), and one using the Matlab filter design function *firls* (Matlab 1999), which designs a finite impulse response filter using a least-squares methodology. Ideally, the discrete filter should exhibit the following characteristics:

- accurate differentiation of the signal at frequencies below 20 Hz.
- effective filtering of high-frequency noise (> 20 Hz) and
- be of the lowest possible order to reduce the delay introduced by the filter.

Since differentiation is equivalent to multiplication by $i\omega$ in the frequency domain, one way of illustrating a filter's response is by looking at the magnitude of its frequency response. This is shown in figure 18 for Stirling filters of order four and six and *firls* filters of order five and seven, with a sampling frequency of 100 Hz. It can be seen that the *firls* filters are more effective at filtering out high-frequency noise, and that this performance improves with filter order. Conversely, with the Stirling method the amplification of noise increases with the order of the filter. The Stirling method would, however, give acceptable results if the sampling frequency were around 50 Hz, since accurate differentiation would then occur for frequencies up to 10 Hz. However, if the sampling frequency was much higher, say

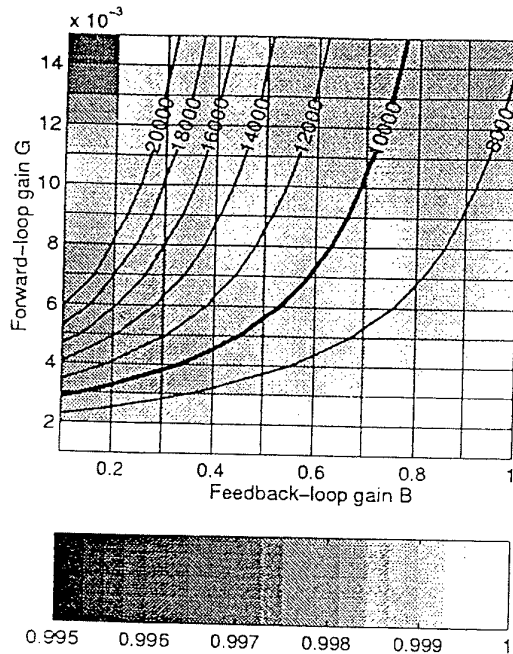


Figure 24. Contour plot showing the slope of the simulated force/velocity response. The shading indicates the correlation coefficient between the data and its line of best fit.

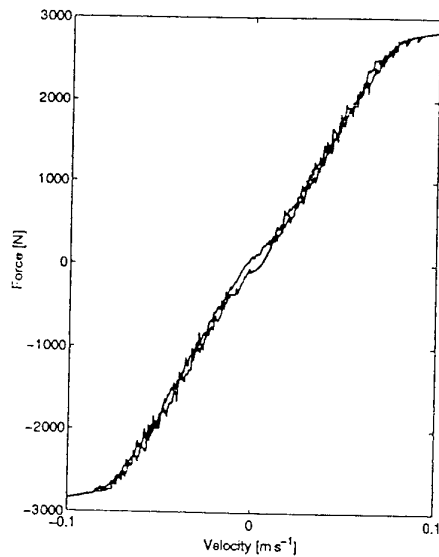


Figure 25. Saturation in the simulated force against velocity characteristic.

1 kHz, then the Stirling method would not produce acceptable results, amplifying the noise at frequencies up to 250 kHz. On the other hand, a 50th order fir filter could be used, with an acceptable delay, and the frequency response would be far superior. This is shown in figure 19. From this figure, it seems appropriate to choose a filter designed by the fir filter function, with the filter order chosen to suit the sampling frequency of the controller.

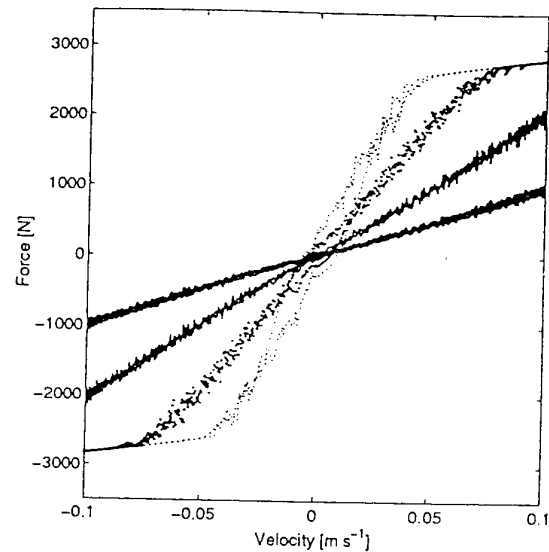


Figure 26. Simulated response with different set point gains. —, $D = 10 \text{ kN s m}^{-1}$; ---, $D = 20 \text{ kN s m}^{-1}$; ····, $D = 40 \text{ kN s m}^{-1}$; - · - ·, $D = 80 \text{ kN s m}^{-1}$.

Following differentiation, the calculated velocity and force signals are then passed to the controller sub-system which is shown in detail in figure 20. It can be seen that the basic structure of this controller resembles that used in the feasibility study (Sims *et al* 1997), and included in the present paper as figure 11(a). However, the controller has been modified so that it performs correctly when the set point and measured force are negative. When these conditions are present, the control signal must still be positive, since the field strength must always be positive. This is achieved by multiplying the control signal by -1 when the measured piston force is negative. The controller also has built-in control limits, corresponding to the maximum and minimum electric field strengths for the fluid.

The final process that requires modelling is that of the dynamics of the ER damper in response to a change in field strength. Open-loop tests which involved switching of the field strength and measurement of the corresponding force response, have shown that a time constant of 3 ms is associated with this operation (Sims *et al* 1999a). This time constant is incorporated into the model of the system with the 'Rheology change' first-order lag block, as shown in figure 17. The output from this block which represents electric field strength is then passed to the 'Damper' sub-system.

5.2. Simulated closed-loop response

The block diagram shown in figure 17 can now be solved using the Simulink software. The variables to be specified in the model are as follows:

- the forward-loop gain G ,
- the feedback-loop gain B ,
- the set point gain D and
- the DSP sampling frequency.

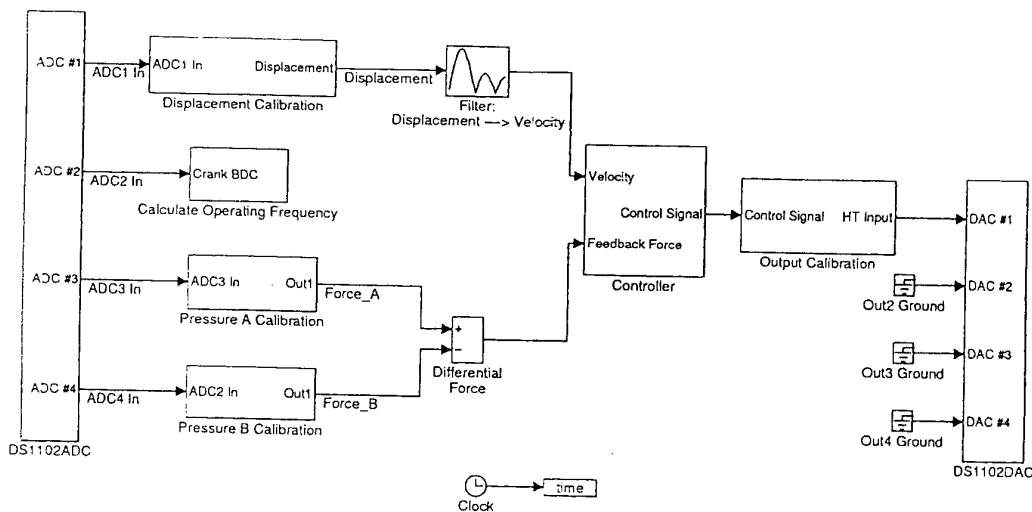


Figure 27. Block diagram to implement the control strategy on the dSPACE software.

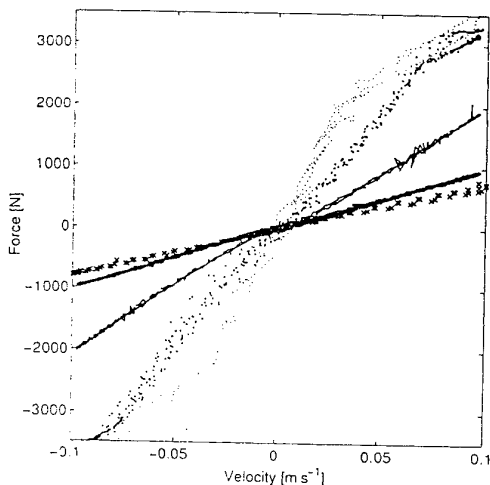


Figure 28. Experimental response with different set point gain. —•—, $D = 10 \text{ kN s m}^{-1}$; —■—, $D = 20 \text{ kN s m}^{-1}$;△....., $D = 40 \text{ kN s m}^{-1}$;×....., $D = 80 \text{ kN s m}^{-1}$; × × ×, zero electric field.

Other variables, such as displacement amplitude and frequency were held constant to simplify the investigation. Their values are tabulated in the appendix. Attention here is focussed on the force/velocity characteristic of the ER damper. In the feasibility study (Sims *et al* 1997), it was shown that as the forward-loop gain was increased, the force/velocity characteristic became linear, with a slope defined by the set point gain D . A sensible starting point with the extended model is to re-investigate this result. We begin by setting $D = 10 \text{ kN s m}^{-1}$, $B = 1$ (dimensionless), a DSP sampling frequency of 10 kHz, and investigating the influence of G on the force/velocity response. The result is shown in figure 21. In figure 22 the slope of each of the force velocity responses is plotted. It can be seen that the result is similar to that found in the feasibility study: as G is increased, the slope tends toward the set point gain D . However, for the highest

value of forward-loop gain, the measured force becomes noisy and the force velocity characteristic is scattered about its line of best fit. It was found that this phenomenon occurred more readily as the sampling frequency was reduced.

This response apparently limits our ability to achieve the desired damping coefficient, at unity feedback-loop gain. The next step then, is to investigate how the response varies when the feedback-loop gain is changed. By choosing 10 values of feedback-loop gain and 15 values of forward-loop gain, a total of 150 permutations result. The response can be simulated at each of these permutations and the slope of the force/velocity characteristic measured, to give a surface representing this slope against values of forward-loop and feedback-loop gains. This is shown in figure 23. It can be seen that the feedback-loop gain has the opposite effect to the forward-loop gain, and so there is a loci of values of B and G where the damping coefficient (i.e. the slope) equals the set point gain D . The loci of points is best illustrated by redrawing the B - G -slope data as a contour plot, as shown in figure 24. This figure contains more information about the force/velocity response at each permutation. The correlation coefficients between the force/velocity data, and its line of best fit, are plotted as a shaded map. Dark regions correspond to poor correlation, i.e. a nonlinear response. This nonlinearity is either due to the noisy response described above, or saturation at the device's control limits. For an example of the former, it is apparent that the characteristic plotted in figure 22 for $G = 0.01$ has a poor correlation with its straight line of best fit. For an example of the latter, figure 25 shows the response at $B = 0.1$ and $G = 0.015$. The maximum field strength has been reached and so the response has become nonlinear at high velocities.

Using the data shown in figure 24, it is possible to determine the most favourable values of the two gains. The objectives are to achieve a response with damping coefficient equal to D , and with the most linear response, i.e. highest correlation coefficient. Suitable values appear to be $B = 0.6$ and $G = 0.007$. In figure 26, the corresponding response is plotted at various set point gains. Figure 26 shows that linear variable damping has been achieved and the damping coefficient

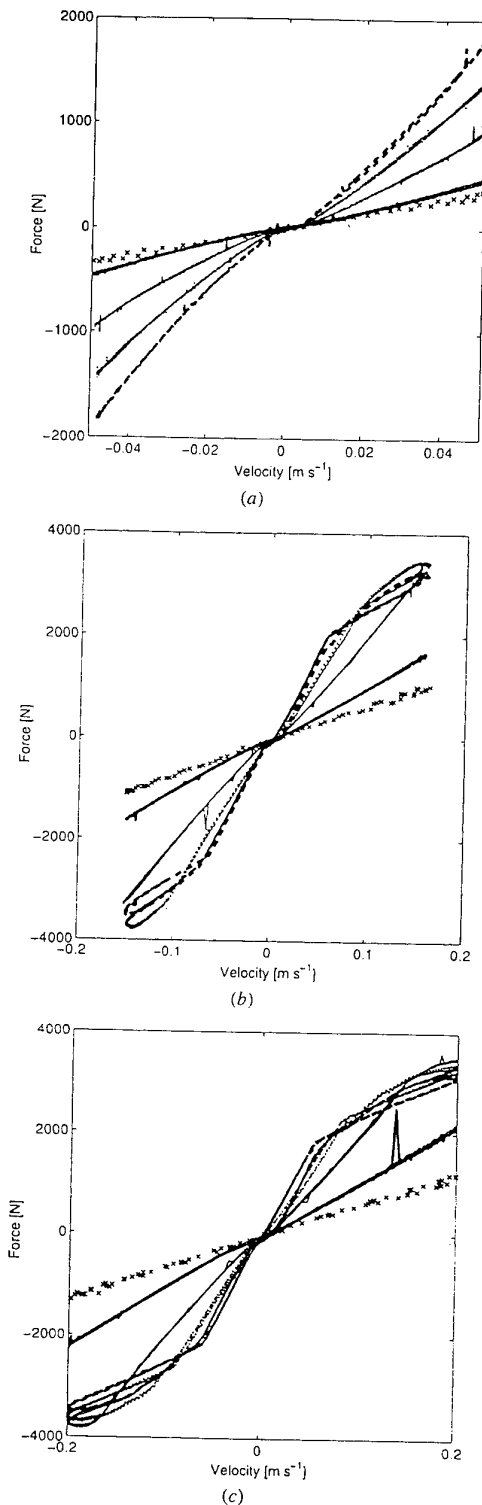


Figure 29. Experimental controlled response at (a) 1 Hz, (b) 3 Hz, (c) 4 Hz and (d) 5 Hz. —, $D = 10 \text{ kN s m}^{-1}$; —, $D = 20 \text{ kN s m}^{-1}$; ·····, $D = 30 \text{ kN s m}^{-1}$; ·····, $D = 40 \text{ kN s m}^{-1}$; × × ×, zero electric field.

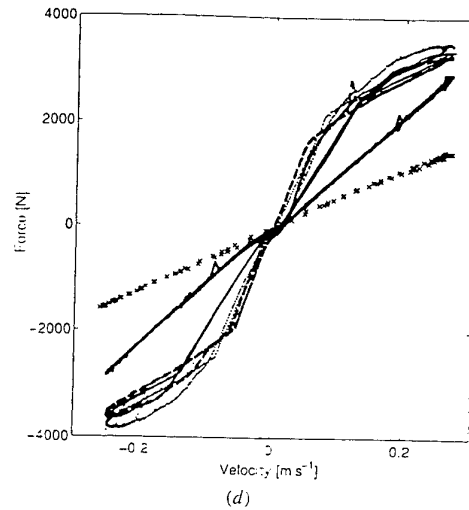


Figure 29. (Continued)

equals the set point gain D . In other words, the simulation results indicate that the device will operate as a viscous damper with a variable coefficient over the range $10\text{--}80 \text{ kN s m}^{-1}$. It remains to be established that similar performance can be achieved in practice. This is the subject of section 6.

6. Experimental closed-loop response

6.1. Implementation of the controller

We begin by developing a DSP program to control the test facility. This is a relatively straightforward task since the Simulink model of the experimental system can simply be replaced with the experimental facility itself through the appropriate ADC/DAC blocks. The resulting system is shown in figure 27, where three further modifications have been included: two pressure signals (one from each side of the piston), an output calibration sub-system and a trigger signal on the crank mechanism, which is used to calculate the mechanical excitation frequency. The output calibration sub-system accounts for the scaling requirements of the DAC and the high-voltage amplifier.

The Simulink model of the control system can now be compiled and downloaded onto the DSP controller board. The controller variables and measurement signals can then be modified and logged whilst the DSP program is running, using either Matlab or dSPACE software.

6.2. Results

A useful starting point for the investigation is to attempt to recreate the response shown in figure 26, where the simulated closed-loop response was plotted for various set point gains, with $G = 0.007$ and $B = 0.6$. The corresponding experimental response is shown in figure 28, and it can be seen that there is close agreement between the two, thus demonstrating the effectiveness of the modelling and control techniques. The response is linear within the control limits and the damping level is equal to the set-point gain. The lower

control limit is the zero electric field condition, illustrated on figure 28—it is the straight line due to the viscous damping of the fluid being forced through the annular electrode with no applied electric field. The maximum control limit can be seen on both graphs—it is the maximum allowable field strength for the fluid (4 kV mm^{-1}), and is effectively the upper saturation limit of the control signal. Even above the upper control limit, there is close agreement between the simulated and experimental responses.

The response at other frequencies, up to 5 Hz, is shown in figure 29, again using $G = 0.007$ and $B = 0.6$. Figures 29(a)–(d) illustrate how the dead band that appears at low frequencies is independent of the operating frequency and appears to have a constant velocity amplitude. So, as the operating frequency increases and the velocity amplitude increases, the dead band occurs over a much smaller portion of the response, until it is barely noticeable. Clearly, this dead band is a phenomenon that has not been accounted for in the model. Possibly it is due to nonlinear flow effects in the valve and piston arrangement. It is also apparent from figure 29 that the control limits are reached much more quickly when the operating frequency increases. This is to be expected since increasing the operating frequency has the effect of increasing the velocity amplitude.

7. Conclusions

In this paper, a closed-loop control strategy has been described, which is capable of linearizing the response of an ER long-stroke damper under experimental conditions. The control regime was first developed in an earlier feasibility study, which simulated the response of the damper under quasi-steady conditions. This paper has extended the earlier work in a number of ways.

- A new model has now been developed which is capable of predicting and explaining the damper's response under dynamic conditions, in a form that is suitable for control simulations.
- A simple correction factor has now been built into the control so that it is effective in both piston directions.
- A comprehensive model of the chosen digital controller has now been used in the control simulations.
- Experimental results have now been obtained, which demonstrate the effectiveness of the control regime under experimental conditions.

It has now been shown how a simple proportional feedback controller can be used to linearize the response of an ER long-stroke damper under laboratory conditions at frequencies up to 5 Hz. Linearized behaviour is available between well defined limits: the Newtonian characteristic in the absence of an applied electric field and the maximum force developed within the ER fluid. Also, it has been confirmed experimentally that the slope of the linearized force/velocity characteristic can be specified through the choice of a controller gain term.

There is enormous scope for future development of the control strategy. The controlled response must be investigated at higher frequencies and different displacement amplitudes, so as to establish the frequency range limitations

of the device. It is anticipated that the controller will be less effective at higher frequencies, when dynamic effects will have a greater influence and a dynamic controller may be required to account for these effects. The robustness of the regime under extremes of temperature, or poor fluid homogeneity will also require investigation before the device can be used outside the laboratory.

Acknowledgments

One of the authors (NDS) would like to thank the EPSRC for funding. The authors are also grateful for partial funding of the control equipment by the European Research Office of the US Army under contract number N68171-98-M-5388.

Appendix. Nomenclature and default values

a	Effective piston area	0.001 355 m^2
A_{e0}	ER fluid yield stress—field strength parameter	–123.6
A_{e1}	ER fluid yield stress—field strength parameter	588.9
A_{e2}	ER fluid yield stress—field strength parameter	81.06
b	Valve effective breadth	0.1021 m
c	Ideal viscous damper damping coefficient	
E	ER fluid electric field strength	
F_d	Model damper force	
f_{in}	Controller set point	
F_s	Model spring force	
F_y	Model yield force	
h	Valve gap	0.0005 m
k	Model stiffness	$9.47 \times 10^6 \text{ N m}^{-1}$
l	Valve length	0.07 m
m	Model mass	4.075 kg
Q	Volume flow rate through ER valve	
\bar{u}	Mean fluid velocity through ER valve	
\dot{x}	Piston velocity	
\ddot{x}	Piston acceleration	
x_1	Model damper displacement	
x_2	Model mass displacement	
x_3	Model spring displacement	
ΔP	Pressure differential across main piston	
P	Modified Hedström number coefficient	–3.253
γ	Quasi-steady damper function	
κ	Bilinear spring function	
η	ER fluid viscosity	0.0625 Pa s
μ_1	Friction coefficient	
μ_2	Reynolds number	
μ_3	ER fluid Hedström number	
$\mu_{3,0}$	Ideal Bingham plastic Hedström number	
ρ	ER fluid density	1024 kg m^{-3}
τ_0	Bingham plastic yield stress	
τ_1	ER fluid yield stress	
	Rheology change time constant ('Tau')	0.003 s
	Displacement amplitude	0.008 m
	Operating frequency	2 Hz

References

- Choi S B, Thompson B S and Gandhi M V 1995 Experimental control of a single-link flexible arm incorporating electrorheological fluids *J. Guidance, Control Dynamics* **18** 916–19
- Dyke S J, Spencer B F, Sain M K and Carlson J D 1996 Modeling and control of magnetorheological dampers for seismic response reduction *Smart Mater. Struct.* **5** 565–75

- Gavin H P, Hanson R D and Filisko F E 1996a Electrorheological dampers, Part I: Analysis and design *Proc. 1996 ASME Int. Mechanical Engineering Congress and Exhibition (Atlanta, GA, November 17-22, 1996) (Conf. code 45867)* (New York: ASME)
- 1996b Electrorheological dampers, Part II: Testing and modeling *Proc. 1996 ASME Int. Mechanical Engineering Congress and Exhibition (Atlanta, GA, November 17-22, 1996) (Conf. code 45867)* (New York: ASME)
- Jolly M, Bender J W and Carlson J D 1998 Properties and applications of commercial magnetorheological fluids *SPIE 5th Int. Symp. on Smart Structures and Materials (San Diego, CA, 15 March, 1998)* (Bellingham, WA: Society of Photo-Optical Instrumentation Engineers)
- Kamath G M, Hurt M K and Wereley N M 1996 Analysis and testing of Bingham plastic behavior in semi-active electrorheological fluid dampers *Smart Mater. Struct.* **5** 576-90
- Kamath G M, Wereley N M and Jolly M R 1997 Analysis and testing of a model-scale magnetorheological fluid helicopter lag mode damper *Ann. Forum Proc. American Helicopter Society* **2** 1325-35
- Makris N, Burton S A and Taylor D P 1996 Electrorheological damper with annular ducts for seismic protection applications *Smart Mater. Struct.* **5** 551-64
- Matlab 1999 The MathWorks Inc 25 Prime Park Way, Natick, MA, USA
- Peel D J, Stanway R and Bullough W A 1996 Engineering with ER fluids: a design methodology based upon generalised fluid data *Proc. 3rd Int. Conf. on Intelligent Materials and 3rd Eur. Conf. on Smart Structures and Materials (Lyon, June 3-5 1996) (Conf. code 22552)* vol 2778 pp 310-16
- Scarborough J B 1958 *Numerical Mathematical Analysis* (Oxford: Oxford University Press)
- Sims N D, Stanway R and Johnson A R 1999b Vibration control using smart fluids: a state-of-the-art review *Shock Vibr. Digest* **31** 195-204
- Sims N D, Peel D J, Stanway R, Johnson A R and Bullough W A 1999a The electrorheological long stroke damper: a new modelling technique with experimental validation *J. Sound Vib.* at press
- Sims N D, Stanway R, and Beck S B M 1997 Proportional feedback control of an electrorheological vibration damper *J. Intell. Mater. Syst. Struct.* **8** 426-33
- Simulink 1999 The MathWorks, Inc. 25 Prime Park Way, Natick, MA, USA
- The MathWorks 1997 Using Simulink
- West J C 1960 *Analytical Techniques for Non-linear Control Systems* (London: The English Universities Press)
- Wilkinson W L 1960 *Non-Newtonian Fluids* (Oxford: Pergamon)

APPENDIX D

Copy of Chantalakhana, C. and Stanway, R., 2000. "Active constrained layer damping of plate vibrations: a numerical and experimental study of modal controllers", Smart Materials and Structures, submitted.

TITLE:
ACTIVE CONSTRAINED LAYER DAMPING OF PLATE VIBRATIONS:
A NUMERICAL AND EXPERIMENTAL STUDY OF MODAL CONTROLLERS

AUTHORS:
C. CHANTALAKHANA AND R. STANWAY*

ADDRESS:
*Department of Mechanical Engineering, University of Sheffield, Mappin Street
Sheffield S1 3JD, United Kingdom*

THIS PAPER CONTAINS 36 PAGES, 4 TABLES AND 25 FIGURES.

SUMMARY

In this paper the authors address the problem of suppressing the vibrations of a clamped-clamped plate using an active constrained layer damping treatment. This treatment involves adding viscoelastic and metallic constraining layers to the host plate and then augmenting this arrangement with an active feedback scheme using piezo-electric actuators. The basis of the control strategy is an effective model of the plate together with the passive damping treatment. The paper summarises the modelling procedures including the finite element formulation, model reduction and model updating. By this means a low-order model, capable of accounting for observed behaviour, is developed.

Emphasis is placed upon the design and implementation of active modal controllers based upon the reduced and updated model. Four actuator/sensor configurations are examined in both numerical and experimental studies. It is shown that effective control of the first two modes of vibration (bending and torsion) can be achieved using only a single actuator and single sensor. However, the most effective configuration involves two actuators and two sensors operating as two independent control channels. It is shown that through suitable design, the active constrained layer damping treatment is capable of avoiding problems due to spillover effects.

* Author to whom correspondence should be addressed.

1. INTRODUCTION

A previous study by Azvine and his colleagues (1994) examined the vibrations of a clamped-clamped plate using an active constrained layer damping treatment (ACLD). The plate was a simplified version of an instrument box cover found in a military aircraft. Excessive bending and torsional vibrations were causing the instrument box to malfunction in service. Consequently, Azvine's brief was to investigate ACLD treatments as a means of suppressing these undesirable levels of vibration.

The ACLD approach involves augmenting a conventional passive constrained layer damping treatment with active control, the latter typically implemented using piezoelectric actuators. The feasibility of applying an ACLD treatment was demonstrated by Baz and Ro (1993) who initially examined a cantilevered beam before progressing to more complex structures such as a cantilevered plate (Baz and Ro, 1996). It is now well established that the passive constrained damping layer is effective at suppressing higher frequency modes of vibration while the active scheme can be designed to suppress the lower frequency modes. Furthermore the presence of the passive treatment introduces sufficient inherent damping so as to minimise the influence of spillover effects which are liable to degrade or even de-stabilise mechanical structures under active control. A recent study (Veley and Rao, 1996) compared ACLD treatments with purely active and purely passive schemes using both a cantilevered beam and a plate clamped on all four sides. It was shown that the ACLD is superior to active schemes in that desired levels of damping can be introduced using with significantly less additional weight.

Whereas there remains little doubt about the capabilities of ACLD as an effective technique for vibration control of thin-walled structures, there is still considerable scope for the development of control algorithms. In particular, the study by Azvine et al (1994) demonstrated the need for improved models of the host plate, the viscoelastic and

constraining layers and a more effective control algorithm based upon the use of these models.

A previous paper by the present authors (Chantalakhana and Stanway, 2000) described a technique for modelling the clamped-clamped plate and showed preliminary experimental results using a modal controller based upon the improved model. In what follows here, the authors will summarise the modelling procedures before focusing on a comprehensive series of numerical and experimental investigations into control of the plate vibrations.

2. SUMMARY OF MODELLING PROCEDURES

2.1 Introduction

It was decided at the outset to develop a model-based approach to controlling the vibrations of the clamped-clamped plate. The starting point was a finite-element of the host plate extended to account for the behaviour of the added viscoelastic and metallic constraining layers. To obtain a model suitable as the basis for controller design, it was necessary to apply model reduction techniques. In order to obtain sufficiently close correspondence between the predictions of the reduced-order model and experimental measurements, it was necessary to apply model updating algorithms. The modelling procedures are described in detail by Chantalakhana and Stanway (2000) and are summarised in the sub-sections which follow.

2.2 Clamped-clamped plate: physical arrangement

The basic experimental facility is shown in Figure 1. Essentially the plate is made of aluminium and has the dimensions 2.5 mm \times 305 mm \times 490 mm and is firmly clamped along the two shorter sides. To the host plate was added a viscoelastic layer (3M

Company, type ISD112) of thickness $50.8\text{ }\mu\text{m}$ (0.002 in). A steel shim of thickness $254\text{ }\mu\text{m}$ (0.010 in) was used as the constraining layer. The material properties for all three layers are given in Table 1. For preliminary experiments to examine the dynamics of the plate, a single shaker and accelerometer were located at node 7, as shown in Figure 1. With this arrangement it was established that at least ten modes of vibration could be excited and detected.

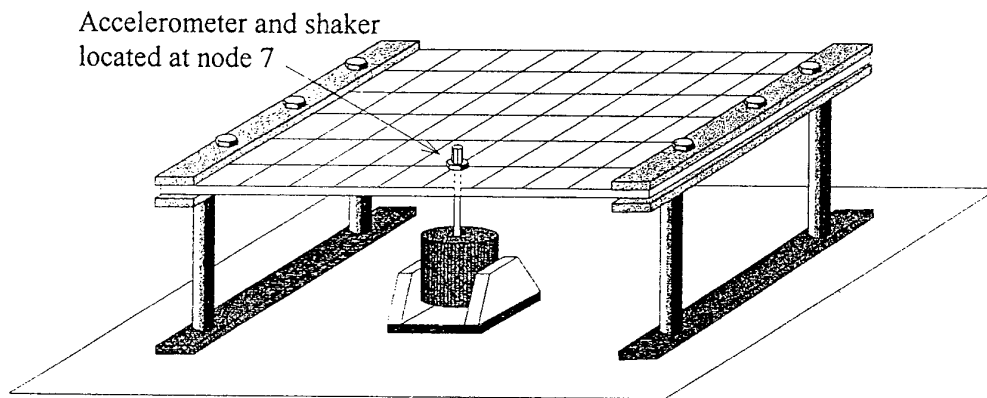


Figure 1. Experimental arrangement of the clamped-clamped plate for passive constrained layer damping experiments

Table 1
Material properties of three-layer plate

Material	modulus of elasticity (MPa)	modulus of rigidity (MPa)	density (kg/m^3)	Poisson's ratio	shear loss factor
aluminium plate	70×10^3	-	2700	0.3	-
ISD112 viscoelastic layer	29.8^*	20^*	1140	0.49	1.0^*
steel constraining layer	200×10^3	-	7000	0.3	-

* at the centre frequency of 600 Hz

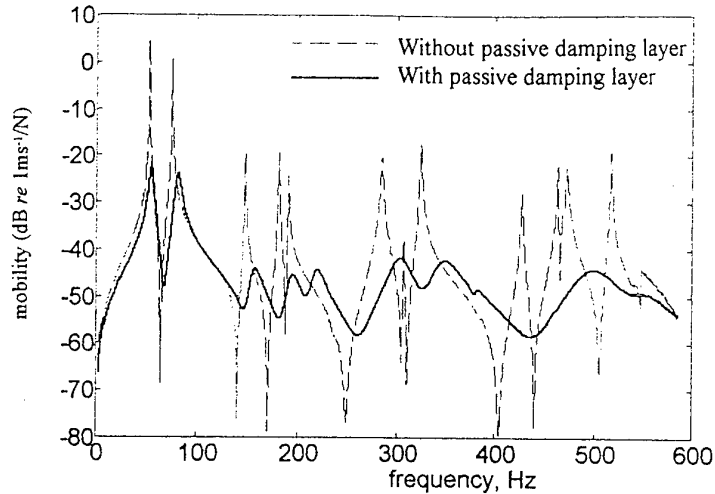


Figure 2. Measured FRFs of the panel plate with and without constrained damping layer

Figure 2, which was generated during the preliminary experiments, shows the influence of the passive constrained damping layer compared with the response of the untreated host plate. Note that the introduction of the damping layer produces around 25 dB attenuation of all the modes up to 600 Hz. However, the vibrations associated with the first two modes still produce mobility peaks some 20 dB above those associated with the higher modes. It is these first two modes, one bending and one torsion, which require the use of active control to introduce significant additional attenuation of vibration levels. Before proceeding to describe active constrained layer damping it is necessary to refine the finite element model of the passively damped plate.

2.3 Finite element model

The finite element modelling technique follows the approach described by Baz and Ro (1996). Rectangular elements are used and at each node there are 7 degrees of freedom, 4 longitudinal, 1 transverse and 2 rotational displacements. The equation of motion is formed as

$$\mathbf{M}_j \ddot{\Delta}_j + \overline{\mathbf{K}}_j \Delta_j = \mathbf{F}_j \quad (1)$$

where \mathbf{M}_j and $\overline{\mathbf{K}}_j$ are, respectively, the mass and stiffness matrices of element j and \mathbf{F}_j is an external force vector acting at the j^{th} element. Note that $\overline{\mathbf{K}}$ is a complex stiffness matrix whose imaginary term serves as a loss energy or damping term. Full details of the formulation and validation of this finite element model are given by Chantalakhana and Stanway (1998). A comparison between the predicted FRF from the finite element model and the FRF measured experimentally, Figure 3, shows that the response levels predicted by the model are consistent with the results from the experiments. However, note that the predicted natural frequencies are shifted to the right of the experimental results. Figure 4 shows the first six mode shapes of the clamped-clamped plate obtained from solving eigensolutions of Equation (1) in which the plate is divided as 9 by 6 elements along the length and width directions, respectively.

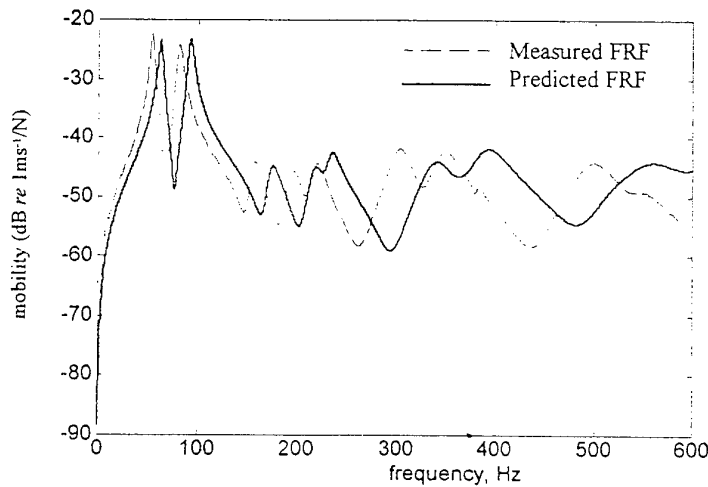


Figure 3. Measured and predicted FRFs (point mobility, the same point for acting force and velocity response) of the panel plate covered with constrained damping layer

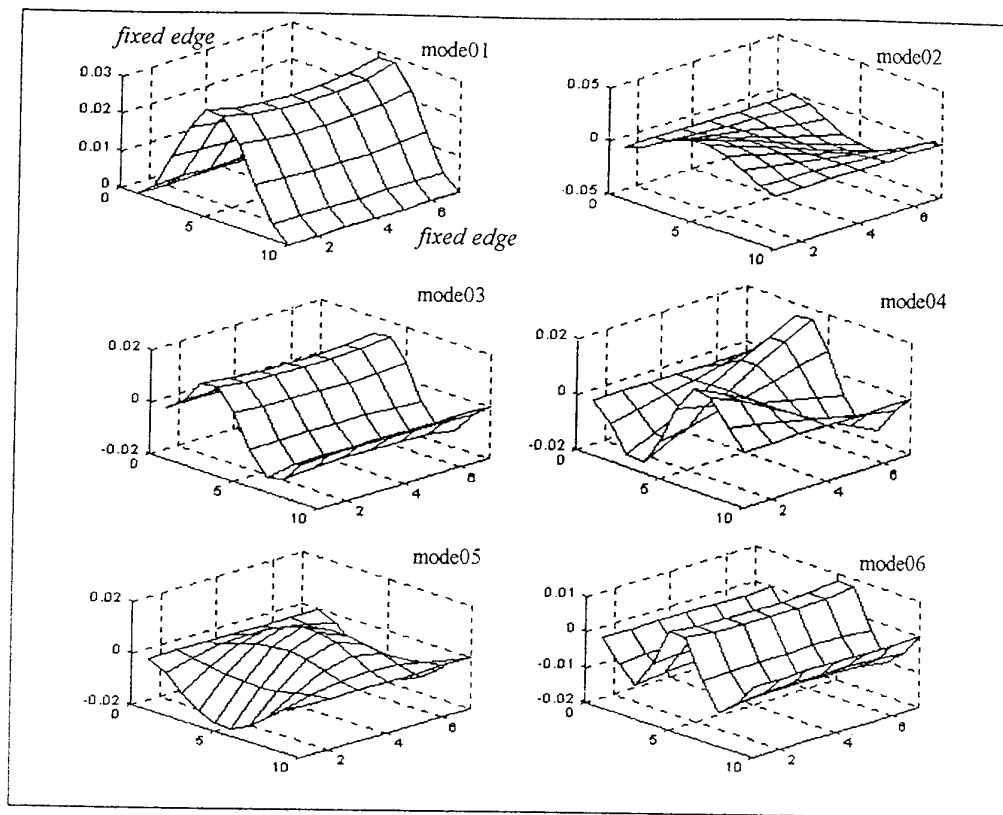


Figure 4. The first six mode shapes of the clamped-clamped plate

2.4 Model updating

It was noted in sub-section 2.3 that the FRF predicted by the finite element model is shifted to the right of the experimental FRF. In order to produce a closer match between predicted and observed FRFs, a model updating procedure was applied. The algorithm used, based upon a pole placement technique, was originally described by Inman and Minas (1990), where full details can be found.

This model updating algorithm requires that the imaginary term in the complex stiffness matrix $\bar{\mathbf{K}}$, in Equation (1), be transformed to a viscous damping matrix. A complication arises in that the resulting viscous damping coefficients are frequency dependent. The algorithm used to achieve this damping transformation was adapted from work by Minas and Inman (1989). Although the transformation is straightforward in

principle, difficulties arose in the present application owing to the dimensions of the matrices which are involved. Essentially, the pseudo-inverse of an over-determined system of linear equations incorporating a $2n^2 \times (n^2 + n)/2$ order matrix needs to be computed. Given that the number of degrees of freedom, n , in the original finite element model is 420, it was necessary to reduce the size of the mass and complex stiffness matrices in Equation (1) before implementing the transformation.

The Guyan technique (1965) was used for model reduction. In this way the number of degrees of freedom was reduced from 420 to 36. Figure 5 shows selected nodes and displacements nominated for the reduced-order model. The master nodes in the reduced-order model were chosen to ensure an adequate reduced-order model over bandwidth of interest and also to maintain correspondence with the measurement locations used in the subsequent experimental work.

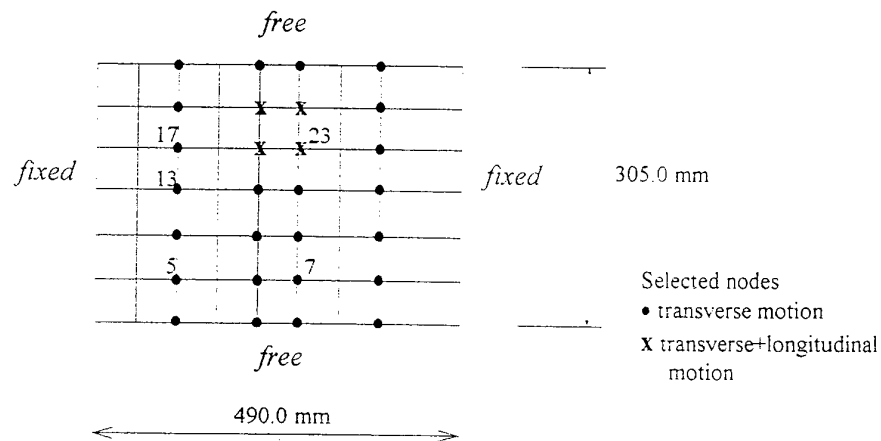


Figure 5. Division of plate to finite elements and selected nodes for model reduction

Following model reduction and transformation of the complex stiffness matrix, \bar{K} , model updating was applied to improve correspondence between predicted and observed FRFs. The updating procedure requires estimates of the natural frequencies and damping factors obtained from the experimental facility. Since the modes of the clamped-

clamped plate are well separated, it is possible to use a peak-picking method to identify the natural frequencies and damping ratios (LMS, 1993). Table 2 gives the identified natural frequencies and percentage damping factors of the first 6 modes compared with those predicted by the finite element model. These predictions were obtained from the reduced model (of order r) which is to be updated with the eigenvalues of the full plate model (of order n).

Table 2
Measured and predicted first six natural frequencies
and damping factors of three-layer plate

mode	1	2	3	4	5	6
predicted natural frequency (Hz)	62.50	92.23	172.93	217.07	233.02	339.06
measured natural frequency (Hz)	54.53	81.50	157.47	195.59	220.60	304.02
predicted % damping	3.50	3.05	3.81	3.87	2.83	4.86
measured % damping	3.44	3.51	4.13	3.66	3.41	3.57

A typical result of model updating is shown in Figure 6. This result shows that the first six modes in the predicted FRFs are concurrent with the measured FRFs. Higher modes are not updated and thus remain unchanged. In the sections which follow, it will be shown that the updated model forms a suitable basis for the design of an active modal controller which complements the damping introduced by the passive constrained layer treatment.

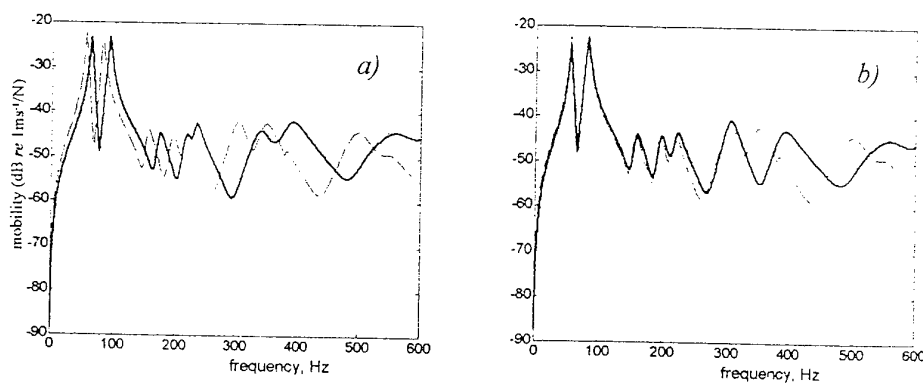


Figure 6. FRF7_7 a) before updating
b) after updating the model

3. CONTROL AND NUMERICAL EXPERIMENTS

3.1 Modal control

The well-established finite element model of three-layer plate summarised in the previous section, will be used here as the basis for the design of active control schemes. The number of degrees of freedom of the model has been reduced by eliminating insignificant variables. The model has also been updated so that observed behaviour of the test plate matches the model predictions. Modal control via pole placement is the method to be used for control. Spillover effects and their avoidance are emphasised.

3.1.1 State-space equations

For a finite element plate model reduced to r degrees of freedom, the corresponding state-space equation of motion can be written as a set of $2r$ first order differential equations :

$$\begin{Bmatrix} \ddot{\Delta} \\ \dot{\Delta} \end{Bmatrix} = \begin{bmatrix} 0 & \mathbf{M}^R \\ \mathbf{M}^R & \mathbf{D}^R \end{bmatrix}^{-1} \begin{bmatrix} \mathbf{M}^R & 0 \\ 0 & -\mathbf{K}^R \end{bmatrix} \begin{Bmatrix} \dot{\Delta} \\ \Delta \end{Bmatrix} + \begin{bmatrix} 0 & \mathbf{M}^R \\ \mathbf{M}^R & \mathbf{D}^R \end{bmatrix}^{-1} \begin{Bmatrix} 0 \\ \mathbf{F} \end{Bmatrix} \quad (2)$$

where Δ is an $r \times 1$ displacement vector, \mathbf{M}^R , \mathbf{D}^R and \mathbf{K}^R are $r \times r$ the reduced-order mass, damping and stiffness matrices, respectively, and \mathbf{F} is an $r \times 1$ force vector acting at the nodal displacements. For the special case of a single input force, Equation (2) may written in the form

$$\dot{\mathbf{Y}} = \mathbf{A}\mathbf{Y} + \mathbf{b}f \quad (3)$$

where $\mathbf{Y}_{2r \times 1} = \begin{bmatrix} \dot{\Delta}^T & \Delta^T \end{bmatrix}^T$, $\mathbf{A}_{2r \times 2r}$ is a plant matrix, $\mathbf{b}_{2r \times 1}$ is an input vector or $\mathbf{b} = \begin{bmatrix} (\mathbf{M}^{-1}\mathbf{F})^T & 0 \end{bmatrix}^T$ and f is a scalar input. Let $\mathbf{Y} = \mathbf{U}\xi$, where $\xi_{2r \times 1}$ is a modal state variable vector and $\mathbf{U}_{2r \times 2r}$ is a transformation matrix containing $2r$ columns of the eigenvectors of \mathbf{A} . After substituting this transformation into Equation (3) and pre-multiplying by \mathbf{U}^{-1} , then Equation (3) becomes

$$\dot{\xi} = \Lambda\xi + \mathbf{w}f \quad (4)$$

where $\Lambda = \mathbf{U}^{-1}\mathbf{A}\mathbf{U}$ is a diagonal matrix containing $2r$ eigenvalues of \mathbf{A} along its diagonal elements, $\mathbf{w} = \mathbf{U}^{-1}\mathbf{b}$ is a modal controllability vector in which an element j of \mathbf{w} quantifies controllability of the j th mode by the input f . This transformation results in the decoupling of Equation (3). If Equation (4) is partitioned as c controlled mode equations and u residual or uncontrolled mode equations, then Equation (4) can be rearranged as

$$\begin{Bmatrix} \dot{\xi}_c \\ \dot{\xi}_u \end{Bmatrix} = \begin{bmatrix} \Lambda_c & \mathbf{0} \\ \mathbf{0} & \Lambda_u \end{bmatrix} \begin{Bmatrix} \xi_c \\ \xi_u \end{Bmatrix} + \begin{Bmatrix} \mathbf{w}_c \\ \mathbf{w}_u \end{Bmatrix} f \quad (5)$$

The c eigenvalues can be shifted to their desired values by feeding back the vector of state variables ξ_c , as a scalar input f with appropriate weightings

$$f = \mathbf{k}_c^T \xi_c \quad (6)$$

where \mathbf{k}_c is a $c \times l$ gain vector.

Note that substitution of Equation (6) into Equation (5) results in force coupling in the system equation due to a coupling input matrix $(\mathbf{w}_c \mathbf{k}_c^T)_{c \times c}$. Modal decomposition attempts to decouple a system of equations so that each mode can be controlled independently. The force coupling effect results in the benefit of simultaneous control of several modes with possibly a single actuator where the controllability element j , corresponding to the j th controlled mode, is non-zero.

3.1.2 State estimator

The scalar feedback input f in Equation (6) is formed from the modal state variable vector ξ_c which needs to be computed from physical measurements. If $\mathbf{z}_{l \times 1}$ is a vector of physical observations where l is a number of available measurements, the relationship between this vector and the vector of physical co-ordinates $\mathbf{Y}_{2r \times 1}$ is

$$\mathbf{z} = \mathbf{L}\mathbf{Y} \quad (7)$$

where L_{k2r} is an output matrix. In modal co-ordinates, Equation (7) becomes

$$\mathbf{z} = \mathbf{L}\mathbf{U}\xi \quad (8)$$

or

$$\mathbf{z} = \begin{bmatrix} \mathbf{H}_c^T & \mathbf{H}_u^T \end{bmatrix} \begin{Bmatrix} \xi_c \\ \xi_u \end{Bmatrix}. \quad (9)$$

An observability vector can be defined at this stage as $\mathbf{v} = \mathbf{U}^T \mathbf{L}^T$ which the j th element in the vector represents the observability of a modal state variable ξ_j . Using with Equations (6) and (9), a set of c controlled mode equations defines the modal state estimator :

$$\hat{\xi}_c = (\Lambda_c + \mathbf{w}_c \mathbf{k}_c^T) \hat{\xi}_c + \Phi (\mathbf{z} - \mathbf{h}(\hat{\xi}_c, t)) \quad (10)$$

where $\hat{\xi}_c$ is the estimate of ξ_c , $\mathbf{h}(\hat{\xi}_c, t) = \mathbf{H}_c^T \hat{\xi}_c$ is the estimate of \mathbf{z} , and Φ_{cxl} is a weighting matrix.

3.1.3 Spillover effects

Balas (1978) showed that using a reduced set of equations for the controller and estimator causes, respectively, control and observation spillover. A scalar input force f can excite the controllable residual modes (see Equation (5)) because of the force coupling which is present. Similarly, Equation (10) shows that if the measurement signal includes terms from the residual state variable ξ_u , then the estimator is contaminated by values of $\Phi(\mathbf{H}_u^T \xi_u)$. These spillover effects can cause instability in the controlled structure.

However, these effects can be reduced by keeping the elements of gain vector \mathbf{k}_c^T and the weighting matrix Φ low. Optimal designs such as the linear quadratic regulator and Kalman filter (Franklin et al, 1998) can be used to achieve the low gains. Placement of actuator and sensor should be close to the nodal lines of residual modes so that the

residual modes are not significantly excited and the residual state variables in ξ_u are not strongly observed.

3.1.4 Control law and estimator design

Continuous-time design

For the state-space equations with a single input and single output, the control gain vector \mathbf{k}_c^T (see Equation (6)) and weighting gain vector Φ (see Equation (10)) can be assigned using a pole placement technique. However, to optimise actuator power consumption and damping of the assigned modes, Linear Quadratic Regulator (LQR) and Gaussian (LQG) algorithms are used to obtain optimal control and estimator gains, respectively, so that the spillover effects are not sufficient to destabilise the actively controlled system. The LQR is the solution provided by solving a general optimal control problem to find the control gains. However, a drawback is that the entire set of state variables must be measured. The LQG controller is provided by the solution of an extended optimal control problem where white noise disturbance inputs are included and incomplete state measurements can be used to construct the full state vector through computing the appropriate estimator gains (Burl, 1999). The LQR design is aimed at minimising the cost function

$$\mathbf{J} = \int (\xi^T \mathbf{Q} \xi + f^T \mathbf{R} f) dt \quad (11)$$

where \mathbf{Q} and \mathbf{R} are weighting matrices. One choice of \mathbf{Q} and \mathbf{R} is to make them symmetrical (semi-symmetrical for \mathbf{Q}) positive definite matrices. For a SISO modal state-space equation, \mathbf{R} is a scalar and can be set to unity while \mathbf{Q} is of the form

$$\begin{bmatrix} a_1 & \cdots & \cdots & 0 \\ \vdots & a_1 & & \vdots \\ \vdots & & a_2 & \vdots \\ 0 & \cdots & \cdots & a_2 \end{bmatrix} \quad (12)$$

where a_1 and a_2 are real constants, chosen so as to maintain two pairs of complex conjugate eigenvalues. Increasing a_1 and a_2 results in an increase in the damping of the assigned eigenvalues which correspond to the original modes 1 and 2 respectively. The control gains must not be so high such that control spillover affects the results. The influence of a truncated model on the assigned eigenvalues of a closed-loop system will be discussed later.

Traditionally the estimator gains are chosen to provide poles to the left of the assigned poles in the left-hand half of the s-plane. Equations (5), (6) and (10) can be rewritten in terms of the error of the estimation process

$$\dot{\mathbf{e}} = \begin{pmatrix} \hat{\xi}_c - \xi_c \end{pmatrix} = (\Lambda_c - \Phi \mathbf{H}_c^T) \mathbf{e} + \Phi \mathbf{H}_u^T \xi_u \quad (13)$$

The decay of the estimator error is thus dependent on the eigenvalues of $(\Lambda_c - \Phi \mathbf{H}_c^T)$. If the estimator gains are chosen to be high so as to achieve rapid decay of the error terms, then contamination of the uncontrolled modes is also amplified, resulting in a significant observation spillover effect. The effect of spillover on the assigned close-loop poles can be studied by considering Equations (5), (6) and (13) (a combination of a modal state-space equation involving the controlled modes, uncontrolled modes and state estimation error (Balas, 1978)):

$$\begin{Bmatrix} \dot{\xi}_c \\ \mathbf{e} \\ \dot{\xi}_u \end{Bmatrix} = \begin{bmatrix} \Lambda_c + \mathbf{w}_c \mathbf{k}_c^T & \mathbf{w}_c \mathbf{k}_c^T & 0 \\ 0 & \Lambda_c - \Phi \mathbf{H}_c^T & \Phi \mathbf{H}_u^T \\ \mathbf{w}_u \mathbf{k}_c^T & \mathbf{w}_u \mathbf{k}_c^T & \Lambda_u \end{bmatrix} \begin{Bmatrix} \xi_c \\ \mathbf{e} \\ \xi_u \end{Bmatrix} \quad (14)$$

As indicated in sub-section 3.1.3, the assigned eigenvalues are disturbed by the residual terms of the observation signal. Both the actual closed-loop eigenvalues and the stability of the control system including spillover effects can be investigated by obtaining the eigensolutions of Equation (14).

Discrete-time design

In the discrete-time domain, the controlled mode state-space equations of motion corresponding to Equation (5) can be obtained from (for example, see Ogata, 1987)

$$\Lambda_c^d = e^{\Lambda_c T_s}, \mathbf{w}_c^d = (e^{\Lambda_c T_s} - \mathbf{I})\Lambda_c^{-1}\mathbf{w}_c \quad (15)$$

where Λ_c^d is the discrete-time form of Λ_c and T_s is sampling time. An advantage of controller design in modal co-ordinates is that the exponential of the plant matrix Λ_c is straightforward to compute because it contains only diagonal elements. Elements in the discrete-time control gain \mathbf{k}_c^T are then calculated from (Porter and Crossley, 1972)

$$k_j^d = \frac{\prod_{k=1}^c (\exp(\rho_k T_s) - \exp(\lambda_j T_s))}{\left(w_{c,j}^d \prod_{\substack{k \neq j \\ k=1}}^c (\exp(\lambda_k T_s) - \exp(\lambda_j T_s)) \right)} \quad j=1,2,\dots,c \quad (16)$$

where $\lambda_{j,k}$ is eigenvalue of the mode to be controlled, ρ_k is assigned eigenvalues obtained from the LQR design, c is the number of controlled modes and $w_{c,j}^d$ is the j th element of \mathbf{w}_c^d . The estimator state-space equation (Equation (10)) is rewritten here

$$\hat{\xi}_c(t) = (\Lambda_c - \Phi \mathbf{H}_c^T) \hat{\xi}_c(t) + \Phi z(t) + \mathbf{w}_c f(t) \quad (17)$$

For compactness, define $\bar{\mathbf{G}} = (\Lambda_c - \Phi \mathbf{H}_c^T)$. Then the discrete-time estimator takes the form

$$\hat{\xi}_c(k+1) = \bar{\mathbf{G}}^d \hat{\xi}_c(k) + \Phi^d z(k) + \bar{\mathbf{w}}_c^d f(k) \quad (18)$$

where $\bar{\mathbf{G}}^d = e^{\bar{\mathbf{G}} T_s}$, $\Phi^d = (e^{\bar{\mathbf{G}} T_s} - \mathbf{I})\bar{\mathbf{G}}^{-1}\Phi$, $\bar{\mathbf{w}}_c^d = (e^{\bar{\mathbf{G}} T_s} - \mathbf{I})\bar{\mathbf{G}}^{-1}\mathbf{w}_c$ and k is the sampling index. From Equations (15) to (18), the discrete modal controller can be formulated to implement digital control used in the following section.

3.2 Description of numerical experiments

Numerical simulations of an actively controlled system were performed to investigate the performance of the controller designs. In what follows, various configurations of control device arrangement are examined using simulation procedures. A series of simulation results is given and will be compared with experimental results in the next section.

Configuration 1: a single PZT actuator and single accelerometer

Plots of mode shapes were considered and the sensor and actuator were chosen to occupy the middle of the upper half portion of the plate as illustrated in Figure 7. The dimensions of the PZT actuator were chosen based upon the results obtained by finite element modelling and experimental observations. A 50 mm \times 50 mm PZT patch was used as the actuator. A square shape of PZT patch results in generating forces in both x and y directions (Figure 7). With this location, the sensor and actuator, respectively, detect and excite the maximum transverse displacements associated with the first two modes whilst also keeping to the nodal lines of the higher modes so as to minimise spillover effects. Modal controllability and observability vectors were also used to refine the choices of the sensor and actuator locations (Chantalakhana and Stanway, 2000). The disturbance (shaker position) and measurement points are at points 7 and 23, respectively, on the three-layer test plate as shown in Figure 7. The control excitation is applied to a PZT actuator placed in the middle of upper portion of plate. The controller and estimator gains are designed to produce high damping of the first two eigenvalues and to ensure stability of the closed-loop system in the face of spillover effects. The assigned eigenvalues, along with controller and estimator gains are given in Table 3. The assigned poles are obtained by using the LQR design to minimise the control gain and to achieve high damping. The LQG design is used to obtain the optimal estimator gain such that the error from

estimation decays faster than the response due to the assigned poles. The main consideration in designing the controller is to minimise spillover problems. The complete closed-loop control system for numerical experiments, is shown in Figure 8.

In controller design, the control law and estimator are implemented using complex numbers - a formulation which is not suitable for experimental implementation by real-time digital control. To overcome this problem, the state-space estimator equation is converted to its transfer function form so that real and imaginary terms can be computed separately in terms of real numbers, as illustrated in Figure 8. This significantly reduces the number of lines required for program execution and results in faster calculations for real-time control.

Table 3

Poles and corresponding gains of controller and estimator

mode	original poles(rad/s)	assigned poles(rad/s)	control gain	estimator gain
1	$-11.78 \pm 343i$	$-105.6 \pm 339i$	$-4.88 \pm 5.61I$	$-1313 \pm 387i$
2	$-17.96 \pm 512i$	$-74.6 \pm 498i$	$5.08 \pm 3.80I$	$-720 \pm 302i$

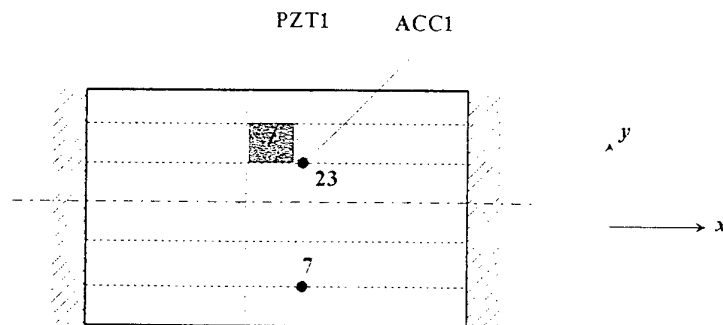
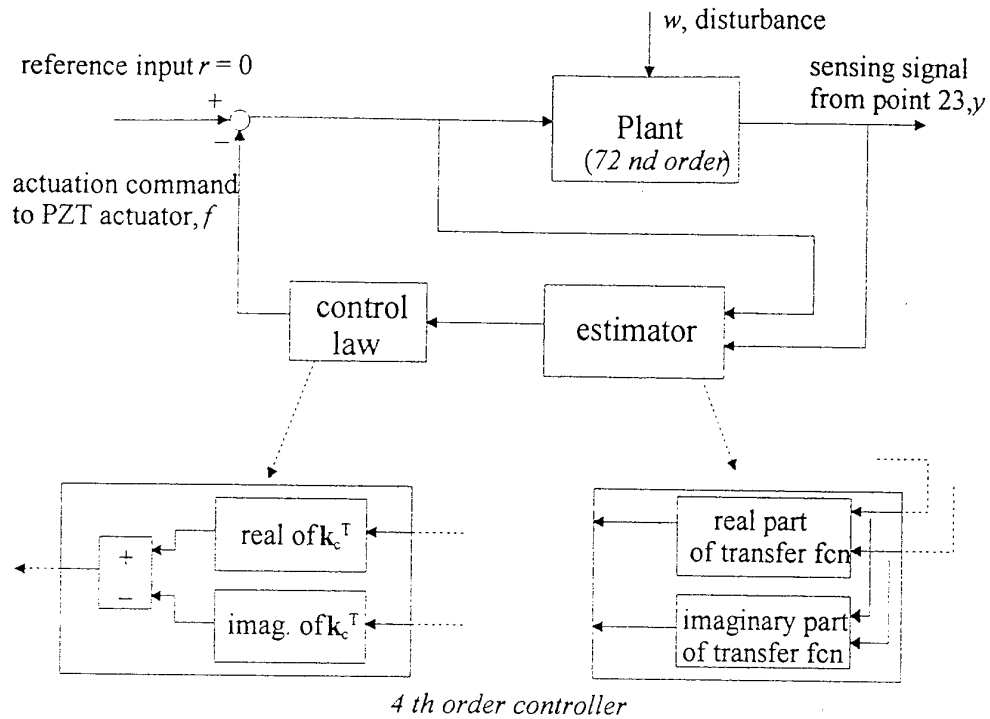


Figure 7. Arrangement of the clamped-clamped plate with a square PZT element used as actuator, an accelerometer for sensing at point 23 and shaker location at point 7 used in simulation of active constrained layer damping



Implementing a complex number controller using real

Figure 8. Block diagram of digital control simulation to match with real-time interface using SIMULINK software

For the numerical simulations, a 72nd-order plant equation together with a truncated, 4th-order controller is used to investigate the performance of active controlled system and the influence of spillover effects. FRFs from numerical simulations of the SISO configuration of the actively controlled system shown in Figure 7 are plotted in Figure 9 where notation FRF7_23 is referred to disturbance and measurement locations at points 7 and 23 respectively. Compared to the passively damped plate, the FRF of the actively controlled one shows significant attenuation of vibration levels of the first two modes. However, higher frequency modes tend to be excited so that their amplitudes increase slightly. Experimental verification of the simulation results and study of other

control configurations to obtain effective performance and overcome spillover effects are presented in the following sub-section where simulation procedures described in this section will be used to obtain numerical results for a comparison with experimental results in the next section.

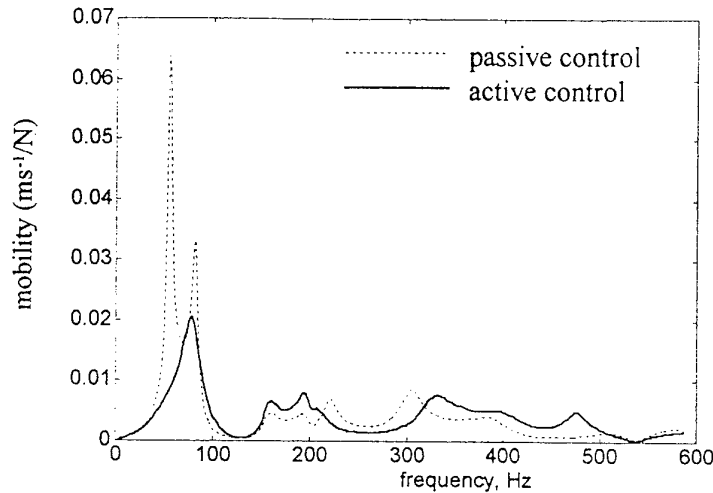


Figure 9. Simulation results: predicted FRFs (FRF7_23) of three-layer plate with and without active control for a single PZT actuator and a single accelerometer

Configuration 2: a PZT actuator operating in the x direction only

In configuration 1, a 50 mm \times 50 mm element of PZT material was used as an actuator which operates in both the x and y directions. In principle, the intention of the active control strategy is to increase the induced shear strain in the x direction where bending curvature of the first two modes occur. Actuation of the PZT actuator in the y direction causes an excessive load of the actuator and may excite higher frequency modes of vibration as already shown in Figures 9. To activate the PZT actuator in the x direction only, the length of the PZT should be longer than 3.5 times their width and thickness (Morgan Matroc, 1999). Thus, a 50 mm \times 50 mm PZT patch is cut into 4 strips of equal width and attached to the plate as shown in Figure 10.

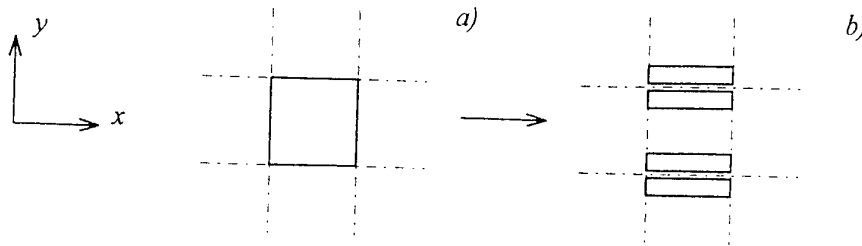


Figure 10. Configuration of PZT actuator
a) for operation in x and y directions
b) for operation in x direction only

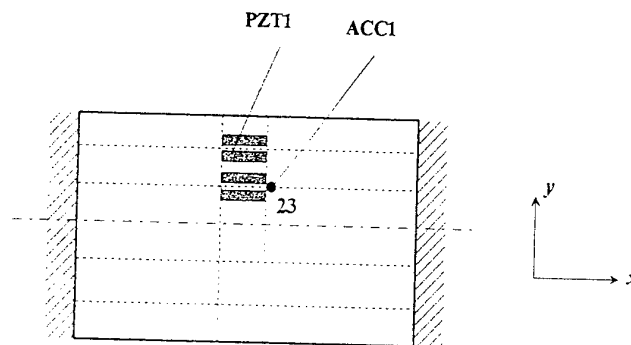


Figure 11. Arrangement of the clamped-clamped plate with 4-strip PZT elements used as actuator and a single accelerometer for sensing

The arrangement of sensor and actuator for this arrangement is shown in Figure 11. The simulation results in Figure 12 show the influence of activating the PZT element in the x direction only. The results demonstrate that superior suppression of vibrations is obtained. In addition, the power consumption for the PZT actuator decreases when actuation is in one direction only (Chantalakhana and Stanway, 2000).

Configuration 3: two PZT actuators with a two-channel amplifier and one accelerometer
As suggested by Azvine et al (1994), a negative velocity feedback controller using non-collocated sensors and actuators can degrade the performance of the active vibration control system. In the present study, a two-channel voltage amplifier for PZT actuators

(PZT1 and PZT2 in Figure 13) is used to provide independently actuator commands for each PZT actuator. In addition, it is not necessary to design for use a multiple-input, multiple-output modal controller with collocated sensors and actuators.

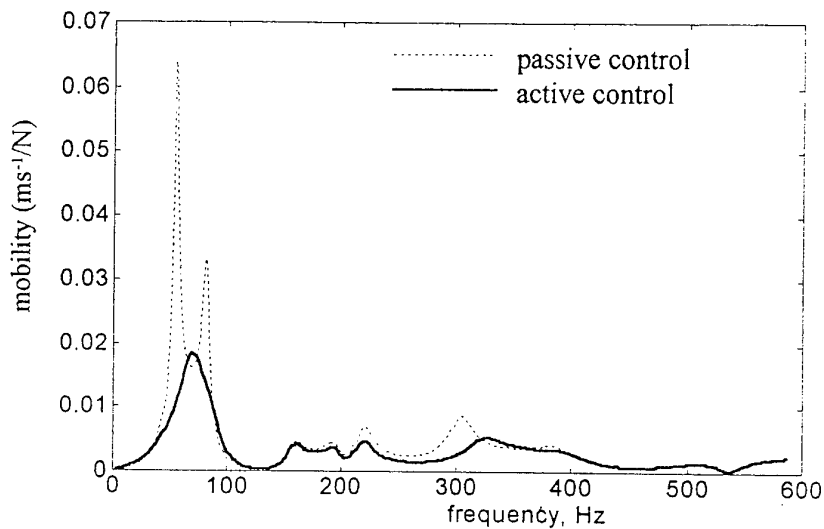


Figure 12. Simulation results: predicted FRFs (FRF7_23) of three-layer plate with and without active control for PZT actuator operating in x direction only (Figure 11)

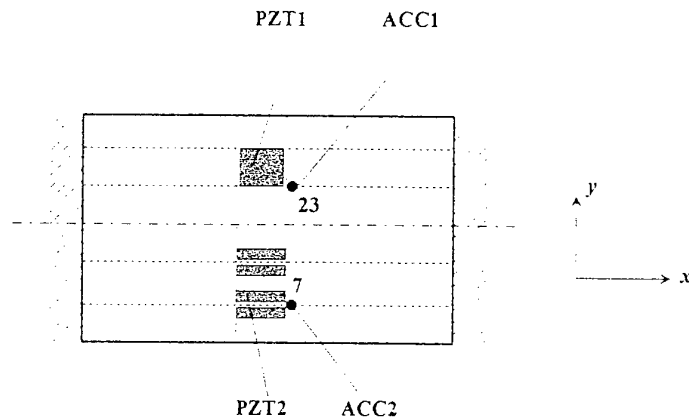


Figure 13. Arrangement of the clamped-clamped plate with 2 PZT actuators (one square element and one 4-strip element) and 2 accelerometers for sensing

Initially, two PZT actuators, PZT1 and 2, and single accelerometer, ACC1, are used in the numerical simulations. Predicted FRFs from simulations show that the amplitudes of the first two modes coalesce into a single mode and the vibrational amplitudes are not effectively suppressed, especially when the control gains increase, as shown in Figure 14.

The reason for this increase in the amplitudes of the first two modes could arise from spillover effects in the closed-loop system. As a result, the controller was redesigned to operate with lower estimator gains. The second test was performed where the configurations of test plate are the same as the previous test but in one configuration the sensor location was changed from point 7 to point 23 (see Figure 13). FRFs predicted from the models of the redesigned control system is shown in Figures 15. The amplitudes of first two modes are well-suppressed as the control gains increase. Table 4 presents the redesigned estimator gains such that the designed gains are reduced by changing the sensor location.

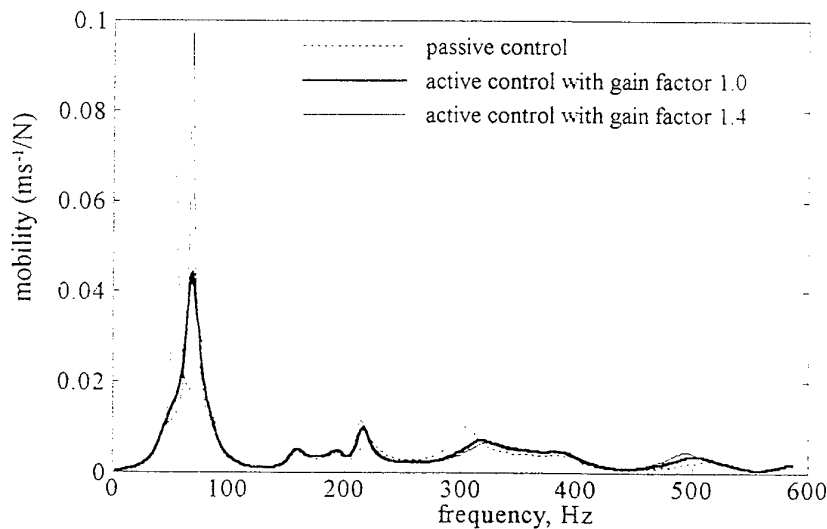


Figure 14. Simulation results: FRFs (FRF7_23) of three-layer plate with and without active control using PZT1 and 2 with a 2-channel amplifier and ACC1 (Figure 13)

Table 4

Re-designed estimator gains				
Case	1) PZT1&2, ACC1	2) PZT1&2, ACC2	3) PZT1&2, ACC1&2	
Estimator for model	65.4±296.6i	44.1±251.0i	66.6±256.5i	51.4±289.9i
gain : for mode2	-337.1±284.6i	218.6±161.4i	-127.8±100.1i	246.2±174.7i

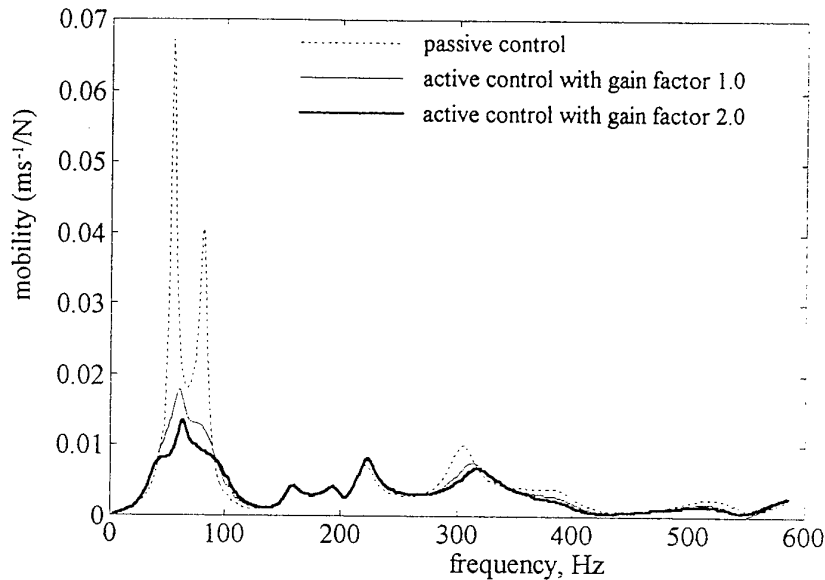


Figure 15. Simulation results: FRFs (FRF7_23) of three-layer plate with and without active control using PZT1 and 2 with a 2-channel amplifier and ACC2 (Figure 13)

Configuration 4: two PZT actuators with a two-channel amplifier and two accelerometers

In this test, two PZT actuators with a two-channel amplifier are used to perform active control as in *Configuration 3* but two accelerometers at points 7 and 23 are used for sensing. Compared to the case of using PZT1 and 2 with ACC1, the estimator gains also reduce in this configuration, PZT1 and 2 with ACC1 and 2 (Table 4). Figure 16 shows results from numerical simulations of this configuration. The best performance of vibration suppression is achieved using this configuration such that the amplitudes of the first two modes do not exceed $0.01 \text{ ms}^{-1}/\text{N}$. Note that the amplitude of mode 5, just above 200 Hz, increases slightly as the control gains increase.

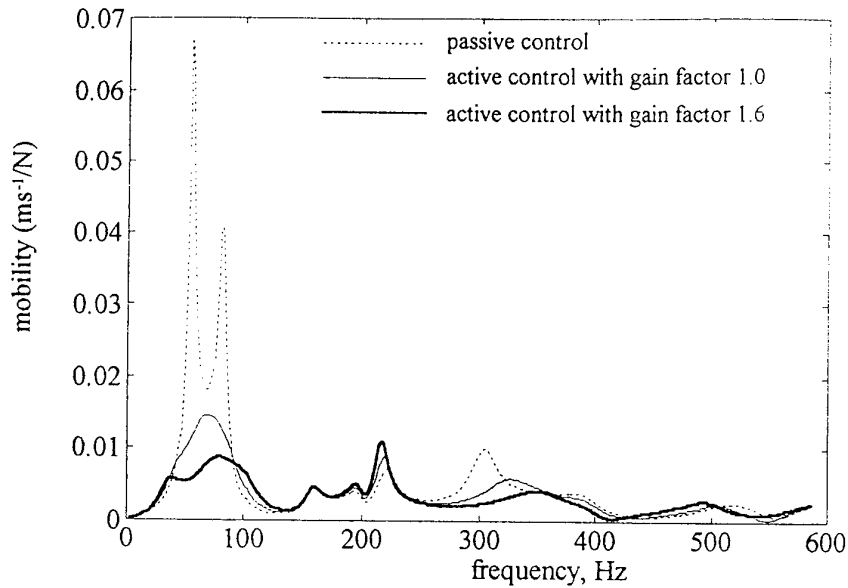


Figure 16. Simulation results: FRFs (FRF7_23) of three-layer plate with and without active control using PZT1 and 2 with a 2-channel amplifier and ACC1 and 2 (Figure 13)

4 EXPERIMENTAL VERIFICATION

In the previous section, various numerical simulations were used to study various configurations of accelerometers and PZT actuators on the three-layer test plate. In the present section, the results from experiments will be compared to those from numerical simulations. The general arrangement of the test facility is shown in Figure 17. Implementation of the digital controller is performed using a commercial package ('dSPACE' DS1102) which has up to 4 analogue-to-digital (A/D) input channels and 4 digital-to-analogue (D/A) output channels. In general, to avoid aliasing of a sampled signal, the sampling frequency must be greater than twice the highest natural frequency of interest, which in this case is around 600 Hz (for example, see Franklin et al, 1998). In the present study it was found that a sampling frequency of 10 kHz provided a suitable compromise between sufficiently accurate discretisation of the analogue signal for real-

time control and the capabilities of the digital signal processor. This sampling rate ensures that the spillover from the uncontrolled higher frequency modes (mode up to 600 Hz), included in the analysis, will not occur. The control interface card is designed to operate with SIMULINK software (Dabney and Harman, 1996).

The PZT actuator (model PC5H type VI from the MATROC company) is approximately 1 mm thick to react effectively to a maximum voltage of from 1 to 2 kV (Physik Instrumente, 1999). The relationship between force and voltage applied for the PZT actuator is derived as (Physik Instrumente, 1999)

$$\begin{aligned} f(t) &= \sigma_a A_a = \left(E_a \frac{d_{31}}{t_a} V(t) \right) \cdot b_a t_a \\ &= -0.702 V(t) \quad (\text{Newton per Volt}) \end{aligned} \quad (19)$$

where σ_a is the stress developed in the PZT, A_a is the cross-section area of the PZT, b_a is the width of the PZT, t_a is thickness of the PZT, E_a is the modulus of elasticity of the PZT ($= 1/15.1 \times 10^{-12} \text{ Nm}^{-2}$) and d_{31} is the piezoelectric constant ($= -212 \times 10^{-12} \text{ mV}^{-1}$).

4.1 Experiment results using *Configuration 1*

For comparison with the simulation results in Figure 9, of the actively damped plate with a single PZT actuator and single accelerometer, a test was carried out to obtain the corresponding experimental results and these results are shown in Figure 18.

Close agreement between simulations and experiments is evident. The introduction of active control results in significant attenuation of the two lowest modes, which was predicted by the simulation results. However the simulation results in Figure 9 indicated that these two modes would coalesce into a single mode. This did not happen in practice with the two modes remaining distinct. Note that there was significant excitation of the mode just above 500 Hz.

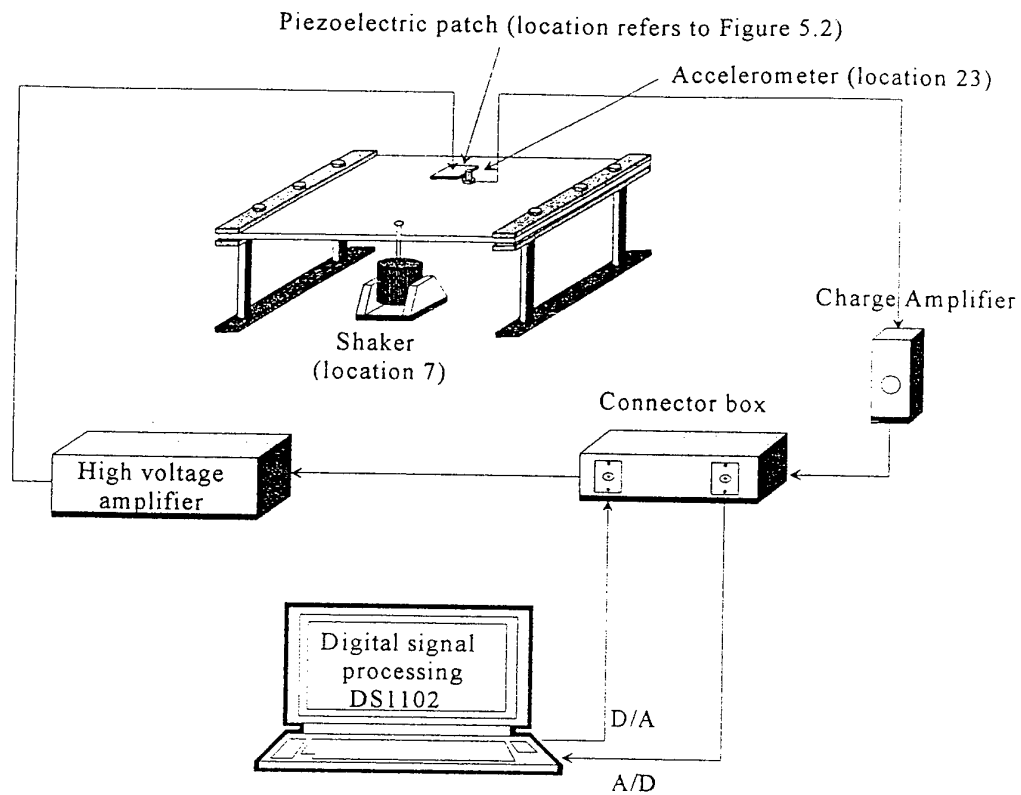


Figure 17. Arrangement of the closed-loop clamped-clamped plate with electronic equipment for digital control implementation

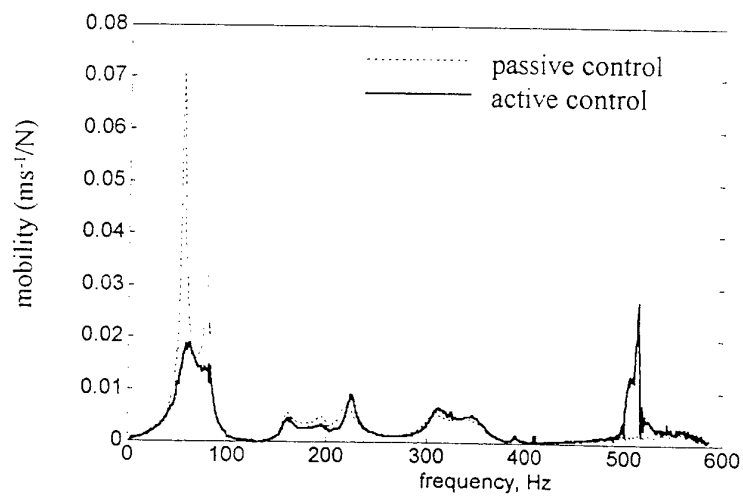


Figure 18. Measured FRFs (FRF7_23) of three-layer plate with and without active control using PZT1 and ACC1 (Figure 7)

4.2 Experimental results using *Configuration 2*

The simulation results in Figure 12 are confirmed with plots of FRFs from experiments in Figure 19. With the PZT actuator operating in the x direction only, the controlled system is more stable and levels of vibrations can be attenuated more than those in the case of the two-direction PZT actuator. Figure 20 shows FRFs from experiments of the one-direction PZT actuator case where the control gain is increased by a factor of 2.4 times the designed gain (of the result in Figure 19). Note also that the excitation of the mode just above 500 Hz is dramatically reduced in relation to the results obtained using *Configuration 1*.

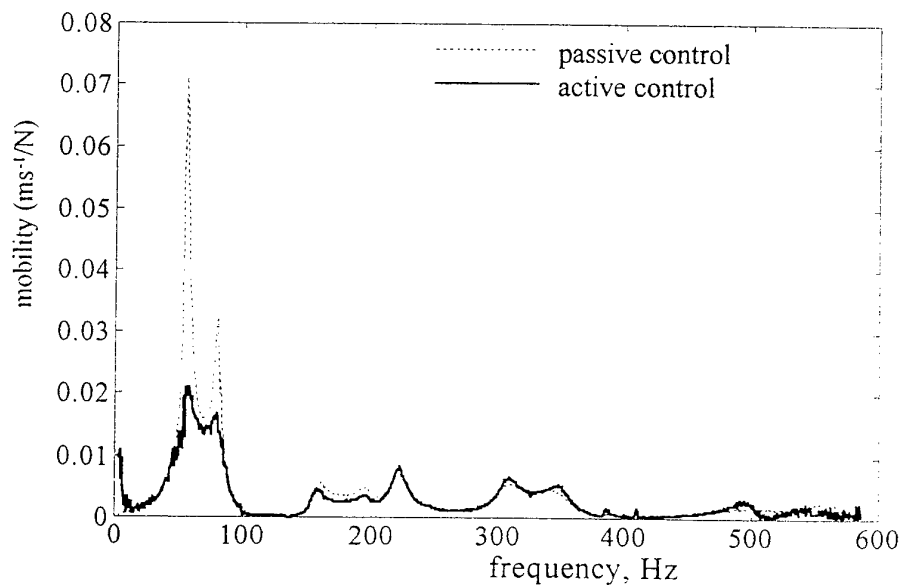


Figure 19. Measured FRFs (FRF7_23) of three-layer plate with and without active control using PZT1 and ACC1 (Figure 11)

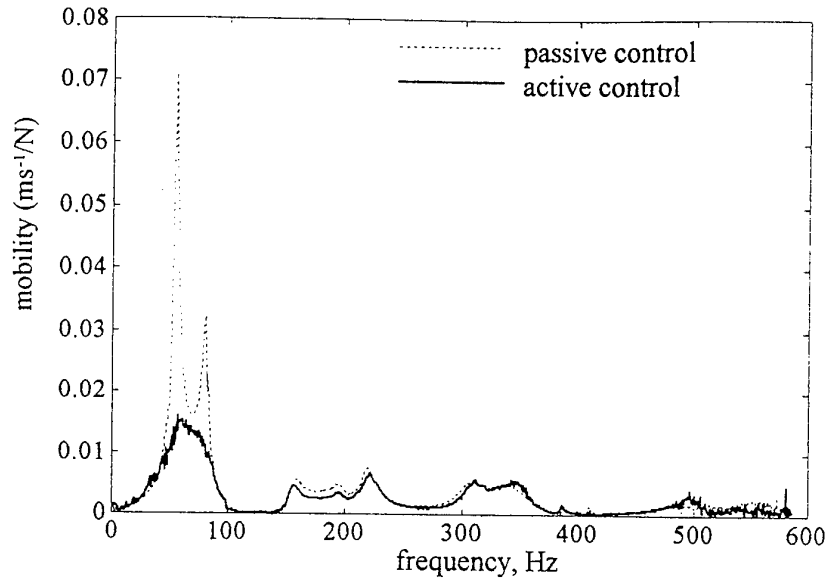


Figure 20. Measured FRFs (FRF7_23) of three-layer plate with and without active control using PZT1 and ACC1 (Figure 11) with an amplified gain factor = 2.4

4.3 Experimental results using *Configuration 3*

The corresponding experimental results of simulations in Figures 14 and 15 are shown in Figures 21 and 22, respectively. Figure 21 shows that the amplitude of the first mode is well-suppressed but this does not occur for the second mode, especially when the control gains increase. For the case of redesigning estimator gains (Figure 22), the plots show that the magnitudes of the first two vibration modes are reduced significantly as the control gains are increased.

4.4 Experimental results using *Configuration 4*

Figure 23 shows experimental results corresponding to the simulations in Figure 16. As expected, the resulting maximum amplitudes of first two modes do not exceed $0.01 \text{ ms}^{-1}/\text{N}$ (Figure 23(b)). However, the increase in amplitude of mode 5 as the control gains increase does not occur in the experimental results, instead mode 6 just above 300 Hz

shows an increase in amplitude. The most effective vibration suppression of the first two controlled modes is obtained using this configuration, two PZT actuators, two sensors and a two-channel amplifier.

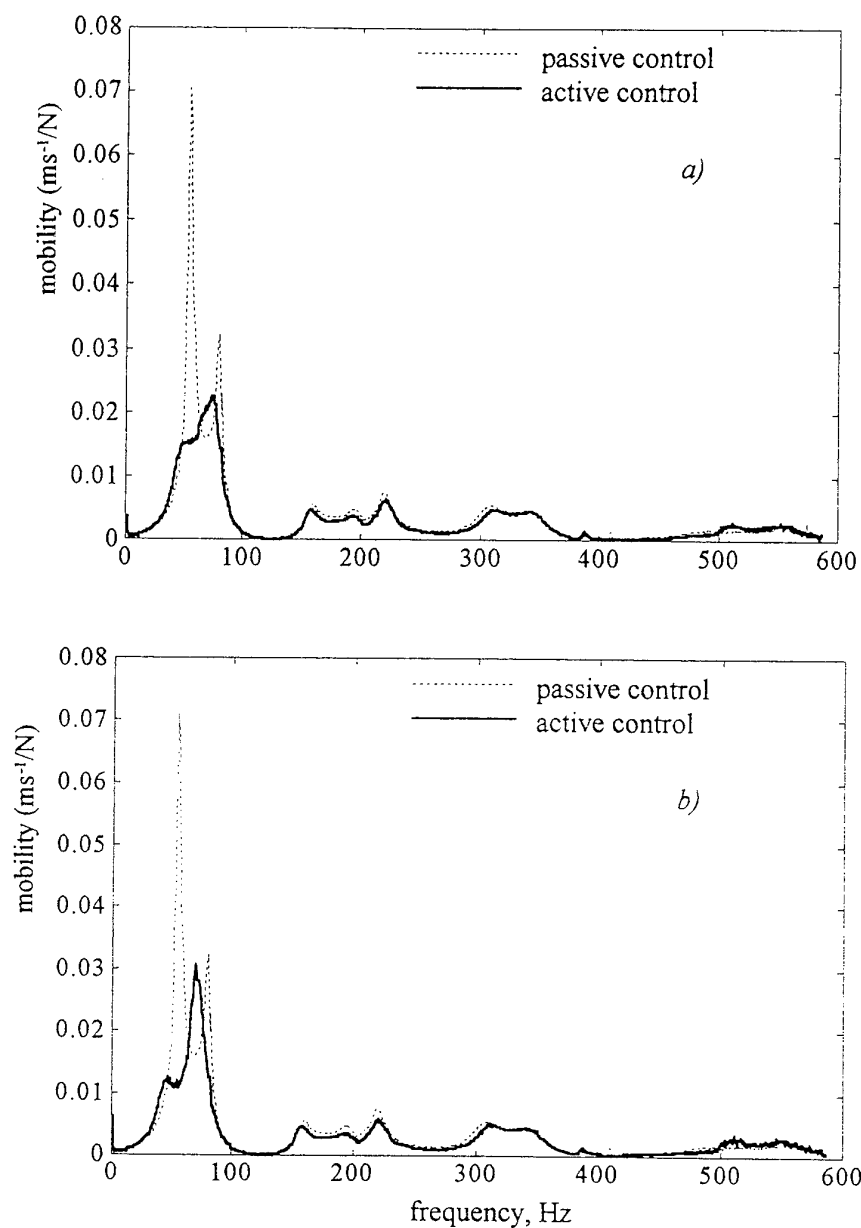


Figure 21. Measured FRFs (FRF7_23) of three-layer plate with and without control using PZT1 and 2 with a 2-channel amplifier and ACC1 (Figure 13)
a) gain as designed
b) with an amplified gain factor = 1.4

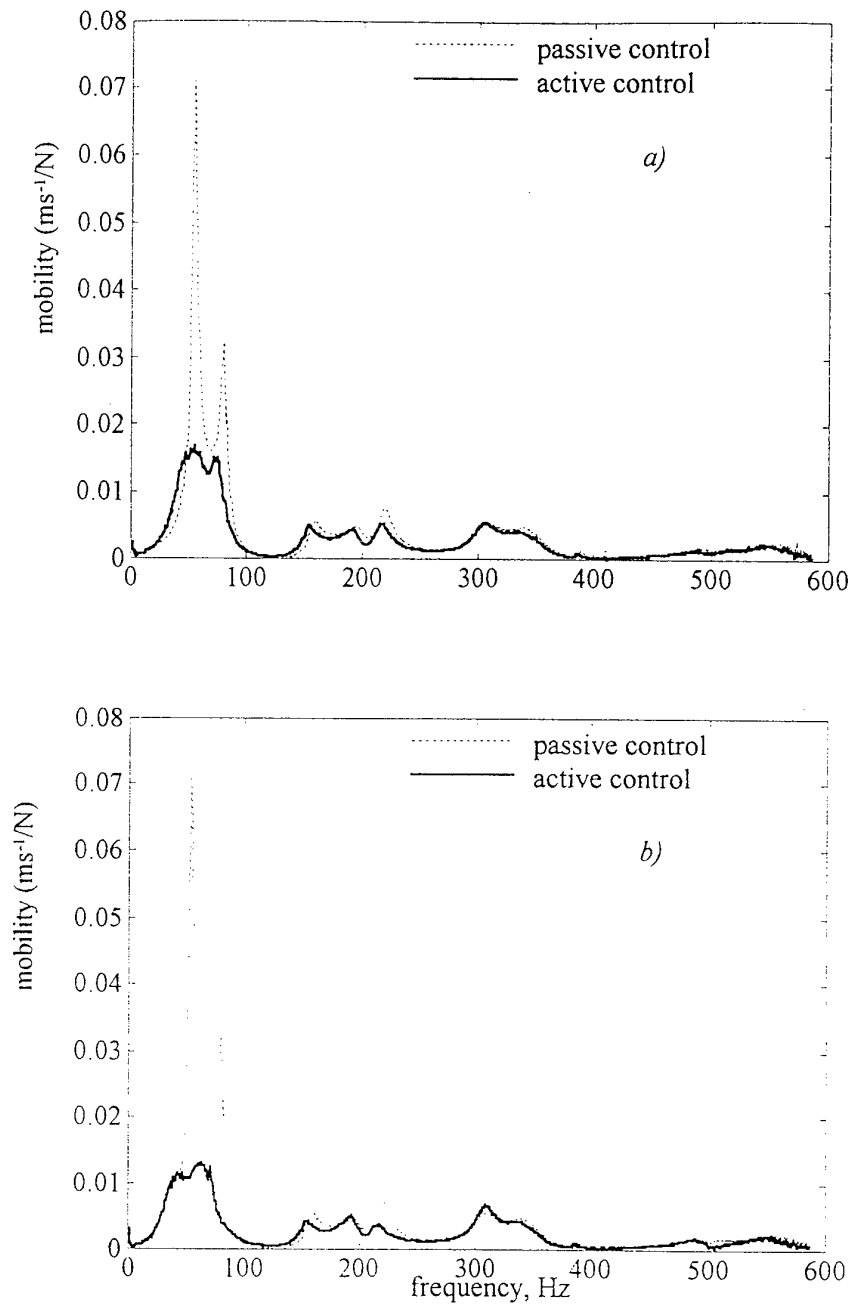


Figure 22. Measured FRFs (FRF7_23) of three-layer plate with and without active control using PZT1 and 2 with a 2-channel amplifier and ACC2 (Figure 13)

- a) gain as designed
- b) with an amplified gain factor = 2.0

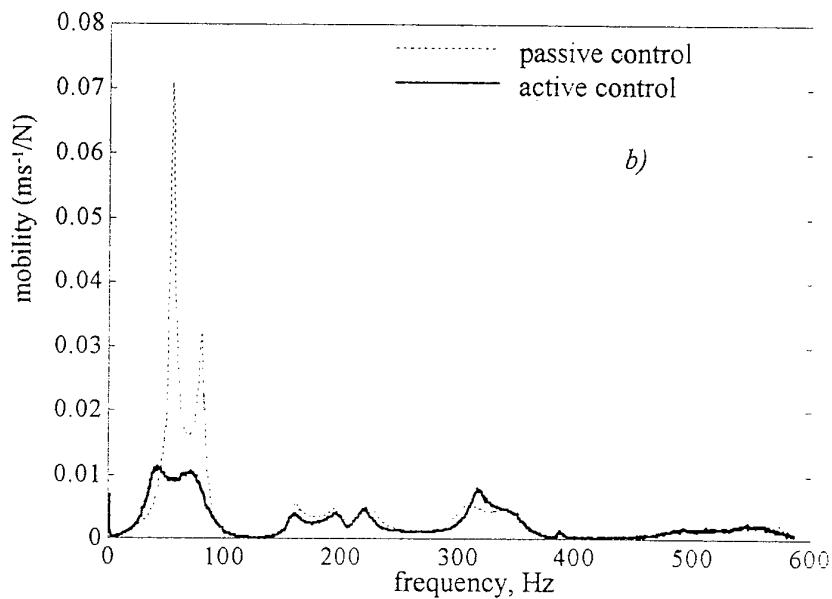
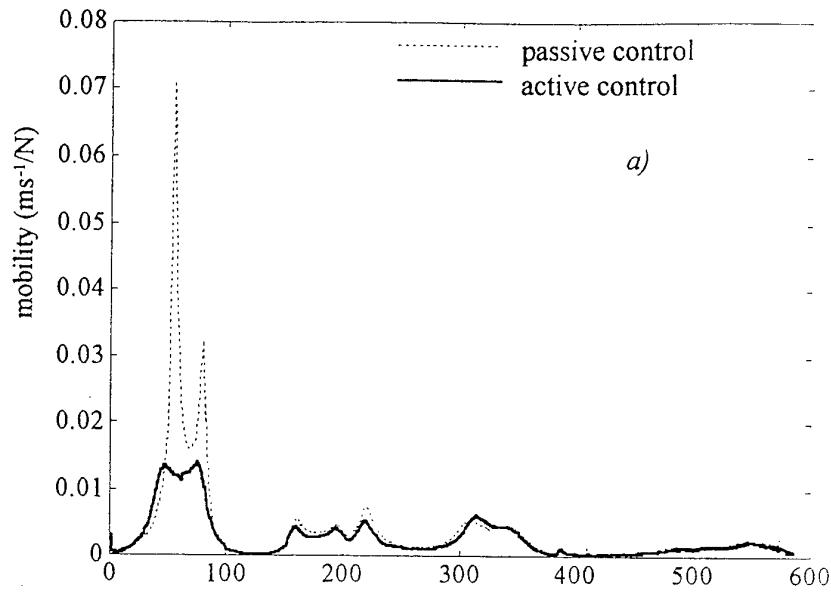


Figure 23. Measured FRFs (FRF7_23) of three-layer plate with and without active control using PZT1 and 2 with a 2-channel amplifier and ACC1 and 2 (Figure 13)

- a) gain as designed
- b) with an amplified gain factor = 1.6

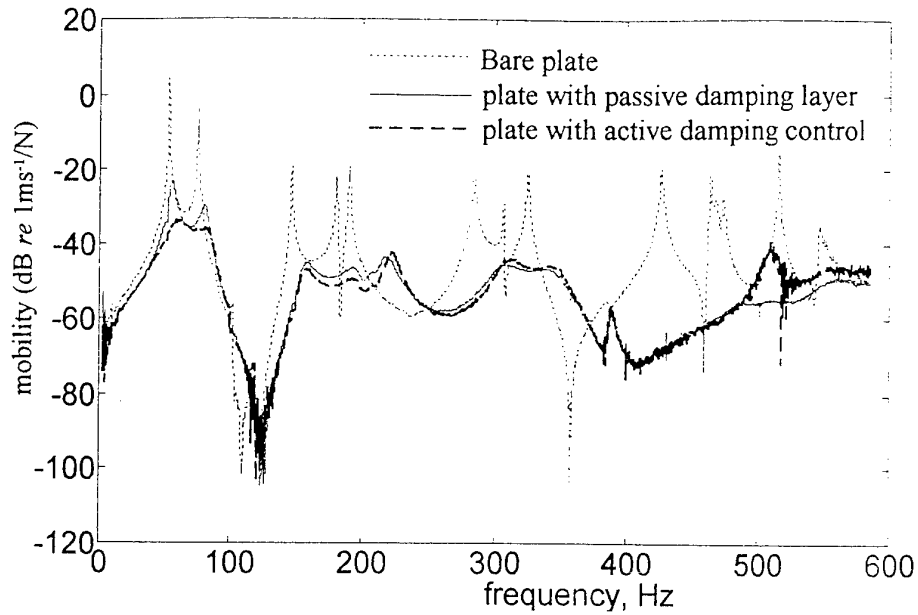


Figure 24. FRF7_23: A comparison of passive and active schemes in relation to untreated plate: the worst case of using a single PZT (a square element) with a single-channel amplifier and a single accelerometer

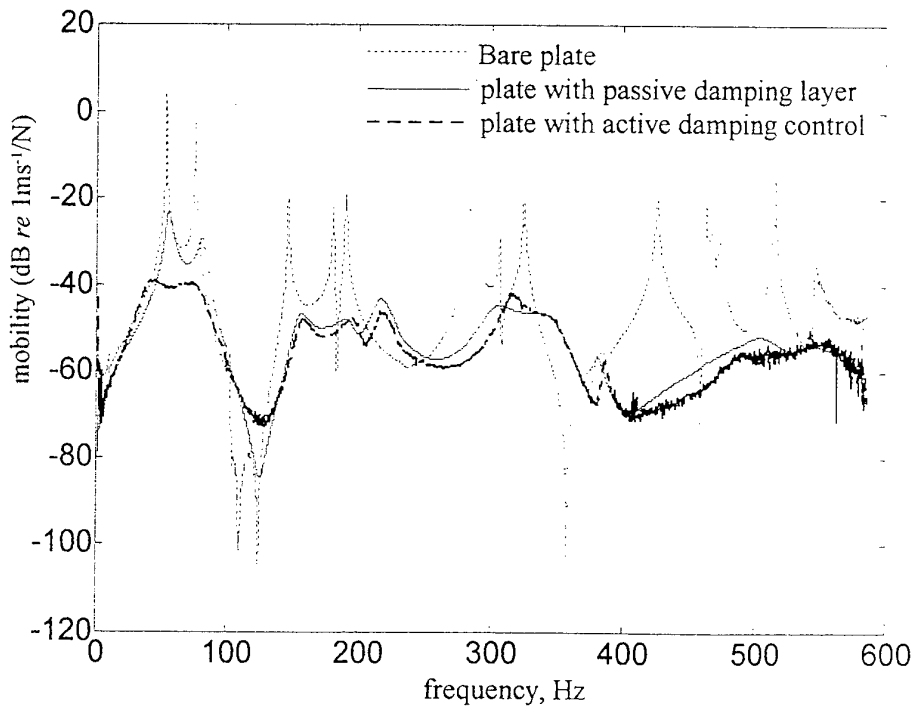


Figure 25. FRF7_23: A comparison of passive and active schemes in relation to untreated plate: the best case of using 2 PZTs with a 2-channel amplifier and 2 ACCs

In Figure 23, it is worthy of note that the level of mode 6 slightly increases as the control gains increase. This arises because mode 6 is the third bending mode where maximum curvature occurs in the middle of the plate, the same as for mode 1. However, this problem could be solved by including mode 6 as a controlled mode. In summary, Figures 24 and 25 show comparisons of FRFs from the actively controlled, passively controlled schemes and the result from the bare plate for the worst and the best cases of the control configuration performed in this study. The worst case of the control configurations is the use of a single square element PZT actuator with a single-channel amplifier and a single accelerometer (results from Figure 18). The attenuation of the first two modes compared to the passive control is about 10 dB and 5 dB, respectively (Figure 24). The active control results provide the best performance using two PZT actuators along with a two-channel amplifier and two accelerometers (Figure 23(b)). Compared with passive control, the attenuation of the first two modes through the active control is increased by 15 dB and 10 dB, respectively (Figure 25).

5 CONCLUSIONS

In this paper, a study of the active constrained layer damping treatment of a clamped-clamped plate has been described. This study has involved both numerical and experimental investigations. The strategy adopted was based upon the development of a model-based approach to control system design. The aim has been to minimise the amount of control hardware required whilst avoiding spillover problems which are liable to degrade performance. The combination of passive and active schemes in the active damping treatment has advantages where inherent damping in the passive damping layer improves the robustness of the actively controlled system and the active function is to

enhanced vibration suppression of the lower frequency modes which are characterised by long wavelengths.

Initially, finite element analysis was used to form the dynamic model of plate treated with the constrained damping layer so that design and performance of both passive and active control could be examined before the implementation stage. An updating algorithm involving pole placement was applied to match the formulated finite element model with the observed behaviour of the treated plate so that the refined model could be used in active control system design.

The development of the active control system involved the transformation of the original finite element model of the plate into a modal state-space description to be implemented in discrete time. The end result of the various computations was a fourth-order estimator/controller. Numerical experiments indicated that such an arrangement was capable of attenuating modes 1 and 2 (in conjunction with a 72 nd order model of the plate) without incurring significant problems due to spillover. This was achieved using only a single sensor and single actuator channel.

The experimental study confirmed the results of the numerical simulations. Various configurations of the control strategies were investigated - a single PZT actuator and single accelerometer - a single PZT actuator activating in x direction only - two PZT actuators associated with single- or two-channel amplifiers and one or two accelerometers. In the simplest configuration - a single PZT patch and single accelerometer, further reduction of vibration levels in the passively damped plate through the active control is about 10 dB and 5 dB for the first and second modes, respectively. The best performance of vibration suppression was found in the case of using two PZT actuators incorporating with a two-channel amplifier and two accelerometers such that high attenuation of vibration levels was achieved, 15 dB and 10 dB in the first and second

modes, respectively. The influence of sensor locations on the performance of the controlled system has been investigated. Lower estimator gains can be obtained by changing the sensor locations so as to minimise spillover effects and to provide better vibration suppression. Also two configurations of PZT actuator were investigated. A single PZT patch arranged to provide actuation in mutually perpendicular directions, and an arrangement of four PZT patches driven by a single amplifier but designed to activate the plate in a single direction only. Both configurations were effective at controlling modes 1 and 2 but the single PZT patch produced significant excitation of a mode above 500 Hz.

ACKNOWLEDGEMENT

The authors would like to thank the European Research Office of the US Army for partial funding of the control equipment under contract number N68171-98-M-5388.

REFERENCES

- Azvine B, Tomlinson G R, Wynne R J and Sensburg O 1994 Vibration suppression of flexible structures using active damping 1994 *4th International Conference on Adaptive Structures*, Cologne.
- Balas M J 1978 Feedback control of flexible systems. *IEEE Transactions on Automatic and Control* **AC-23**, 673-679.
- Baz A and Ro J 1993 Partial treatment of flexible beams with active constrained layer damping. *Conference of Engineering Sciences Society*, Charlottesville, VA.
- Baz A and Ro J 1996 Vibration control of plates with active constrained layer damping. *Smart Materials and Structures* **5**, 272-280.

- Burl J B 1999 *Linear Optimal Control*. California, USA.: Addison Wesley Longman, Inc.
- Chantalakhana C and Stanway R 1998 Control of plate vibrations using smart technology. *Proceedings of the 4th European and 2nd MIMR Conference, Harrogate, UK*, 195-204.
- Chantalakhana C. and Stanway R 2000 Active constrained layer damping of clamped-clamped plate vibrations *Journal of Sound and Vibration*, submitted.
- Dabney J B and Harman T L 1996 *The Student Edition of SIMULINK*. New Jersey: Prentice Hall.
- Franklin G F, Powell J D and Workman M 1998 *Digital Control of Dynamic Systems (3rd edition)*. California, USA.: Addison Wesley Longman, Inc.
- Guyan R J 1965 Reduction of stiffness and mass matrices. *AIAA Journal* **3**, 380.
- Inman D J and Minas C 1990 Matching analytical models with experimental modal data in mechanical systems. *Control and Dynamic Systems* **37**, 327-363.
- LMS 1993 *LMS CADA-PC User Manual*.
- Morgan Matroc 1999 Piezoceramics: manufacturer's data sheets.
- Minas C and Inman D J 1989 Identification of a nonproportional damping matrix from incomplete modal information. *Transactions of the American Society of Mechanical Engineers, Journal of Vibration and Acoustics* **113**, 219-224.
- Ogata K 1987 *Discrete-time Control Systems*. London: Englewood Cliffs, Prentice-Hall.
- Physik Instrumente (PI) Tutorial Manual. 1999 Web page: <http://www.physikinstrumente.com/tutorial>.
- Porter B and Crossley R 1972 *Modal Control Theory and Applications*. London: Taylor and Francis.
- Veley D E and Rao S S 1996 A comparison of active, passive and hybrid damping in structural design. *Smart Materials and Structures* **5**, 660-671.